

JPL D-11401, Rev. D

Multi-angle Imaging SpectroRadiometer (MISR)

Level 2 Surface Retrieval Algorithm Theoretical Basis

Approval:

David J. Diner
MISR Principal Investigator

The MISR web site should be consulted to determine the latest released version of this document (<http://www-misr.jpl.nasa.gov>).
Approval signatures are on file with the MISR Project.



Jet Propulsion Laboratory
California Institute of Technology

TABLE OF CONTENTS

1. INTRODUCTION.....	1
1.1 PURPOSE.....	1
1.2 SCOPE.....	2
1.3 MISR DOCUMENTS.....	2
1.4 REVISIONS	3
2. EXPERIMENT OVERVIEW	4
2.1 OBJECTIVES OF MISR SURFACE RETRIEVALS	4
2.2 INSTRUMENT CHARACTERISTICS.....	5
2.3 SURFACE RETRIEVAL STRATEGY	6
3. ALGORITHM DESCRIPTION	9
3.1 PROCESSING OUTLINE.....	9
3.2 ALGORITHM INPUT	14
3.2.1 MISR data.....	14
3.2.1.1 Corrected terrain-projected TOA equivalent reflectances	14
3.2.1.2 Ellipsoid-referenced geometric parameters.....	15
3.2.1.3 Radiometric Data Quality Indicator	15
3.2.1.4 Aerosol Retrieval Success Indicator	15
3.2.1.5 Retrieval Applicability Mask	16
3.2.1.6 Retrieved aerosol parameters	16
3.2.1.7 Atmospheric pressure.....	16
3.2.1.8 Ancillary aerosol model parameters.....	16
3.2.1.9 Aerosol models for conventional ocean surface retrieval	17
3.2.1.10 Band-weighted exo-atmospheric solar irradiances	17
3.2.1.11 Canopy radiative transfer parameters.....	17
3.2.1.12 Biome Classification Map.....	17
3.2.1.13 NDVI-FPAR regression coefficients	17
3.2.2 Non-MISR data	17
3.2.2.1 Surface wind speed	18
3.3 THEORETICAL DESCRIPTION OF LAND SURFACE RETRIEVALS	18
3.3.1 Calculate Subregion Variability.....	18
3.3.1.1 Physics of the problem.....	18
3.3.1.2 Mathematical description of the algorithm	19
3.3.1.3 Archived algorithm output	19
3.3.2 Sun and view angles for inclined surfaces	19

3.3.2.1 Physics of the problem	19
3.3.2.2 Mathematical description of the algorithm	20
3.3.3 Retrieve HDRF and BHR	21
3.3.3.1 Physics of the problem	21
3.3.3.2 Mathematical description of the algorithm	22
3.3.3.3 Algorithm synopsis and computational specifics	29
3.3.3.4 Aerosol mixture requirements of the algorithm	32
3.3.3.5 Best estimate of the HDRF and BHR and their uncertainties	34
3.3.3.6 Best estimates of the ancillary atmospheric data and their uncertainties	39
3.3.3.7 Archived algorithm output	40
3.3.4 Retrieve BRF and DHR	41
3.3.4.1 Physics of the problem	41
3.3.4.2 Mathematical description of the algorithm	42
3.3.4.3 Algorithm synopsis and computational specifics	47
3.3.4.4 Aerosol mixture requirements of the algorithm	48
3.3.4.5 Archived algorithm output	49
3.3.5 Calculate PAR-integrated BHR and DHR	49
3.3.5.1 Physics of the problem	49
3.3.5.2 Mathematical description of the algorithm	49
3.3.5.3 Aerosol mixture requirements of the algorithm	52
3.3.5.4 Archived algorithm output	52
3.3.6 Determine subregion LAI and associated uncertainty	52
3.3.6.1 Physics of the problem	52
3.3.6.2 Mathematical description of the algorithm	53
3.3.6.3 Algorithm synopsis and computational specifics	57
3.3.6.4 Archived algorithm output	59
3.3.7 Determine subregion FPAR and its uncertainty	60
3.3.7.1 Physics of the problem	60
3.3.7.2 Mathematical description of the algorithm	60
3.3.7.3 Algorithm synopsis and computational specifics	63
3.3.8 Determine regional FPAR	65
3.3.8.1 Physics of the problem	65
3.3.8.2 Mathematical description of the algorithm	65
3.3.8.3 Archived algorithm output	66
3.4 THEORETICAL DESCRIPTION OF OCEAN SURFACE RETRIEVALS	66
3.4.1 Determine TOA equivalent reflectance due to sun glitter and whitecaps	66
3.4.1.1 Physics of the problem	66
3.4.1.2 Mathematical description of the algorithm	67
3.4.1.3 Aerosol mixture requirements of the algorithm	68
3.4.2 Retrieve B-camera water-leaving equivalent reflectance (conventional approach)	

3.4.2.1	Physics of the problem	68
3.4.2.2	Mathematical description of the algorithm	69
3.4.2.3	Aerosol mixture requirements of the algorithm	70
3.4.2.4	Archived algorithm output	70
3.4.3	Retrieve B-camera water-leaving equivalent reflectance (experimental approach)	
70		
3.4.3.1	Physics of the problem	70
3.4.3.2	Mathematical description of the algorithm	70
3.4.3.3	Aerosol mixture requirements of the algorithm	71
3.4.3.4	Best estimate of water-leaving equivalent reflectance and its uncertainty	72
3.4.3.5	Archived algorithm output	73
3.4.4	Retrieve phytoplankton pigment concentration	74
3.4.4.1	Physics of the problem	74
3.4.4.2	Mathematical description of the algorithm	74
3.4.5	Estimated uncertainty of C	75
3.4.5.1	Archived algorithm output	76
3.5	ALGORITHM SENSITIVITY STUDIES	76
3.5.1	HDRF and BHR land retrievals	76
3.5.2	NDVI-FPAR relationship	81
3.5.3	Determination of equivalent reflectance of water-leaving radiance	84
3.6	PRACTICAL CONSIDERATIONS	85
3.6.1	Numerical computation considerations	85
3.6.2	Programming and procedural considerations	85
3.6.3	Configuration of retrievals	85
3.6.4	Quality assessment and diagnostics	86
3.6.5	Exception handling	86
3.7	ALGORITHM VALIDATION	86
3.8	ALGORITHM DEVELOPMENT SCHEDULE	87
4.	ASSUMPTIONS AND LIMITATIONS	88
4.1	ASSUMPTIONS	88
4.2	LIMITATIONS	88
5.	REFERENCES	89

GLOSSARY OF ACRONYMS

A

ACP (Aerosol Climatology Product)
AGP (Ancillary Geographic Product)
ALB (Ancillary Land Biome)
ARP (Ancillary Radiometric Product)
ASTER (Advanced Spaceborne Thermal Emission and Reflectance Radiometer)
ATB (Algorithm Theoretical Basis)
AU (Astronomical Unit)

B

BHR (Bi-Hemispherical Reflectance)
BOA (Bottom of Atmosphere)
BRDF (Bidirectional Reflectance Distribution Function)
BRF (Bidirectional Reflectance Factor)

C

CART (Canopy Architecture Radiative Transfer)
CCD (Charge Coupled Device)
CZCS (Coastal Zone Color Scanner)

D

DAAC (Distributed Active Archive Center)
DDV (Dense Dark Vegetation)
DHR (Directional Hemispherical Reflectance)

F

FPAR (Fractional Absorbed Photosynthetically Active Radiation)

G

GDQI (Geometric Data Quality Indicator)

H

HDRF (Hemispherical-Directional Reflectance Factor)

I

IFOV (Instantaneous Field of View)

L

LAI (Leaf Area Index)

M

MISR (Multi-angle Imaging SpectroRadiometer)

MODIS (Moderate Resolution Imaging Spectroradiometer)

P

PAR (Photosynthetically Active Radiation)

R

RDQI (Radiometric Data Quality Indicator)

S

SCF (Science Computing Facility)

SeaWiFS (Sea-viewing Wide Field-of-view Sensor)

SMART (Simulated MISR Ancillary Radiative Transfer)

SOM (Space Oblique Mercator)

SPOT (Systeme Pour l'Observation de la Terre)

T

TOA (Top of Atmosphere)

TOAC (Tropical Ocean Atmospheric Correction)

W

WGS (World Geodetic System)

1. INTRODUCTION

1.1 PURPOSE

This Algorithm Theoretical Basis (ATB) document describes the algorithms used to retrieve the surface parameters of the MISR Level 2 Aerosol/Surface Product. These parameters are summarized in Table 1. In particular, this document identifies sources of input data, both MISR and non-MISR, which are required for surface retrievals; provides the physical theory and mathematical background underlying the use of this information in the retrievals; includes implementation details; and describes assumptions and limitations of the adopted approach. It is used by the MISR Science Data System Team to establish requirements and functionality of the data processing software.

Table 1: Surface parameters in the Level 2 Aerosol/Surface Product

Parameter name	Units	Horizontal Sampling (Coverage)	Comments
Hemispherical-Directional Reflectance Factor (HDRF)	none	1.1 km (Land)	<ul style="list-style-type: none">• Surface radiance ratioed to that from ideal lambertian reflector at surface• Ambient sky conditions, i.e., direct plus diffuse illumination• 9 viewing angles, 4 spectral bands
Bihemispherical Reflectance (BHR)	none	1.1 km spectral, 17.6 km PAR (Land)	<ul style="list-style-type: none">• Radiant exitance ratioed to irradiance at surface (i.e., albedo)• Ambient sky conditions, i.e., direct plus diffuse illumination• 4 spectral bands and PAR integrated
Bidirectional Reflectance Factor (BRF)	none	1.1 km (Land)	<ul style="list-style-type: none">• Surface radiance ratioed to that from ideal lambertian reflector at surface• Direct illumination only• 9 viewing angles, 4 spectral bands
BRF Model Parameters	none	1.1 km (Land)	<ul style="list-style-type: none">• Model parameters from a fit to the surface BRF
Directional-Hemispherical Reflectance (DHR)	none	1.1 km spectral, 17.6 km PAR (Land)	<ul style="list-style-type: none">• Radiant exitance ratioed to irradiance at surface (i.e., albedo)• Direct illumination only• 4 spectral bands and PAR-integrated
Ancillary atmospheric data	none	17.6 km (Global)	<ul style="list-style-type: none">• Downwelling diffuse irradiance• BOA bihemispherical albedo• Computed from the ACP and SMART Dataset

Table 1: Surface parameters in the Level 2 Aerosol/Surface Product (continued)

Parameter name	Units	Horizontal Sampling (Coverage)	Comments
Leaf-Area Index (LAI)	none	1.1 km (Land)	<ul style="list-style-type: none"> • Best-fitting biome type(s) determined • Mean LAI for each biome type • Spread in LAI for each biome type • Determined using the CART file
Fractional Absorbed Photosynthetically Active Radiation (FPAR)	none	17.6 km (Land)	<ul style="list-style-type: none"> • Determined from LAI and CART file • Averaged over all subregions and biome types
Water-leaving equivalent reflectance (1) and aerosol model parameters	none	1.1 km (Tropical Ocean)	<ul style="list-style-type: none"> • Ocean: Most glitter-free B-camera viewing angle, blue and green spectral bands, low latitudes, using conventional algorithm • Aerosol model from TOAC Dataset
Water-leaving equivalent reflectance (2)	none	1.1 km (Tropical Ocean)	<ul style="list-style-type: none"> • Ocean: Most glitter-free B-camera viewing angle, blue and green spectral bands, low latitudes, using experimental algorithm
Phytoplankton Pigment Concentration (1)	mg m ⁻³	1.1 km (Tropical Ocean)	<ul style="list-style-type: none"> • Calculated using B-camera equivalent reflectances from conventional algorithm
Phytoplankton Pigment Concentration (2)	mg m ⁻³	1.1 km (Tropical Ocean)	<ul style="list-style-type: none"> • Calculated using B-camera equivalent reflectances from experimental algorithm
Retrieval Quality Indicators	vary	vary	<ul style="list-style-type: none"> • Includes Subregion Variability

1.2 SCOPE

This document covers the algorithm theoretical basis for the surface parameters of the Aerosol/Surface Product which are to be routinely retrieved at the DAAC. Post-launch and specialized products or parameters are not discussed. Current development and prototyping efforts may result in modifications to parts of certain algorithms. Only the algorithms which will be implemented at the DAAC for routine processing will be preserved in the final release of this document.

Chapter 1 describes the purpose and scope of the document. Chapter 2 provides a brief overview. The processing concept and algorithm description are presented in Chapter 3. Chapter 4 summarizes assumptions and limitations. References for publications cited in the text are given in Chapter 5. Literature references are indicated by a number in italicized square brackets, e.g., [1].

1.3 MISR DOCUMENTS

Reference to MISR documents is indicated by a number in italicized square brackets, e.g., [M-1]. The MISR web site (<http://www-misr.jpl.nasa.gov>) should be consulted to determine the

latest released version of each of these documents.

[M-1] Experiment Overview, JPL D-13407.

[M-2] Level 1 In-flight Radiometric Calibration and Characterization Algorithm Theoretical Basis, JPL D-13398.

[M-3] Level 1 Georectification and Registration Algorithm Theoretical Basis, JPL D-11532.

[M-4] Level 1 Ancillary Geographic Product Algorithm Theoretical Basis, JPL D-13400.

[M-5] Level 2 Aerosol Retrieval Algorithm Theoretical Basis, JPL D-11400.

[M-6] Level 2 Ancillary Products and Datasets Algorithm Theoretical Basis, JPL D-13402.

[M-7] Algorithm Development Plan, JPL D-11220.

[M-8] Science Data Validation Plan, JPL D-12626.

[M-9] Science Data Quality Indicators, JPL D-13496.

[M-10] Science Data Processing Sizing Estimates, JPL D-12569.

1.4 REVISIONS

The original version of this document was dated February 23, 1994. Revision A was released December 1, 1994. Revision B was released August 15, 1996. Revision C was released January 8, 1998. This version is Revision D. Changes from Rev. C are indicated through the use of change bars, as shown at the left.

2. EXPERIMENT OVERVIEW

2.1 OBJECTIVES OF MISR SURFACE RETRIEVALS

About 30% of the Earth's surface is covered by land and much of this is vegetated. Thus, land surface processes are important components of the terrestrial climate system [10]. In particular, continents affect the climate system because of

- (1) Their orography, which substantially modifies the planetary atmospheric flow;
- (2) Their relatively small heat capacity, compared with that of the oceans, which induces a range of dynamic perturbations, from sea breezes to monsoons;
- (3) The very high spatial and temporal variability of terrestrial surfaces, which affect the roughness of these surfaces, and therefore the dissipation of atmospheric kinetic energy through friction and turbulence;
- (4) Their albedo and, to a lesser extent, emissivity, which are highly variable in space and time, and which control the absorption of solar and the emission of thermal radiation, respectively, hence the bulk of the energy available in the climate system;
- (5) Their hosting of most of the biosphere (over 99% by mass), which exerts significant controls on the exchange of heat, moisture, and chemicals within the climate system, through a surface of contact (that of plant leaves) which exceeds the total area of the planet's surface.

The bulk of the solar energy provided to the troposphere is first absorbed at the lower boundary (oceans and continents) and then made available to the atmosphere through the fluxes of sensible and latent heat, as well as in the form of thermal radiation. Accurate descriptions of the interactions between the surface and the atmosphere require reliable quantitative information on the fluxes of energy (all forms), mass (including water and CO₂), and momentum, especially over terrestrial areas, where they are closely associated with the rates of evapotranspiration and photosynthesis. Many of these processes and interactions directly affect the reflectance of the surface [27], [39], [40]. Reflectance measurements, which can be acquired by remote sensing, are therefore particularly useful to describe and predict these surface-atmosphere interactions. Clearly, the usefulness of such measurements is not limited to vegetated areas, as all significant modifications of surface properties, whether due to natural or human-induced causes, tend to affect this property. While these changes may impact on the state of the climate system through a perturbation of the boundary condition at the bottom of the atmosphere [8], [11], [31], they also provide a unique opportunity for their detection through remote sensing techniques.

Angular signature information is also expected to be a significant component of improved surface cover classification and characterization. The time-evolution of terrestrial ecosystems is difficult to monitor at the surface and satellite platforms provide a unique opportunity to carry out extensive surveys with comprehensive spatial coverage and high time resolution. Detection of eco-

physiological change on the land surface, resulting from natural processes (canopy succession and species replacement) or anthropogenic activities (e.g., deforestation, acid rain), necessitates accurate, repeatable measurements of the surface that can be used for landscape classification. Over oceans, monitoring of ocean color provides the means of monitoring marine biological productivity and its changes with time.

The overall scientific objectives of the MISR surface retrievals are:

- (1) To characterize the bidirectional reflectance distribution function of all terrestrial surfaces, as a function of space, time, and surface type;
- (2) To study, on a global basis, the magnitude and natural variability in space and time of sunlight absorption and scattering by the Earth's surface, particularly through determination of the surface bihemispherical reflectance (spectral albedo);
- (3) To provide improved measures of land surface classification and dynamics in conjunction with MODIS (which will fly on the same EOS spacecraft as MISR);
- (4) To supplement MODIS observations of ocean color in the tropics by providing atmospherically-corrected water leaving radiances in the equatorial regions.

The scientific background on each of these objectives, a historical perspective on surface retrievals using remote sensing, the unique contribution of MISR, and the scientific rationale for the surface parameter contents of the MISR Aerosol/Surface Product are presented in [M-1].

2.2 INSTRUMENT CHARACTERISTICS

The MISR instrument consists of nine pushbroom cameras. It is capable of global coverage every nine days and flies in a 705-km descending polar orbit. The cameras are arranged with one camera pointing toward the nadir (designated An), one bank of four cameras pointing in the forward direction (designated Af, Bf, Cf, and Df in order of increasing off-nadir angle), and one bank of four cameras pointing in the aftward direction (using the same convention but designated Aa, Ba, Ca, and Da). Images are acquired with nominal view angles, relative to the surface reference ellipsoid, of 0°, 26.1°, 45.6°, 60.0°, and 70.5° for An, Af/Aa, Bf/Ba, Cf/Ca, and Df/Da, respectively. Each camera uses four Charge-Coupled-Device (CCD) line arrays in a single focal plane. The line arrays consist of 1504 photoactive pixels plus 16 light-shielded pixels per array, each 21 μm by 18 μm . Each line array is filtered to provide one of four MISR spectral bands. The spectral band shapes are approximately gaussian and centered at 446, 558, 672, and 866 nm.

MISR contains 36 parallel signal chains corresponding to the four spectral bands in each of the nine cameras. The zonal overlap swath width of the MISR imaging data (i.e., the swath seen in common by all nine cameras along a line of constant latitude) is ≥ 360 km, which provides global

multi-angle coverage of the entire Earth in 9 days at the equator and 2 days at the poles. The crosstrack IFOV and sample spacing of each pixel is 275 m for all of the off-nadir cameras, and 250 m for the nadir camera. Downtrack IFOV's depend on view angle, ranging from 214 m in the nadir to 707 m at the most oblique angle. However, sample spacing in the downtrack direction is 275 m in all cameras. The instrument is capable of buffering the data to provide 4 sample x 4 line, 2 sample x 2 line, or 1 sample x 4 line averages, in addition to the mode in which pixels are sent with no averaging. The averaging capability is individually selectable within each of the 36 channels, providing several observational modes of the MISR instrument. The MISR Aerosol/Surface Product is generated from Global Mode data. Global Mode refers to continuous operation with no limit on swath length. Global coverage in a particular spectral band of one camera is provided by operating the corresponding signal chain continuously in a selected resolution mode. Any choice of averaging mode among the nine cameras that is consistent with the instrument power and data rate allocation is suitable for Global Mode. Current plans are to operate the instrument in the 4 x 4 averaging mode (1.1 km sampling) with selected channels operating in 1 x 1 or 1 x 4 mode. When the instrument operates in the higher resolution modes, aerosol retrievals are more readily accomplished because of better cloud discrimination and higher spatial contrast over land. Since surface retrievals require that an aerosol retrieval be performed first, this mode of instrument operation also facilitates the production of the surface parameters.

Additional background on the instrument design is provided in [M-1].

2.3 SURFACE RETRIEVAL STRATEGY

Before surface retrievals can be performed within a given region, various atmospheric parameters need to be determined by means of an aerosol retrieval. Here, a region is defined to be an area of 17.6 km x 17.6 km or a 16 x 16 array of 1.1 km samples, covering either land or ocean. However, an aerosol retrieval is not performed if the region exhibits too much cloudiness or if the surface terrain is too topographically complex [M-5]. Even if an aerosol retrieval was successful, some 1.1 km samples in the region may not be suitable for a surface retrieval due to subregion cloudiness, cloud shadows, sun glitter (usually over water), and other, instrument-related, reasons [M-5].

The MISR surface retrievals will generate a number of parameters related to the surface science objectives outlined above. Over land, these include hemispherical-directional reflectance factor (HDRF), bidirectional reflectance factor (BRF), bihemispherical reflectance (BHR), directional-hemispherical reflectance (DHR), a parametric model of the surface BRF, leaf area index (LAI), and the fraction of incident photosynthetically active radiation absorbed by live vegetation (FPAR). Over ocean, these include equivalent reflectance and phytoplankton pigment concentration. A summary table defining these and related surface-atmosphere radiation interaction terms is provided in Table 2.

The definitions of the terms included in Table 2 vary according to (a) whether the surface is assumed to be illuminated by sunlight, skylight, or both, and (b) whether the upwelling radiation is integrated over all directions, or if it is reported as a function of view angle. The commonly used term “albedo” refers to one of the hemispherically integrated quantities (BHR or DHR), depending on what illumination conditions are assumed. BRDF is just a factor of π smaller than the BRF.

Table 2: Surface parameters and related surface-atmosphere radiation interaction terms

Term	Name	Definition	Units
BRDF	Bidirectional Reflectance Distribution Function	Surface-leaving radiance divided by incident irradiance from a single direction ($= \text{BRF}/\pi$)	sr^{-1}
BRF	Bidirectional Reflectance Factor	Surface-leaving radiance divided by radiance from a lambertian reflector illuminated from a single direction	--
HDRF	Hemispherical-Directional Reflectance Factor	Surface-leaving radiance divided by radiance from a lambertian reflector illuminated under the same ambient conditions	--
DHR	Directional Hemispherical Reflectance	Radiant exitance divided by irradiance (“albedo”) under illumination from a single direction (i.e., in the absence of an atmosphere)	--
BHR	Bihemispherical Reflectance	Radiant exitance divided by irradiance (“albedo”) under ambient illumination conditions	--
LAI	Leaf Area Index	One-side green leaf area per unit ground area, integrated from canopy top to the ground	--
FPAR	Fractional absorbed Photosynthetically Active Radiation	PAR irradiance absorbed by live vegetation divided by incident PAR irradiance	--
ρ	Equivalent reflectance	$\pi \cdot$ radiance divided by normal incidence irradiance	--
C	Phytoplankton pigment concentration	Concentration of chlorophyll <i>a</i> + concentration of phaeophytin <i>a</i>	mg m^{-3}
L	Spectral radiance	Radiant energy per time-area-solid angle-wavelength interval	$\text{W m}^{-2} \text{sr}^{-1} \mu\text{m}^{-1}$
E	Spectral irradiance	Incident radiant energy flux	$\text{W m}^{-2} \mu\text{m}^{-1}$
M	Spectral radiant exitance	Surface-leaving radiant energy flux	$\text{W m}^{-2} \mu\text{m}^{-1}$

The following sequence of land surface retrieval activity is performed on all suitable 1.1 km samples within a region. First, the hemispherical-directional reflectance factors (HDRF’s) for all available camera views and the bihemispherical reflectances (BHR’s) are determined for the four MISR spectral channels. The HDRF’s and BHR’s are surface reflectance properties for illumina-

tion conditions of the ambient atmosphere (i.e., direct and diffuse sunlight) and are retrieved with a minimum number of assumptions. Then, using the HDRF's as a starting point, the corresponding bidirectional reflectance factors (BRF's) and the directional-hemispherical reflectances (DHR's) are determined. The BRF's and the DHR's are surface properties assuming direct sunlight illumination only and therefore can only be retrieved if a surface BRF model is assumed. This makes the BRF's and DHR's somewhat more model-dependent than the HDRF's and the BHR's. By using a parameterized BRF model, however, and determining the model parameters, the possibility exists of extrapolating the BRF's and DHR's to other view angles and sun angles not obtainable by MISR.

From the spectral BHR's and DHR's the PAR-integrated BHR and DHR are obtained. The PAR (photosynthetically active radiation) band covers the 400 - 700 nm wavelength range, allowing three of the four MISR channels to be used in the integration. The PAR-integrated BHR and DHR are a measure of the amount of PAR absorbed by the surface (vegetative and non-vegetative) under ambient and direct illumination conditions. The green leaf-area index (LAI) is estimated from a comparison of the retrieved spectral BHR's and the BHR's derived from detailed radiative transfer modeling of the plant canopy biome types specified in the ALB Dataset. All canopy models which pass the BHR comparison test are then tested again by comparing their directional reflectances to the retrieved BRF's. Once the biome type and its LAI are determined, the fractional amount of incident PAR absorbed by the canopy (FPAR) only (and not the understory) is then estimated. For efficiency in execution of the algorithm, all necessary radiative transfer parameters have been precomputed and stored in the Canopy Architecture Radiative Transfer (CART) file, a subset of the Ancillary Land Biome (ALB) Dataset [M-6]. A geographic Biome Classification Map file is also contained in the ALB Dataset. A comparison of the two estimates of FPAR for dense, dark vegetation (DDV) (the retrieved FPAR and the PAR-integrated BHR, which constitutes a more direct determination) will allow an assessment of the accuracy of the Biome Classification Map, at least for DDV.

The ocean surface retrieval process is performed only for the tropical ocean, which for our purpose is limited to a 600 km wide band centered on the geographic equator. Phytoplankton pigment concentration is estimated at a spatial resolution of 1.1 km, using the retrieved water-leaving radiances in the MISR blue and green bands as inputs to the Coastal Zone Color Scanner (CZCS) algorithm. However, these water-leaving radiances are retrieved in two distinct ways. One is the conventional approach, essentially employing the MODIS/SeaWiFS algorithm which has its own collection of aerosol models, and the other, termed experimental, is based on the MISR aerosol retrieval results and MISR surface reflectance retrieval techniques. Pigment concentrations are determined using both sets of water-leaving radiances for later comparison studies.

3. ALGORITHM DESCRIPTION

3.1 PROCESSING OUTLINE

The MISR surface retrieval approach involves inversion of the solution to the radiative transfer equation to convert TOA equivalent reflectances (normalized to an Earth-Sun distance of 1 AU and corrected for ozone absorption) to surface parameters using the aerosol model that is retrieved as described in [M-5]. The processing concepts for land and ocean surface retrievals are shown below. The convention for the various elements displayed in these diagrams is shown in Figure 1.

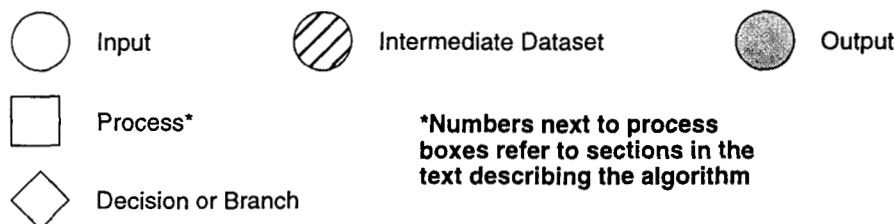


Figure 1. Conventions used in processing flow diagrams

The surface retrieval process is assisted by establishment of four ancillary datasets. The first, the Aerosol Climatology Product (ACP), contains microphysical and scattering characteristics of a set of aerosol types upon which the preceding aerosol retrievals are based, the mixture of pure aerosol types which comprise candidate models used during the aerosol retrievals, along with a geographical and seasonal measure of climatological likelihood of each mixture and information about the mixture that is required during the retrievals. The second, the Simulated MISR Ancillary Radiative Transfer (SMART) Dataset, contains radiation fields used to generate the model top-of-atmosphere (TOA) equivalent reflectances to which the MISR observations are compared during the aerosol retrievals and is generated by performing radiative transfer calculations on stratified atmospheric models containing the aerosols found in the ACP. The calculations contained in the SMART Dataset includes two surface boundary condition cases: (1) oceans or large dark water bodies, and (2) a spectrally black surface. The third, the Ancillary Land Biome Dataset, provides a land surface classification map in addition to the necessary radiative transfer parameters needed to determine LAI and FPAR, based on canopy models for six different biome types. The fourth, the Tropical Ocean Atmospheric Correction (TOAC) Dataset, contains parameters necessary for the generation of atmospheric radiation fields used in the retrieval of ocean color. These datasets are generated prelaunch at the MISR SCF and then delivered to the DAAC. Further details are provided in [M-6].

The remaining elements of the retrieval occur during routine processing at the DAAC. Before a surface retrieval can be performed on a given region, however, a successful aerosol retrieval must be performed first, resulting in one or more acceptable aerosol mixture models which are compatible with the measurements. These models are then used to generate the appropriate atmospheric parameters needed in the surface retrieval.

Figures 2 and 3 depict the processing concept for surface retrieval over land. The core of the process is the determination of the hemispherical-directional reflectance factors (HDRF's) and the associated bihemispherical reflectances (BHR's). From these parameters, flow the majority of the remaining land surface products, e.g., LAI and FPAR.

The conventional and experimental approaches to surface retrieval over ocean are depicted in Figure 4. Both approaches use the MISR-derived aerosol models to apply a correction for glitter and whitecaps. In addition, they are applied only to the MISR B cameras (a compromise between sunglint avoidance and a desired nadir view), and in particular only that B-camera contaminated with the least amount of sunglint (i.e., farthest from the specular direction).

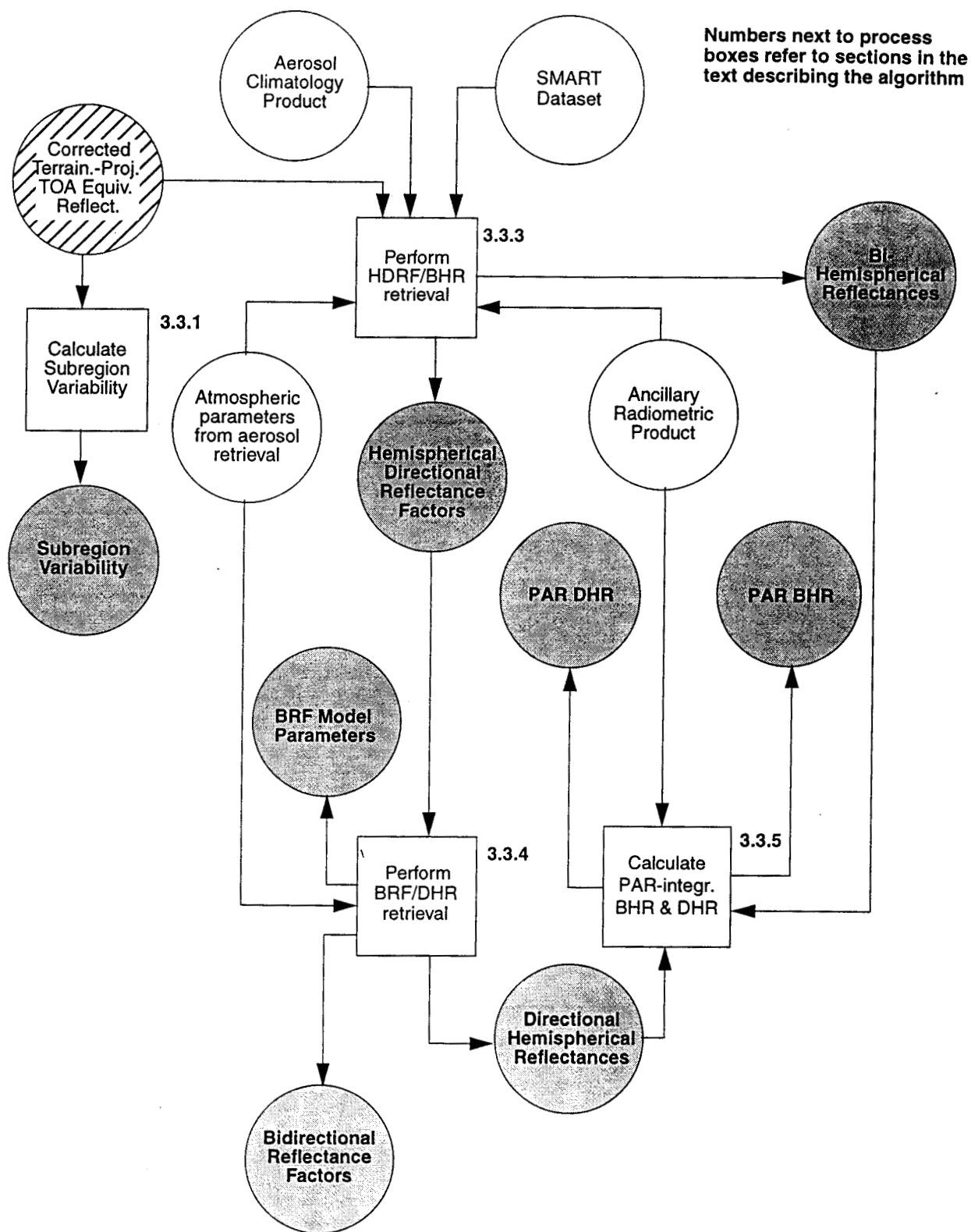


Figure 2. Land surface retrieval processing concept, excepting LAI and FPAR

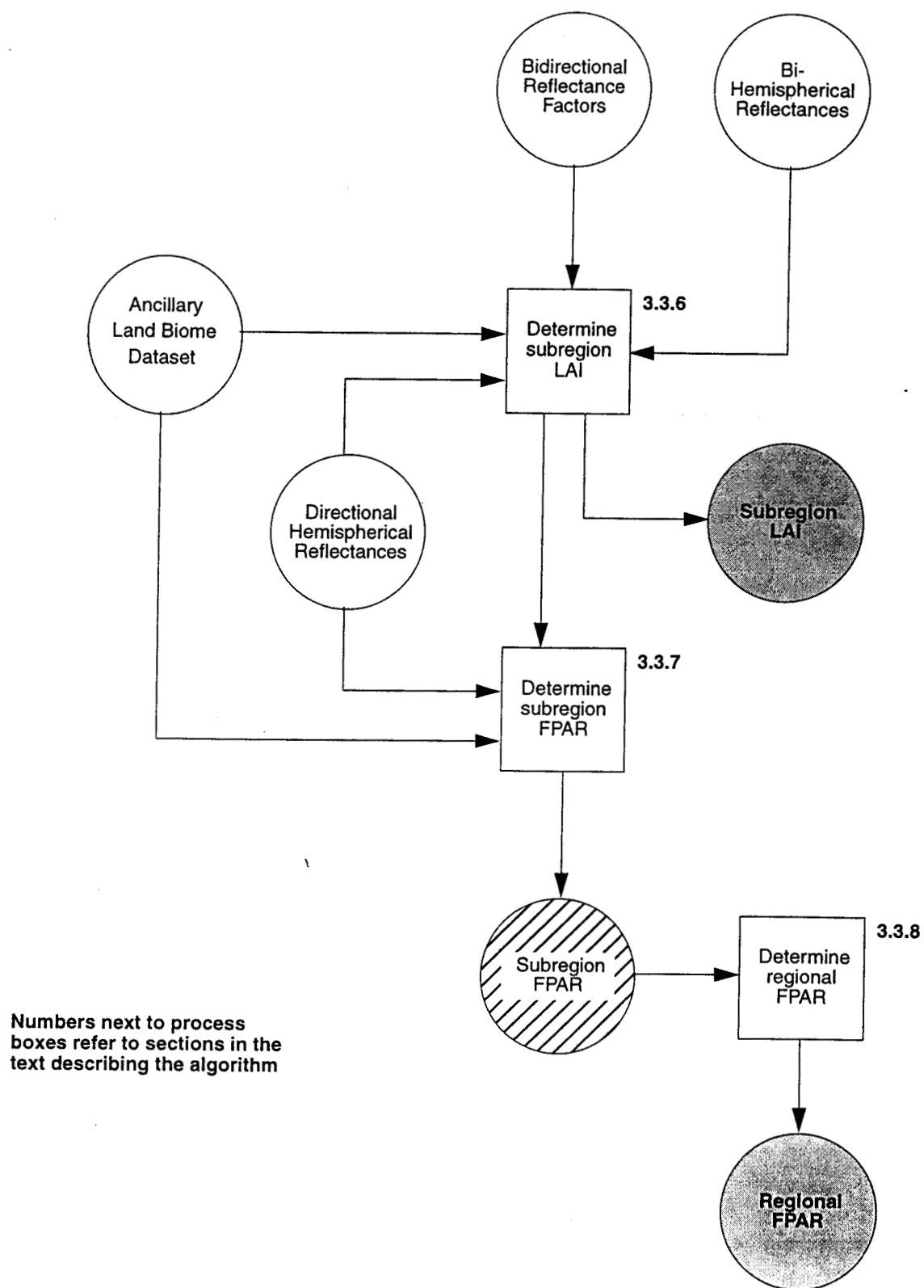


Figure 3. LAI/FPAR retrieval processing concept

Numbers next to process boxes refer to sections in the text describing the algorithm

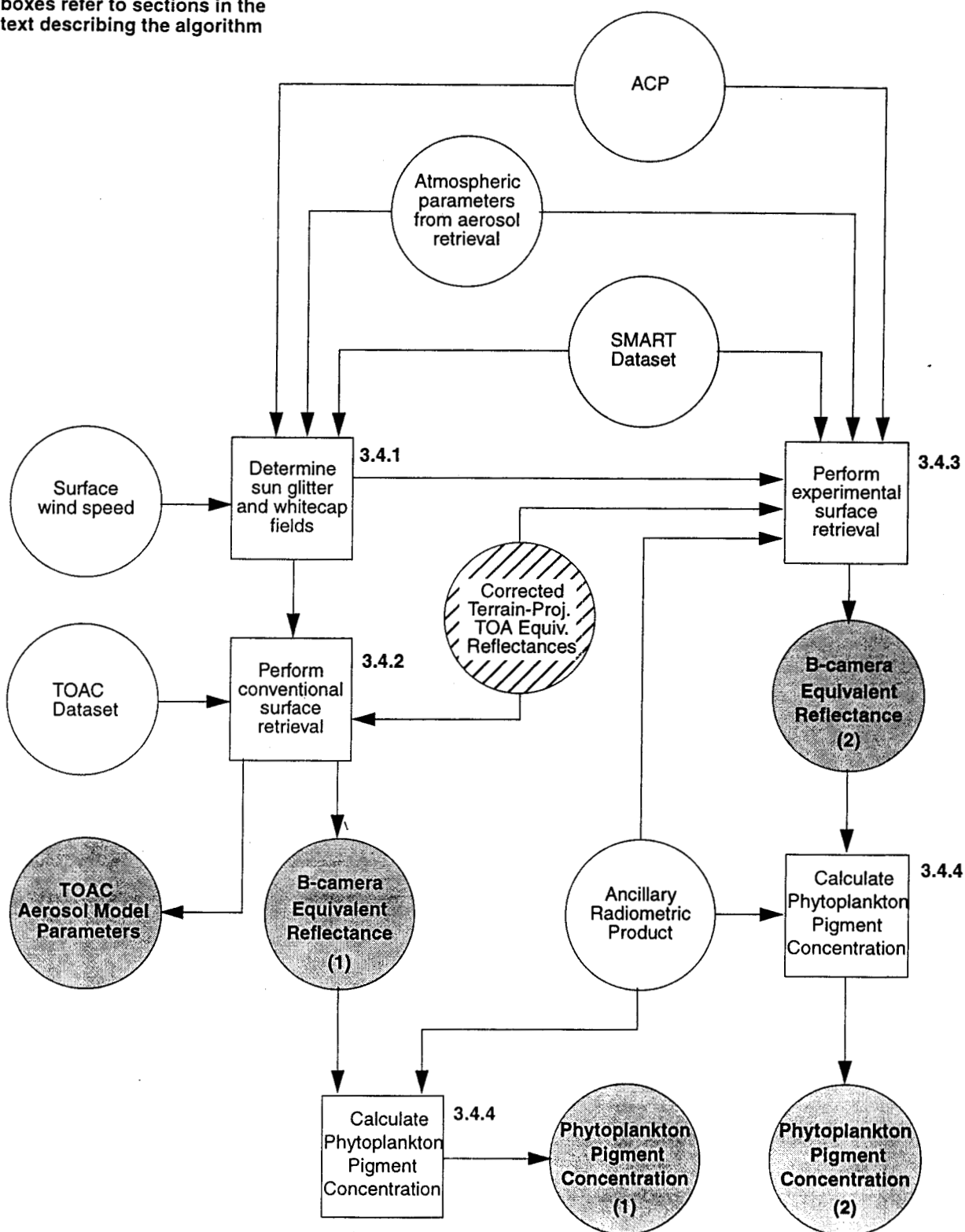


Figure 4. Ocean surface retrieval processing concepts

3.2 ALGORITHM INPUT

3.2.1 MISR data

Required inputs for the surface retrieval to be obtained from the MISR data processing stream (at the DAAC or SCF) are summarized in Table 2. Further information on each of the inputs is provided below.

Table 3: Level 2 Aerosol/Surface Product Inputs (MISR Data) used for surface retrievals

Input data	Source of data	Reference
Corrected terrain-projected TOA equivalent reflectances	Level 1B2, with normalization to Earth-Sun distance of 1 AU and ozone correction applied during aerosol retrieval	[M-5]
Ellipsoid-referenced geometric parameters	Level 1B2 Georectified Radiance Product	[M-3]
Radiometric Data Quality Indicator (RDQI)	Level 1B2 Georectified Radiance Product	[M-3]
Aerosol Retrieval Success Indicator	Aerosol retrieval	[M-5]
Retrieval Applicability Mask	Aerosol retrieval	[M-5]
Retrieved aerosol parameters	Aerosol retrieval	[M-5]
Atmospheric pressure	Passed in from aerosol retrieval	[M-5]
Ancillary aerosol model parameters	Simulated MISR Ancillary Radiative Transfer (SMART) Dataset Aerosol Climatology Product (ACP)	[M-6]
Aerosol models for conventional ocean surface retrieval	Tropical Ocean Atmospheric Correction (TOAC) Dataset	[M-6]
Band-weighted exo-atmospheric solar irradiances	Ancillary Radiometric Product	[M-2]
Canopy radiative transfer parameters	Ancillary Land Biome (ALB) Dataset	[M-6]
Biome Classification Map	Ancillary Land Biome (ALB) Dataset	[M-6]
NDVI-FPAR regression coefficients	Ancillary Land Biome (ALB) Dataset	[M-6]

3.2.1.1 Corrected terrain-projected TOA equivalent reflectances

The terrain-projected TOA radiances are derived at Level 1B2 and consist of geolocated, registered, and calibrated radiances in all 36 channels of the instrument projected onto the surface terrain. The data are resampled onto a Space Oblique Mercator grid. The corrected terrain-projected TOA equivalent reflectances are normalized to an Earth-Sun distance of 1 AU, corrected for ozone absorption, converted from radiances to equivalent reflectances according to Eq. (30), and have a spectral out-of-band correction applied. See [M-5].

3.2.1.2 Ellipsoid-referenced geometric parameters

These are calculated at Level 1B2 and provide view zenith and azimuth angles as well as solar zenith and azimuth angles, each referenced to the surface ellipsoid.

3.2.1.3 Radiometric Data Quality Indicator

A Radiometric Data Quality Indicator (RDQI) will be associated with each projected radiance provided by Level 1B2. This indicator will provide a representation of the radiometric quality of the input radiances used to generate values reported in the Geo-rectified Radiance Product. Because of the data resampling required at Level 1B2, each projected radiance represents a bilinear interpolation of four surrounding radiances obtained from the MISR images. The radiances in the imagery will be coded with a quality indicator specifying the reliability level of the radiometry on a pixel-by-pixel basis. From these, a scaled value will be produced at Level 1B2. The RDQI's take on values of 0 - 3, as follows:

RDQI = 0: Radiometric accuracy meets all specifications

RDQI = 1: Radiometric accuracy is sufficient for certain applications but some specifications are violated (see [M-2] and [M-3])

RDQI = 2: Radiance value is available but of insufficient accuracy to be used in Level 2 retrievals

RDQI = 3: Radiance value is unavailable.

Thus, higher quality data are associated with smaller values of RDQI.

In addition to the RDQI's, radiances reported in Level 1B2 will be encoded to provide Data Flag information, for example, to indicate that a particular point on the Space Oblique Mercator (SOM) grid was topographically obscured from view by a particular camera.

Finally, MISR data will have an associated Geometric Data Quality Indicator (GDQI). The GDQI will provide a measure of how much image matching was used to insure high-quality image registration, relative to a pure reliance on spacecraft-supplied navigation.

Surface retrievals are only performed on subregions for which the $RDQI \leq RDQI_1$. We set $RDQI_1$ to 0.

3.2.1.4 Aerosol Retrieval Success Indicator

Each 17.6 km x 17.6 km region has an associated indicator which describes the status of the aerosol retrieval process. If no successful aerosol retrieval was performed, the reason is indicated, such as no acceptable aerosol model was found, a failure in the algorithm code, or no retrieval was

attempted. Reasons for not attempting a retrieval include the region being too topographically complex, too cloudy, or having no acceptable 1.1 km x 1.1 km subregions. A successful aerosol retrieval must be done as a prerequisite to performing any type of surface retrieval.

3.2.1.5 Retrieval Applicability Mask

This mask, covering the 16 x 16 array of subregions within a 17.6 km x 17.6 km region, is generated for each of the 36 channels of MISR and indicates whether the associated equivalent reflectances are acceptable for use in an aerosol or surface retrieval. If an equivalent reflectance is rated unacceptable, the mask value also indicates the reason for rejection, such as poor radiometric quality, glitter contamination, etc. The criteria for rejecting a particular subregion for usage in a surface retrieval are the same as for an aerosol retrieval, with one exception. If the Aerosol Retrieval Success Indicator says that a successful aerosol retrieval was obtained for a particular region, and certain subregions and channels within that region have been eliminated for use during the aerosol retrieval, they will usually be considered unacceptable for surface retrieval as well. The exception is that subregions and channels which were deemed of unacceptable radiometric quality for aerosol retrieval may be considered acceptable for surface retrieval, depending on the values established for the RDQI thresholds.

3.2.1.6 Retrieved aerosol parameters

These parameters include the column aerosol optical depth and aerosol compositional model identifiers (model types) as determined from the MISR aerosol retrieval. They define which sections of the Simulated MISR Ancillary Radiative Transfer (SMART) Dataset and the Aerosol Climatology Product (ACP) are interrogated for the atmospheric inputs to the surface retrieval. See [M-5] and [M-6].

3.2.1.7 Atmospheric pressure

This parameter is used during aerosol retrievals and passed to surface processing in order to calculate the Rayleigh scattering optical depth at each wavelength.

3.2.1.8 Ancillary aerosol model parameters

These parameters consist of inputs from the SMART Dataset, including aerosol optical depth, equivalent reflectance corresponding to atmospheric path radiance, upward diffuse atmospheric transmittance, diffuse irradiance, and bottom-of-atmosphere (BOA) bihemispherical albedo; and inputs from the ACP, including aerosol fractional amounts, optical depth spectral scaling factors, and single scattering albedos for aerosol mixtures, and particle extinction cross sections and single scattering albedos for pure particles.

3.2.1.9 Aerosol models for conventional ocean surface retrieval

The Tropical Ocean Atmospheric Correction (TOAC) Dataset contains coefficients describing a specialized set of aerosol models that are to be used for ocean retrievals from SeaWiFS and MODIS. They are implemented here as well to facilitate the conventional ocean surface retrieval algorithm.

3.2.1.10 Band-weighted exo-atmospheric solar irradiances

These are obtained from the Ancillary Radiometric Product (ARP) and used in the calculation of phytoplankton pigment concentration to convert equivalent reflectances to radiances. Because a correction for out-of-band radiation has been applied to the equivalent reflectances prior to aerosol and surface retrieval, the standardized, in-band weighted values, denoted $E_{0,b}^{std, in-band}$, are used.

3.2.1.11 Canopy radiative transfer parameters

These parameters consists of inputs from the Canopy Architecture Radiative Transfer (CART) file in the ALB, and include canopy upward and downward directed transmittances and absorptances at a reference wavelength, transmittance and absorptance coefficients depending only on the canopy structure, and spectral leaf albedo. They are used in the LAI/FPAR algorithm to readily compute spectrally dependent transmittance, reflectance, and absorptance parameters of complex, biome-dependent canopy models. Further information pertaining to the content of this file is presented in [M-6].

3.2.1.12 Biome Classification Map

This 1.1 km resolution, SOM projected, Biome Classification Map is a file in the ALB. It is used by the LAI/FPAR algorithm when in the default mode. This occurs when no satisfactory identification of biome type can be made and the Biome Classification Map is then used as input to an NDVI-FPAR regression analysis. Further information pertaining to the content of this file is presented in [M-6].

3.2.1.13 NDVI-FPAR regression coefficients

This file contains the coefficients necessary to perform an NDVI-FPAR regression analysis. Further information pertaining to the content of this file is presented in [M-6].

3.2.2 Non-MISR data

Required inputs for the ocean surface retrieval to be obtained from non-MISR sources are

summarized in Table 3. Further information on each of the inputs is provided below.

Table 4: Aerosol/Surface Product inputs (non-MISR data)

Input data	Source of data
Surface wind speed	EOS Data Assimilation Office (DAO) or TASC Dataset

3.2.2.1 Surface wind speed

A model of water surface roughness with wind speed as a parameter is used in the calculation of TOA equivalent reflectances over dark water (defined to be the open ocean and the middle of large lakes, away from coastal boundaries). Therefore, the surface wind speed parameter is used to select the appropriate ocean surface model in the SMART Dataset, needed in the ocean retrieval for establishing the sunglint and whitecap contributions.

3.3 THEORETICAL DESCRIPTION OF LAND SURFACE RETRIEVALS

Several processes which occur during the land surface retrievals are indicated in §3.1 (in particular Figure 2). In the following sections, the physical basis of these processes and a mathematical description of the algorithm which is used to implement each process is presented. The following processes are performed only on those subregions which have been deemed acceptable for surface retrieval (see §3.2.1.4 and §3.2.1.5).

Note that the process described in §3.3.2 is provided for information only, and the calculations are not performed during retrievals at the DAAC. The reason for this is that (a) the resulting information is not used during the retrievals, (b) the parameters require a large data volume to archive, and (c) the parameters may be readily calculated from available products. Because the data are useful to users, however, the equations for calculating the indicated parameters are included in this document.

3.3.1 Calculate Subregion Variability

3.3.1.1 Physics of the problem

The Subregion Variability, a retrieval quality assessment parameter, is the standard deviation of the nadir equivalent reflectances within each 1.1-km land surface subregion divided by the mean value, and makes use of the 4 x 4 array of 275-m values within each 1.1-km surface sample, for each band of the MISR nadir camera, on the SOM grid. As this parameter is designed to provide a relative measure of subregion contrast, an atmospheric correction is not applied. However, the result of computing the standard deviation removes any horizontally uniform fields within the 1.1-km subregion. The atmospheric path radiance and, to a large extent, diffusely transmitted radiation

from the surface to the top-of-the-atmosphere fall into this category. Therefore, the Subregion Variability provides a measure of surface contrast. Low values of this parameter will indicate those places where angle-to-angle misregistration effects will be minimal.

3.3.1.2 Mathematical description of the algorithm

At each wavelength, the Subregion Variability v is given by:

$$v = \frac{\sqrt{\langle \rho^2(nadir) \rangle - \langle \rho(nadir) \rangle^2}}{\langle \rho(nadir) \rangle} \quad (1)$$

where

$$\begin{aligned} \langle \rho(nadir) \rangle &= \sum_{x,y} [\rho_{x,y}(nadir) \cdot q_{x,y}(nadir)] / \sum_{x,y} q_{x,y}(nadir) \\ \langle \rho^2(nadir) \rangle &= \sum_{x,y} [\rho_{x,y}^2(nadir) \cdot q_{x,y}(nadir)] / \sum_{x,y} q_{x,y}(nadir) \end{aligned} \quad (2)$$

Here, $\rho_{x,y}$ is the corrected, terrain-projected, equivalent reflectance for nadir view at coordinates x,y within a subregion and $q_{x,y} = 1$ if the associated $RDQI \leq RDQI_1$; otherwise $q_{x,y} = 0$. The summations are over the 4 x 4 array of 275 m samples within the subregion.

3.3.1.3 Archived algorithm output

A value of v is computed for each 1.1 km land subregion and each MISR wavelength band at which unaveraged (275-m sample size) equivalent reflectances are acquired by the nadir camera and is archived as a Retrieval Quality Indicator parameter.

3.3.2 Sun and view angles for inclined surfaces

3.3.2.1 Physics of the problem

Because the surface topography is variable within the footprints of the MISR observations, the effects of terrain slope are useful in evaluating the surface retrievals. The primary effects of a sloped or tilted terrain include the dependence of irradiance (both direct and diffuse), upward transmittance, and possibly surface BRDF (e.g., for a vegetated surface) on the tilt angle (slope). Some of these effects have been studied insofar as how they impact the classification accuracy of forest canopies (see, e.g., [6], [43]). A more general analysis was done by Woodham and Lee [47], who devised a 6-parameter model of surface reflectance to account for slope effects. Using this model, Gray [22] reported that the classification accuracy for a forested area increased from 51% (uncor-

rected Landsat MSS data) to 80% with correction for solar incidence angle providing the largest effect.

If the slope is kept under 20° , the atmospheric parameters associated with diffuse scattering seem to depend only slightly on the slope angle [5]. MISR aerosol retrievals are confined to this situation, and are not performed over rugged terrain. When a region (17.6 km x 17.6 km) has a complex terrain, that is, the standard deviation of the elevation of the subregions exceeds 250 m, an aerosol retrieval will not have been performed [M-5]. Surface parameters will consequently be retrieved only for subregions with slopes within the slope limit, using the Retrieval Applicability Mask generated during aerosol retrievals to filter out more rugged terrain. Thus, the MISR surface retrievals do not explicitly incorporate tilt or slope effects. Instead, in every 1.1 km land subregion where a retrieval is performed, the surface leaving radiance is considered to transition an imaginary horizontal surface (i.e., a surface parallel to the ellipsoid). Therefore, the MISR land surface retrieval algorithms are performed relative to this hypothetical surface.

Despite the approach taken for MISR surface retrievals, the surfaces over each 1.1-km land-surface sample for which surface retrievals will be performed will in general be inclined with respect to the Earth's reference ellipsoid. As a result, the view angles at the surface for each of the nine MISR cameras, as well as the solar incidence angle at the surface, will vary from sample to sample. This information is therefore useful to interpreters of the retrieved surface parameters. However, the required parameters may be readily calculated from data provided by the MISR Ancillary Geographic Product (AGP) and the Level 1B2 ellipsoid-referenced geometric parameters. Archival of the parameters requires a large data volume. Consequently, we have opted to provide within this document, for the benefit of MISR data users, the algorithm needed to calculate terrain-referenced geometric parameters. This algorithm is not implemented at the DAAC.

3.3.2.2 Mathematical description of the algorithm

The MISR AGP provides, on 1.1-km centers, the zenith and azimuth angles of the vector describing the surface normal (θ_n and ϕ_n , respectively), in a coordinate system in which the z-axis is aligned with the normal to the surface reference ellipsoid (defined by the World Geodetic System 1984, WGS84), and points toward the center of the Earth. The Level 1B2 Product provides, on 17.6-km centers, the zenith and azimuth angles of the direction of illumination by the Sun (θ_0 and ϕ_0 , respectively) and the direction to each of the nine cameras (θ_j and ϕ_j , respectively, for the j^{th} camera) relative to the ellipsoid. The latter set of parameters are reported on 17.6-km centers because these quantities vary slowly on this scale. However, since the surface slope can change significantly over 1.1 km, the solar and view vectors relative to the actual surface orientation must be calculated at the 1.1-km resolution.

A right-handed coordinate system is defined in which the z-axis is co-aligned with the normal to the Earth's ellipsoid and pointing downward, the x-axis is aligned with a great circle and

points toward the north pole, and the y-axis is orthogonal to both of these. The following vectors are defined in this coordinate system:

$$\hat{n} = \begin{bmatrix} \sin\theta_n \cos\phi_n \\ \sin\theta_n \sin\phi_n \\ \cos\theta_n \end{bmatrix} \quad \hat{s} = \begin{bmatrix} \sin\theta_0 \cos\phi_0 \\ \sin\theta_0 \sin\phi_0 \\ \cos\theta_0 \end{bmatrix} \quad \hat{v}_j = \begin{bmatrix} \sin\theta_j \cos\phi_j \\ \sin\theta_j \sin\phi_j \\ \cos\theta_j \end{bmatrix} \quad (3)$$

where \hat{n} is the unit vector describing the orientation of the normal to the surface terrain, \hat{s} is the unit vector describing the direction of solar illumination, and \hat{v}_j is the unit vector describing the backward view direction (i.e., from the Earth to the camera) of the j^{th} camera. Then, the cosine of the view angle relative to the local normal, denoted η , the cosine of the Sun angle relative to the local normal, denoted η_0 , and the scattering angle Ω are calculated from

$$\eta_j = \hat{n} \cdot \hat{v}_j \quad \eta_0 = -\hat{n} \cdot \hat{s} \quad \cos\Omega_j = \hat{s} \cdot \hat{v}_j \quad (4)$$

and the relative azimuth difference between the view and incident directions, $\Delta\xi_j$, is given by

$$\cos\Delta\xi_j = \frac{\cos\Omega_j - \eta_j\eta_0}{\sqrt{1-\eta_j^2}\sqrt{1-\eta_0^2}} \quad (5)$$

The terrain-dependent Sun and view geometry parameters, η_0 and the $(\eta, \Delta\xi)$ pair for each MISR camera, may be computed for each 1.1 km land subregion. They are not archived.

3.3.3 Retrieve HDRF and BHR

3.3.3.1 Physics of the problem

Hemispherical-directional reflectance factors (HDRF's) and bihemispherical reflectances (BHR's) (or albedos), which include the effects of both direct and diffuse illumination at the bottom of the atmosphere, are most appropriately used in the description of the lower boundary condition in climate studies. The HDRF product is essentially a measure of surface-leaving radiance at the nine MISR view angles and four wavelengths for the particular sun geometry of the observations. This kind of data currently is being obtained for very localized areas as part of sporadically timed field experiments, using hand-held radiometers with footprint sizes of less than a meter (see, e.g., Starks et al. [42]). In contrast, MISR will provide HDRF's and BHR's systematically with a footprint size of 1.1 km over most of the global land surface during the life of the EOS-AM mission, nominally six years. The retrieval algorithm presented below simultaneously retrieves the spectral HDRF and BHR. Therefore, although these are archived as separate parameters, a single

algorithm for their derivation is described.

The derivation assumes that scattering and absorption of sunlight within the atmosphere is adequately described by radiative transfer theory [7]. In general, attenuation of the incident and reflected beams as a result of extinction (scattering and absorption) along the ray path is somewhat offset by diffuse radiation that has been (1) reflected by the atmosphere without reaching the surface, (2) subjected to multiple reflections between the atmosphere and surface, and (3) scattered into the line-of-sight from neighboring terrain. The top-of-atmosphere radiance field depends on both the optical characteristics of the atmosphere and the reflectance properties (spatial, spectral, and angular) of the surface. The solution to the radiative transfer equation is an integral expression which must be solved for the surface reflectance. At the bottom of the atmosphere, the surface is illuminated by radiation which has been both directly and diffusely transmitted through the atmosphere, as well as by backscattered light from the surface. The diffuse radiation field illuminating the surface is known as skylight, and illuminates the surface from all angles in the downward hemisphere. In contrast, directly transmitted sunlight is more or less uni-directional (except for the finite angular size of the Sun, which can be ignored for practical purposes).

An implicit assumption of the surface retrieval algorithms is that each of the 36 view-dependent MISR radiances is associated with the same ground footprint, particularly with regard to size. At the highest resolution, the geometric crosstrack footprint dimension of each camera is virtually the same, about 275 m, as a consequence of the particular camera effective focal length. However, surface projection effects increase the geometric along-track footprint dimension with increasing view angle. Thus, the D camera along-track instantaneous footprint dimension at the highest resolution (excluding smear due to the finite integration time) is three times that of the off-nadir A cameras (707 m versus 236 m) but the along-track sample spacing is still 275 m. When the high resolution samples are averaged 4 x 4 to create an averaged sample with a crosstrack dimension of 1.1 km, the surface projection effect is substantially mitigated for the averaged sample along-track dimension, due to the 275 m high resolution sample spacing. Thus, averaged samples from the D, C, and B cameras are only 17%, 11%, and 6% geometrically larger, respectively, than averaged samples from the A cameras. These variations in footprint size are not considered significant and so the 4 x 4 averaged (1.1 km x 1.1 km) samples (called subregions) from all nine cameras are treated in the retrieval process as having identical ground footprints.

3.3.3.2 Mathematical description of the algorithm

For a radiometrically calibrated satellite image, the radiance $L_{x,y}$ leaving the top of the atmosphere can be written as

$$\begin{aligned}
L_{x,y}(-\mu, \mu_0, \phi - \phi_0) = & L^{atm}(-\mu, \mu_0, \phi - \phi_0) \\
& + e^{-\tau/\mu} \cdot \frac{1}{\pi} \int_0^{12\pi} \int_0^{12\pi} R_{x,y}(-\mu, \mu', \phi - \phi') L_{x,y}^{inc}(\mu', \mu_0, \phi' - \phi_0) \mu' d\mu' d\phi' \\
& + \frac{1}{\pi} \int_0^{12\pi} \int_0^{12\pi} \int_0^{12\pi} \int_0^{12\pi} T_{x,y}(-\mu, -\mu'', \phi - \phi'') \otimes R_{x,y}(-\mu'', \mu', \phi'' - \phi') L_{x,y}^{inc}(\mu', \mu_0, \phi' - \phi_0) \mu' d\mu'' d\phi'' d\mu' d\phi'
\end{aligned} \tag{6}$$

where x, y are the image spatial coordinates, μ and μ_0 are the cosines of the view and Sun angles, defined with respect to the normal to the surface ellipsoid (not the local topographically-defined surface orientation) and $\phi - \phi_0$ is the view azimuthal angle with respect to the Sun position, also in the ellipsoid reference system. The convention $-\mu$ and μ is used for upwelling and downwelling radiation respectively. The properties of the atmosphere are assumed to be horizontally homogeneous. On the right-hand-side of Eq. (6), L^{atm} is the radiance scattered by the atmosphere to space without interacting with the surface (i.e., the path radiance), τ is the optical depth of the atmosphere, $L_{x,y}^{inc}$ is the direct and diffuse downward radiance incident on the surface, $T_{x,y}$ is the upward diffuse transmittance, and $R_{x,y}$ is the spatially variable surface bidirectional reflectance factor (BRF). The BRF of a surface target is defined as the bidirectional reflectance distribution function of the target ratioed to the bidirectional reflectance distribution function from a non-absorbing lambertian surface [35]. Note that the TOA radiance $L_{x,y}$ has been normalized to a 1 AU Earth-Sun distance and corrected for the effects of ozone absorption as described in [M-5]. Also, all the parameters in Eq. (6) are a function of wavelength, but this dependence has been suppressed in the notation for simplicity.

In the general three-dimensional solution to the radiative transfer problem with a horizontally uniform atmosphere over a spatially varying and flat surface, the transmittance $T_{x,y}$ can be thought of as a point-spread function and with the convolution operation \otimes describes the blurring effect of the atmosphere on the surface reflectance $R_{x,y}$ [14]. When the image spatial resolution is comparable to the atmospheric scattering scale height (defined by the vertical distribution of the aerosols and/or Rayleigh scattering molecules), Eq. (6) reduces to the standard one-dimensional radiative transfer regime, and $T_{x,y}$ is effectively a delta function in the spatial coordinates. In this case, Eq. (6) simplifies to:

$$\begin{aligned}
L_{x,y}(-\mu, \mu_0, \phi - \phi_0) = & L^{atm}(-\mu, \mu_0, \phi - \phi_0) \\
& + e^{-\tau/\mu} \cdot \frac{1}{\pi} \int_0^{12\pi} \int_0^{12\pi} R_{x,y}(-\mu, \mu', \phi - \phi') L_{x,y}^{inc}(\mu', \mu_0, \phi' - \phi_0) \mu' d\mu' d\phi' \\
& + \frac{1}{\pi} \int_0^{12\pi} \int_0^{12\pi} \int_0^{12\pi} \int_0^{12\pi} T(-\mu, -\mu'', \phi - \phi'') R_{x,y}(-\mu'', \mu', \phi'' - \phi') L_{x,y}^{inc}(\mu', \mu_0, \phi' - \phi_0) \mu' d\mu'' d\phi'' d\mu' d\phi'
\end{aligned} \tag{7}$$

A principal assumption in the surface retrieval process is that the state of the atmosphere is known (i.e., from the aerosol parameters in the Aerosol/Surface Product, which are used as input to the surface retrievals) such that the various atmosphere-dependent functions, e.g., T and $L_{x,y}^{inc}$ in Eq. (6) or (7), can be determined. Whether Eq. (6) or (7) is used in the surface retrieval process depends on the spatial scale of the contrast in the scene. Over ocean the 1-D radiative transfer description of the TOA radiance, described by Eq. (7), is appropriate, due mainly to a lack of contrast on the ocean surface. Over land, however, there can be significant surface contrast and aerosol scale heights are about 1 - 2 km, comparable to the surface spatial resolution, leading to adjacency effects. Nevertheless, by virtue of the 1.1-km sample size, we assume that Eq. (7) is sufficiently accurate such that surface retrievals are not significantly compromised by not using Eq. (6). This assumption has been tested using a 3-D radiative transfer algorithm [12], [13], [15] on a scene with a high-contrast boundary (a coastline). The results of these tests indicate that at the spatial resolution corresponding to unaveraged MISR data (275 m), and especially at high spatial resolution (30 m or finer) obtained with sensors such as the Landsat Thematic Mapper, SPOT, or ASTER, the use of Eq. (7) can lead to errors larger than those resulting from expected uncertainties in the aerosol model. At the 1.1-km sample size, the errors resulting from the use of 1-D radiative transfer theory are similar in magnitude to errors in the aerosol model. Therefore, until we are confident that aerosol retrieval errors can be minimized, we do not consider the additional complexities of including 3-D radiative transfer theory to be warranted. However, users with extremely stringent accuracy requirements on surface retrievals would be advised to use the Subregion Variability to identify areas with low contrast, such that adjacency effects do not play a significant role.

The description of the HDRF/BHR retrieval algorithm begins with a definition of the *hemispherical-directional reflectance factor for non-isotropic incident radiation*, hereafter referred to as the HDRF. It can be written as

$$r_{x,y}(-\mu, \mu_0, \phi - \phi_0) = \frac{\frac{1}{\pi} \int_0^{2\pi} \int_0^1 R_{x,y}(-\mu, \mu', \phi - \phi') L_{x,y}^{inc}(\mu', \mu_0, \phi' - \phi_0) \mu' d\mu' d\phi'}{\frac{1}{\pi} \int_0^{2\pi} \int_0^1 L_{x,y}^{inc}(\mu', \mu_0, \phi' - \phi_0) \mu' d\mu' d\phi'} \quad (8)$$

and is the ratio of the radiance reflected from the surface to that from an ideal lambertian target reflected into the same beam geometry and illuminated under identical atmospheric conditions. The surface irradiance $E_{x,y}$ is proportional to the denominator of Eq. (8), and is defined as

$$E_{x,y}(\mu_0) = \int_0^{2\pi} \int_0^1 L_{x,y}^{inc}(\mu', \mu_0, \phi' - \phi_0) \mu' d\mu' d\phi' \quad (9)$$

A related irradiance is the black surface irradiance, E_b ,

$$E_b(\mu_0) = E_b^{dir}(\mu_0) + E_b^{diff}(\mu_0) = \int_0^1 \int_0^{2\pi} L_b^{inc}(\mu', \mu_0, \phi' - \phi_0) \mu' d\mu' d\phi' \quad (10)$$

where E_b^{dir} and E_b^{diff} are the direct and diffuse components, respectively, and L_b^{inc} is the downwelling radiance when the surface reflectance is identically zero. Thus L_b^{inc} is a surface-independent parameter since no multiple reflections of radiation between surface and atmosphere are possible. On the other hand, $L_{x,y}^{inc}$ in Eq. (9) does contain all of the multiple reflection contributions to the downward radiance and therefore is dependent on the surface BRDF, $R_{x,y}$.

Associated with the surface irradiance $E_{x,y}$ is the radiant exitance at the surface, $M_{x,y}$, expressed as

$$\begin{aligned} M_{x,y}(\mu_0) &= \frac{1}{\pi} \int_0^1 \int_0^{2\pi} \int_0^1 \int_0^{2\pi} R_{x,y}(-\mu, \mu', \phi - \phi') L_{x,y}^{inc}(\mu', \mu_0, \phi' - \phi_0) \mu' d\mu' d\phi' \mu d\mu d\phi \\ &= \int_0^1 \int_0^{2\pi} L_{x,y}^{refl}(-\mu, \mu_0, \phi - \phi_0) \mu d\mu d\phi \end{aligned} \quad (11)$$

where the surface-leaving radiance, $L_{x,y}^{refl}$, is given as

$$L_{x,y}^{refl}(-\mu, \mu_0, \phi - \phi_0) = \frac{1}{\pi} \int_0^1 \int_0^{2\pi} R_{x,y}(-\mu, \mu', \phi - \phi') L_{x,y}^{inc}(\mu', \mu_0, \phi' - \phi_0) \mu' d\mu' d\phi' \quad (12)$$

Now when Eq. (8) is averaged over projected view solid angle, the result, $A_{x,y}^{hem}$, is the *bihemispherical reflectance for non-isotropic incident radiation* or BHR, i.e.,

$$\begin{aligned} A_{x,y}^{hem}(\mu_0) &= \frac{1}{\pi} \int_0^1 \int_0^{2\pi} r_{x,y}(-\mu, \mu_0, \phi - \phi_0) \mu d\mu d\phi \\ &= \frac{M_{x,y}(\mu_0)}{E_{x,y}(\mu_0)} \end{aligned} \quad (13)$$

Thus, the BHR is the ratio of the radiant exitance to the irradiance.

The surface-dependent irradiance $E_{x,y}$ can be related to the black surface irradiance E_b via

the highly accurate approximation

$$E_{x,y}(\mu_0) = \frac{E_b(\mu_0)}{1 - A_{x,y}^{hem}(\mu_0) \cdot s} \quad (14)$$

where s , the *bottom-of-atmosphere (BOA) bihemispherical albedo for isotropic incident radiation*, is defined as

$$s = \frac{1}{\pi^2} \int_0^{12\pi} \int_0^{12\pi} \int_0^{12\pi} \hat{\rho}^{atm}(\mu, -\mu', \phi - \phi') \mu d\mu d\phi d\mu' d\phi' \quad (15)$$

and $\hat{\rho}^{atm}$ is the BOA atmospheric path radiance expressed as an equivalent reflectance. For a given aerosol model, the parameters s and E_b are computed from information contained in the SMART Dataset, allowing the surface-dependent irradiance $E_{x,y}$ to be computed on a subregional scale (1.1 km centers), using Eq. (14). Combining Eqs. (13) and (14), the expression for $A_{x,y}^{hem}$ then can be recast as

$$A_{x,y}^{hem}(\mu_0) = \frac{M_{x,y}(\mu_0)}{E_b(\mu_0) + s \cdot M_{x,y}(\mu_0)} \quad (16)$$

Retrievals of the HDRF and the BHR are coupled together within a common algorithm which is based on Eq. (7). Rewriting this equation in terms of the surface-leaving radiance $L_{x,y}^{refl}$, using Eq. (12), we have

$$\begin{aligned} L_{x,y}(-\mu, \mu_0, \phi - \phi_0) &= L^{atm}(-\mu, \mu_0, \phi - \phi_0) + e^{-\tau/\mu} \cdot L_{x,y}^{refl}(-\mu, \mu_0, \phi - \phi_0) \\ &+ \int_0^{12\pi} \int_0^{12\pi} T(-\mu, -\mu', \phi - \phi') L_{x,y}^{refl}(-\mu', \mu_0, \phi' - \phi_0) d\mu' d\phi' \end{aligned} \quad (17)$$

where τ is the total atmospheric optical depth, given as the sum of the Rayleigh and aerosol components. The Rayleigh component is calculated using Eq. (21) in [M-6], and the aerosol optical depth results from aerosol retrieval processing. This integral equation can be solved for $L_{x,y}^{refl}$ by starting with an initial estimate and converging to the solution via iteration. A good initial estimate, $L_{x,y}^{refl(0)}$, is made by using Eq. (17), but with $L_{x,y}^{refl}$ in the diffuse transmittance term brought outside the integral. Then, we can write

$$L_{x,y}^{refl(0)}(-\mu, \mu_0, \phi - \phi_0) = \frac{L_{x,y}(-\mu, \mu_0, \phi - \phi_0) - L^{atm}(-\mu, \mu_0, \phi - \phi_0)}{e^{-\tau/\mu} + t(-\mu)} \quad (18)$$

where

$$t(-\mu) = \int_0^1 \int_0^{2\pi} T(-\mu, -\mu', \phi - \phi') d\mu' d\phi' \quad (19)$$

To get an initial estimate of the BHR, $A_{x,y}^{hem(0)}$, by means of Eq. (16), an estimate of the radiant exitance, $M_{x,y}^{(0)}$ must first be made by using $L_{x,y}^{refl(0)}$ in Eq. (11). Note that, in general, $L_{x,y}^{refl}$ is determined only at the view angle geometry of the observations whereas Eq. (11) involves integration over the entire view angle hemisphere. This integration is facilitated, however, by assuming a simple azimuth angle model for $L_{x,y}^{refl}$, namely

$$L_{x,y}^{refl}(-\mu, \mu_0, \phi - \phi_0) = L_{0,x,y}^{refl}(-\mu, \mu_0) + L_{1,x,y}^{refl}(-\mu, \mu_0) \cdot \cos(\phi - \phi_0) \quad (20)$$

Note that this simple expansion, which is independent of any specific physical or parametric surface model, is adequate and highly accurate for the purposes for which it is used, namely retrieval of HDRF and BHR [30]. Later (see §3.3.4), a more sophisticated model is invoked to take into account the angular distribution of incident skylight.

Now, using Eq. (20),

$$L_{0,x,y}^{refl}(-\mu, \mu_0) = \frac{L_{x,y}^{refl}(-\mu, \mu_0, \phi_a - \phi_0) \cos(\phi_f - \phi_0) - L_{x,y}^{refl}(-\mu, \mu_0, \phi_f - \phi_0) \cos(\phi_a - \phi_0)}{\cos(\phi_f - \phi_0) - \cos(\phi_a - \phi_0)} \quad (21)$$

$$L_{1,x,y}^{refl}(-\mu, \mu_0) = \frac{L_{x,y}^{refl}(-\mu, \mu_0, \phi_f - \phi_0) - L_{x,y}^{refl}(-\mu, \mu_0, \phi_a - \phi_0)}{\cos(\phi_f - \phi_0) - \cos(\phi_a - \phi_0)} \quad (22)$$

where ϕ_f and ϕ_a are the two azimuth angles for each fore-aft camera pair. Eq. (11) for $M_{x,y}$ can then be rewritten in terms of $L_{0,x,y}^{refl}$ as

$$M_{x,y}(\mu_0) = 2\pi \int_0^1 L_{0,x,y}^{refl}(-\mu, \mu_0) \mu d\mu \quad (23)$$

Once $L_{x,y}^{refl(0)}$ is computed from Eq. (18), it is used in Eq. (17) to update $L_{x,y}^{refl}$ via the iteration scheme

$$L_{x,y}^{refl(n+1)}(-\mu, \mu_0, \phi - \phi_0) = [L_{x,y}(-\mu, \mu_0, \phi - \phi_0) - L^{atm}(-\mu, \mu_0, \phi - \phi_0)] \cdot e^{\tau/\mu} - \left[\int_0^1 \int_0^{2\pi} T(-\mu, -\mu', \phi - \phi') L_{x,y}^{refl(n)}(-\mu', \mu_0, \phi' - \phi_0) d\mu' d\phi' \right] \cdot e^{\tau/\mu} \quad (24)$$

If both T and $L_{x,y}^{refl}$ in the integral term are described by means of a two term cosine series in azimuth angle as in Eq. (20), Eq. (24) then can be rewritten as

$$L_{x,y}^{refl(n+1)}(-\mu, \mu_0, \phi - \phi_0) = [L_{x,y}(-\mu, \mu_0, \phi - \phi_0) - L^{atm}(-\mu, \mu_0, \phi - \phi_0)] \cdot e^{\tau/\mu} - 2\pi \cdot e^{\tau/\mu} \int_0^1 T_0(-\mu, -\mu') L_{0,x,y}^{refl(n)}(-\mu', \mu_0) d\mu' - \pi \cos(\phi - \phi_0) \cdot e^{\tau/\mu} \int_0^1 T_1(-\mu, -\mu') L_{1,x,y}^{refl(n)}(-\mu', \mu_0) d\mu' \quad (25)$$

where $L_{0,x,y}^{refl(n)}$ and $L_{1,x,y}^{refl(n)}$ are computed using $L_{x,y}^{refl(n)}$ in Eqs. (21) and (22) and T_0 and T_1 are described by

$$T_0(-\mu, -\mu') = \frac{1}{2\pi} \int_0^{2\pi} T(-\mu, -\mu', \phi - \phi') d\phi' \quad (26)$$

and

$$T_1(-\mu, -\mu') = \frac{1}{\pi} \int_0^{2\pi} T(-\mu, -\mu', \phi - \phi') \cos(\phi' - \phi) d\phi' \quad (27)$$

respectively. Once $L_{x,y}^{refl}$ is updated it is then used to compute a new $M_{x,y}$ from Eq. (23) and a new $A_{x,y}^{hem}$ from Eq. (16). The iteration number N is a configurable parameter, currently set equal to 2.

$$\text{Equation deleted} \quad (28)$$

The procedure described by Eq. (25) is very fast and very stable. Once $L_{x,y}^{refl}$ and $A_{x,y}^{hem}$ are retrieved, the hemispherical-directional reflectance factor $r_{x,y}$ then can be evaluated from the expression

$$\begin{aligned}
r_{x,y}(-\mu, \mu_0, \phi - \phi_0) &= \frac{\pi \cdot L_{x,y}^{refl}(-\mu, \mu_0, \phi - \phi_0)}{E_{x,y}(\mu_0)} \\
&= \frac{\pi \cdot L_{x,y}^{refl}(-\mu, \mu_0, \phi - \phi_0) \cdot [1 - A_{x,y}^{hem}(\mu_0) \cdot s]}{E_b(\mu_0)}
\end{aligned} \tag{29}$$

where Eqs.(8), (9), (12) and (14) are used.

3.3.3.3 Algorithm synopsis and computational specifics

In this section the algorithm described above is recast in terms of the parameters used to describe the MISR TOA radiances and the parameters contained in the SMART Dataset. All TOA radiances, both the MISR measurements and the computed radiances in the SMART Dataset, are expressed as equivalent reflectances ρ , defined as

$$\rho(-\mu, \mu', \phi - \phi') \equiv \pi L(-\mu, \mu', \phi - \phi') / E_0 \tag{30}$$

where E_0 is the exo-atmospheric solar irradiance. Also, any irradiance E or radiant exitance M is expressed as a normalized irradiance e or normalized radiant exitance m , with the normalization factor being E_0 . Thus, we define

$$\begin{aligned}
e(\mu_0) &\equiv E(\mu_0) / E_0 \\
m(\mu_0) &\equiv M(\mu_0) / E_0
\end{aligned} \tag{31}$$

The basic iteration equation for the algorithm, Eq. (25) then is rewritten as

$$\begin{aligned}
\rho_{x,y}^{refl(n+1)}(-\mu, \mu_0, \phi - \phi_0) &= [\rho_{x,y}(-\mu, \mu_0, \phi - \phi_0) - \rho^{atm}(-\mu, \mu_0, \phi - \phi_0)] \cdot e^{\tau/\mu} \\
&\quad - 2\pi \cdot e^{\tau/\mu} \int_0^1 T_0(-\mu, -\mu') \rho_{0,x,y}^{refl(n)}(-\mu', \mu_0) d\mu' \\
&\quad - \pi \cos(\phi - \phi_0) \cdot e^{\tau/\mu} \int_0^1 T_1(-\mu, -\mu') \rho_{1,x,y}^{refl(n)}(-\mu', \mu_0) d\mu'
\end{aligned} \tag{32}$$

with $\rho_{0,x,y}^{refl(n)}$ and $\rho_{1,x,y}^{refl(n)}$ derived from Eqs. (21) and (22),

$$\rho_{0,x,y}^{refl(n)}(-\mu, \mu_0) = \frac{\rho_{x,y}^{refl(n)}(-\mu, \mu_0, \phi_a - \phi_0) \cos(\phi_f - \phi_0) - \rho_{x,y}^{refl(n)}(-\mu, \mu_0, \phi_f - \phi_0) \cos(\phi_a - \phi_0)}{\cos(\phi_f - \phi_0) - \cos(\phi_a - \phi_0)} \quad (33)$$

$$\rho_{1,x,y}^{refl(n)}(-\mu, \mu_0) = \frac{\rho_{x,y}^{refl(n)}(-\mu, \mu_0, \phi_f - \phi_0) - \rho_{x,y}^{refl(n)}(-\mu, \mu_0, \phi_a - \phi_0)}{\cos(\phi_f - \phi_0) - \cos(\phi_a - \phi_0)} \quad (34)$$

The equivalent reflectances $\rho_{x,y}^{refl(n)}$ for a camera pair in Eqs. (33) and (34) are assumed to have identical view zenith angle cosines, μ . In practice, a camera pair, with view geometries $(-\mu_f, \mu_0, \phi_f - \phi_0)$ and $(-\mu_a, \mu_0, \phi_a - \phi_0)$, will not have identical viewing angles, i.e., μ_f in the forward direction will not equal μ_a in the aftward direction, due to the ellipsoidal shape of the Earth's surface, altitude variations of the orbit, and boresight differences incurred during instrument fabrication. This view zenith angle difference, however, is generally small (less than 1.5° for the D cameras, which are the cameras most affected) so a pair-averaged value of μ is used. But there will be times when one or more cameras is not available for a particular subregion simply due to cloud contamination. This situation then requires that $\rho_{x,y}^{refl(n)}$ be interpolated at the missing camera view angle cosine, thus completing the equivalent reflectance pair to be used in Eqs. (33) and (34). If μ_m is the view angle cosine for a camera labeled m in, say, the aftward bank and with an unusable measurement, the interpolated reflectance, $\tilde{\rho}_{x,y}^{refl}$, of camera m can be expressed as

$$\begin{aligned} &\tilde{\rho}_{x,y}^{refl(n)}(-\mu_m, \mu_0, \phi_{m,a} - \phi_0) \\ &= (1 - \delta) \cdot \rho_{x,y}^{refl(n)}(-\mu_{m+1,a}, \mu_0, \phi_{m+1,a} - \phi_0) + \delta \cdot \rho_{x,y}^{refl(n)}(-\mu_{m-1,a}, \mu_0, \phi_{m-1,a} - \phi_0) \end{aligned} \quad (35)$$

where $(-\mu_m, \mu_0, \phi_{m,a} - \phi_0)$ is the view geometry for the interpolated reflectance of camera m in the aftward bank; $(-\mu_{m+1,a}, \mu_0, \phi_{m+1,a} - \phi_0)$ and $(-\mu_{m-1,a}, \mu_0, \phi_{m-1,a} - \phi_0)$ are the view geometries for the valid reflectances of nearest neighbor cameras $m+1$ and $m-1$, respectively, on either side of camera m . Here,

$$\begin{aligned} &\mu_{m+1,a} \leq \mu_m \leq \mu_{m-1,a} \\ &\delta = \frac{\mu_m - \mu_{m+1,a}}{\mu_{m-1,a} - \mu_{m+1,a}} \end{aligned} \quad (36)$$

Thus, the surface equivalent reflectance is linearly interpolated, with δ as the variable. If μ_m is outside of the range of cosines for the available cameras in a particular bank, then $\tilde{\rho}_{x,y}^{refl(n)}$ for μ_m is set equal to $\rho_{x,y}^{refl(n)}$ of the nearest available camera. This procedure for obtaining interpolated values $\tilde{\rho}_{x,y}^{refl(n)}$ can be used even if only one camera is available. In this case all values of $\tilde{\rho}_{x,y}^{refl(n)}$

are set equal to the one available value of $\rho_{x,y}^{refl(n)}$. Clearly the surface retrieval quality is reduced when less than the full complement of nine cameras is available and this fact is recorded by the Retrieval Quality Indicator which notes the number of cameras used. Therefore, regardless of the number of usable cameras, a complete set of nine values of $\rho_{x,y}^{refl(n)}$ is always made available for use in Eqs. (33) and (34) to obtain the five values each of $\rho_{0,x,y}^{refl(n)}$ and $\rho_{1,x,y}^{refl(n)}$.

The initial estimate, $\rho_{x,y}^{refl(0)}$, derived from Eq. (18),

$$\rho_{x,y}^{refl(0)}(-\mu, \mu_0, \phi - \phi_0) = \frac{\rho_{x,y}(-\mu, \mu_0, \phi - \phi_0) - \rho^{atm}(-\mu, \mu_0, \phi - \phi_0)}{e^{-\tau/\mu} + t(-\mu)} \quad (37)$$

requires that ρ^{atm} and t be interpolated to the camera specific values of μ since these parameters are stored in the SMART Dataset on a grid of view angle cosines which are selected to be Radau quadrature points and are referred to as the standard Radau point grid. This is accomplished using a three point quadratic interpolation scheme.

The bihemispherical reflectance for the n^{th} iteration, $A_{x,y}^{hem(n)}$, described by Eq. (16), is rewritten as

$$A_{x,y}^{hem(n)}(\mu_0) = \frac{m_{x,y}^{(n)}(\mu_0)}{e_b(\mu_0) + s \cdot m_{x,y}^{(n)}(\mu_0)} \quad (38)$$

and $m_{x,y}^{(n)}$ is derived from Eq. (23),

$$m_{x,y}^{(n)}(\mu_0) = 2 \int_0^1 \rho_{0,x,y}^{refl(n)}(-\mu, \mu_0) \mu d\mu \quad (39)$$

where the integration is performed using a Radau quadrature formula. This integration scheme requires that $\rho_{0,x,y}^{refl(n)}$ itself be interpolated at the selected Radau quadrature points which are taken to be the standard Radau point grid. Again, linear interpolation is used for those Radau points within the range covered by the five camera pair-averaged μ values. For those points outside this range, the interpolated values of $\rho_{0,x,y}^{refl(n)}$ are set equal to the $\rho_{0,x,y}^{refl(n)}$ value at the μ range limit. The camera pair-averaged values of $\rho_{1,x,y}^{refl(n)}$ are also interpolated on the standard Radau point grid in the same way as $\rho_{0,x,y}^{refl(n)}$ because both interpolated functions are needed in the integral terms of Eq. (32). These integrals have $\rho_{0,x,y}^{refl(n)}$ and $\rho_{1,x,y}^{refl(n)}$ multiplying T_0 and T_1 , respectively and, like the expression for $m_{x,y}^{(n)}$ in Eq. (39), also are evaluated using a Radau quadrature formula. Since T_0 and T_1 are computed on the standard Radau point grid for both the incoming and outgoing directions, the integral terms can be computed for the complete range of view angle cosines equal

to the standard Radau points but this is not necessary. Only those Radau view angle points need to be considered which are used in a three-point quadratic interpolation to evaluate these terms at the particular camera zenith angles.

From Eq. (29) the hemispherical-directional reflectance factor, $r_{x,y}^{(N)}$, for the N^{th} and final iteration is rewritten as

$$r_{x,y}^{(N)}(-\mu, \mu_0, \phi - \phi_0) = \frac{\rho_{x,y}^{refl(N)}(-\mu, \mu_0, \phi - \phi_0) \cdot [1 - A_{x,y}^{hem(N)}(\mu_0) \cdot s]}{e_b(\mu_0)} \quad (40)$$

where the black surface diffuse irradiance, e_b , as expressed in Eq. (10), is given by

$$\begin{aligned} e_b(\mu_0) &= e_b^{dir}(\mu_0) + e_b^{diff}(\mu_0) \\ &= \mu_0 e^{-\tau/\mu_0} + e_b^{diff}(\mu_0) \end{aligned} \quad (41)$$

Note that e_b^{diff} in Eq. (41) must be interpolated at the appropriate solar zenith angle cosine, μ_0 , since it too is stored in the SMART Dataset on the standard Radau point grid.

3.3.3.4 Aerosol mixture requirements of the algorithm

The aerosol model results contained in the SMART Dataset are calculated for pure particles, i.e., each model is composed of a single size distribution, composition and shape prescription. However, the aerosol retrieval process generates best-fitting aerosol mixtures, containing up to three pure particle types or components. Thus, in order to implement the surface retrieval algorithm described above, it is necessary to derive the required atmospheric parameters for the retrieved aerosol mixture, using the SMART Dataset, the Aerosol Climatology Product (ACP), and the archived aerosol retrieval parameters. The HDRF/BHR algorithm uses six atmospheric parameters which are dependent on the particular components of the aerosol mixture. They are optical depth τ , the equivalent reflectance corresponding to the atmospheric path radiance ρ^{atm} , the upward diffuse transmittance T , the angle-integrated upward diffuse transmittance t , the BOA bihemispherical albedo for isotropic incident radiation s , and the normalized black surface diffuse irradiance e_b^{diff} . Their computation is described as follows.

The fractional amount of pure aerosol component n at each wavelength, $f_{n\lambda}$, is defined as the ratio of the component optical depth, $\tau_{n\lambda}$, to the mixture (or total) optical depth, τ_λ . The values of $f_{n\lambda}$ are obtained from the ACP, along with spectral scaling factors that enable scaling the total optical depth in the reference wavelength (chosen to be band 2) to any of the other three MISR bands.

In [M-5] the atmospheric path equivalent reflectance of the mixture, ρ^{atm} , for optical depth

τ_λ was described in terms of the $f_{n\lambda}$ as

$$\begin{aligned} \rho^{atm}(-\mu, \mu_0, \phi - \phi_0; \tau_\lambda) &= \rho_{R,ms}^{black}(-\mu, \mu_0, \phi - \phi_0; \tau_{R,\lambda}) + \sum_n f_{n\lambda} \cdot \rho_{n,ss}^{black}(-\mu, \mu_0, \phi - \phi_0; \tau_\lambda) \\ &+ \sum_n f_{n\lambda} \cdot \frac{\varpi_{mix,\lambda}}{\varpi_{n\lambda}} \cdot e^{-\tau_\lambda |\varpi_{mix,\lambda} - \varpi_{n\lambda}|} \cdot [\rho_{n,ms}^{black}(-\mu, \mu_0, \phi - \phi_0; \tau_\lambda) - \rho_{R,ms}^{black}(-\mu, \mu_0, \phi - \phi_0; \tau_{R,\lambda})] \end{aligned} \quad (42)$$

where $\rho_{n,ss}^{black}$ is the single scattered TOA equivalent reflectance for a black surface which includes contributions from both Rayleigh at optical depth $\tau_{R,\lambda}$ and aerosol component n at the mixture optical depth τ_λ , $\rho_{n,ms}^{black}$ is the multiple scattered TOA equivalent reflectance under the same conditions as single scattering, $\rho_{R,ms}^{black}$ is the pure Rayleigh multiple scattered TOA equivalent reflectance for a black surface at optical depth $\tau_{R,\lambda}$, $\varpi_{n\lambda}$ is the single scattering albedo of aerosol component n , and $\varpi_{mix,\lambda}$ is the single scattering albedo of the mixture.

Equation (42) is an extension of standard linear mixing theory (e.g., [46]), which enables an accurate calculation of the atmospheric path equivalent reflectance for a mixture of pure aerosol particles, given the black surface TOA equivalent reflectances for each of the pure particles and their fractional amounts, without having to perform the exact radiative transfer calculation for the mixture. Standard linear mixing theory is generally accurate when the particles are conservative scatterers, but starts to break down when one or more of the aerosol components is absorbing. The mixing theory described by Eq. (42), however, provides a relatively accurate representation of the mixture equivalent reflectance for both non-absorbing and absorbing particles, though it involves a somewhat more complicated expression, requiring the separation of single and multiple scattering contributions for both Rayleigh and the individual aerosol components.

This description of the atmospheric path equivalent reflectance for the mixture can be expanded to include other parameters which are governed solely by scattering of radiation. These include T , t , s , and e_b^{diff} which, by analogy with Eq. (42), can then be expressed as

$$\begin{aligned} T(-\mu, -\mu', \phi - \phi'; \tau_\lambda) &= T_{R,ms}(-\mu, -\mu', \phi - \phi'; \tau_{R,\lambda}) + \sum_n f_{n\lambda} \cdot T_{n,ss}(-\mu, -\mu', \phi - \phi'; \tau_\lambda) \\ &+ \sum_n f_{n\lambda} \cdot \frac{\varpi_{mix,\lambda}}{\varpi_{n\lambda}} \cdot e^{-\tau_\lambda |\varpi_{mix,\lambda} - \varpi_{n\lambda}|} \cdot [T_{n,ms}(-\mu, -\mu', \phi - \phi'; \tau_\lambda) - T_{R,ms}(-\mu, -\mu', \phi - \phi'; \tau_{R,\lambda})] \end{aligned} \quad (43)$$

$$\begin{aligned} t(-\mu; \tau_\lambda) &= t_{R,ms}(-\mu; \tau_{R,\lambda}) + \sum_n f_{n\lambda} \cdot t_{n,ss}(-\mu; \tau_\lambda) \\ &+ \sum_n f_{n\lambda} \cdot \frac{\varpi_{mix,\lambda}}{\varpi_{n\lambda}} \cdot e^{-\tau_\lambda |\varpi_{mix,\lambda} - \varpi_{n\lambda}|} \cdot [t_{n,ms}(-\mu; \tau_\lambda) - t_{R,ms}(-\mu; \tau_{R,\lambda})] \end{aligned} \quad (44)$$

$$\begin{aligned}
s(\tau_\lambda) &= s_{R,ms}(\tau_{R,\lambda}) \\
&+ \sum_n f_{n\lambda} \cdot s_{n,ss}(\tau_\lambda) + \sum_n f_{n\lambda} \cdot \frac{\varpi_{mix,\lambda}}{\varpi_{n\lambda}} \cdot e^{-\tau_\lambda |\varpi_{mix,\lambda} - \varpi_{n\lambda}|} \cdot [s_{n,ms}(\tau_\lambda) - s_{R,ms}(\tau_{R,\lambda})]
\end{aligned} \tag{45}$$

and

$$\begin{aligned}
e_b^{diff}(\mu_0; \tau_\lambda) &= e_{b,R,ms}^{diff}(\mu_0; \tau_{R,\lambda}) + \sum_n f_{n\lambda} \cdot e_{b,n,ss}^{diff}(\mu_0; \tau_\lambda) \\
&+ \sum_n f_{n\lambda} \cdot \frac{\varpi_{mix,\lambda}}{\varpi_{n\lambda}} \cdot e^{-\tau_\lambda |\varpi_{mix,\lambda} - \varpi_{n\lambda}|} \cdot [e_{b,n,ms}^{diff}(\mu_0; \tau_\lambda) - e_{b,R,ms}^{diff}(\mu_0; \tau_{R,\lambda})]
\end{aligned} \tag{46}$$

To summarize, the aerosol optical depth in the reference band (band 2), τ_r , and the compositional model (mixture) identifier are retrieved aerosol parameters archived in the Aerosol/Surface Product. The fractional amounts $f_{n\lambda}$ associated with the model identifier, the optical depth spectral scale factors, $\varpi_{mix,\lambda}$ and the single scattering albedos $\varpi_{n\lambda}$ for each pure particle type at each MISR wavelength are obtained from the ACP. The remaining atmospheric parameters are contained in the SMART Dataset, indexed by the model identifier. These SMART Dataset parameters are determined on specified grids of aerosol optical depth and view and Sun angular geometry and therefore must be interpolated to the required τ_λ and $(-\mu, \mu_0, \phi - \phi_0)$.

3.3.3.5 Best estimate of the HDRF and BHR and their uncertainties

During the course of the aerosol retrieval a variety of aerosol compositional models or mixtures are tested and those that satisfy the goodness-of-fit criteria, based on consistency with the observations, are acceptable retrieval candidates. If there are N_{cand} such models, the subsequent surface retrieval will use atmospheric parameters which are an average of the atmospheric parameters for the N_{cand} models. Thus,

$$\begin{aligned}
\tau_\lambda &= \frac{1}{N_{cand}} \cdot \sum_{m=1}^{N_{cand}} \tau_{\lambda, m} \\
\rho_\lambda^{atm}(-\mu, \mu_0, \phi - \phi_0) &= \frac{1}{N_{cand}} \cdot \sum_{m=1}^{N_{cand}} \rho_\lambda^{atm}(-\mu, \mu_0, \phi - \phi_0; \tau_{\lambda, m}) \\
T_\lambda(-\mu, -\mu', \phi - \phi') &= \frac{1}{N_{cand}} \cdot \sum_{m=1}^{N_{cand}} T_\lambda(-\mu, -\mu', \phi - \phi'; \tau_{\lambda, m}) \\
t_\lambda(-\mu) &= \frac{1}{N_{cand}} \cdot \sum_{m=1}^{N_{cand}} t_\lambda(-\mu; \tau_{\lambda, m}) \\
s_\lambda &= \frac{1}{N_{cand}} \cdot \sum_{m=1}^{N_{cand}} s_\lambda(\tau_{\lambda, m}) \\
e_{b, \lambda}^{diff}(\mu_0) &= \frac{1}{N_{cand}} \cdot \sum_{m=1}^{N_{cand}} e_b^{diff}(\mu_0; \tau_{\lambda, m})
\end{aligned} \tag{47}$$

where m is the aerosol candidate index. Then the use of these averaged atmospheric parameters in the HDRF/BHR algorithm produces the “best” estimate of the HDRF, $r_{best, \lambda}$, and the BHR, $A_{best, \lambda}^{hem}$. We use the adjective “best” to signify the most unbiased estimate based on our aerosol retrieval results, since we do not invoke any additional information to select any one successful aerosol model over another. Implicit in these estimates and also in the uncertainty analysis described below is the assumption that the various aerosol model candidates are reasonably independent and, therefore, their intrinsic radiative parameters are basically uncorrelated. All aerosol models in the Aerosol Mixture file of the ACP were studied to check for redundancy.

The associated uncertainties in these retrieved surface parameters are a function of both the radiometric uncertainty of the observations and the model uncertainty of the aerosol retrieval. We can derive an expression for the HDRF uncertainty by starting with an appropriate description of the HDRF, r_λ . Assuming an approximate relationship between r_λ and the TOA equivalent reflectances, ρ_λ , based on Eqs. (37), (40), and (41), we can write

$$\begin{aligned}
r_\lambda(-\mu, \mu_0, \phi - \phi_0) &\approx \frac{[1 - A_{best, \lambda}^{hem}(\mu_0) \cdot s_\lambda] \cdot [\rho_\lambda(-\mu, \mu_0, \phi - \phi_0) - \rho_\lambda^{atm}(-\mu, \mu_0, \phi - \phi_0)]}{[\mu_0 e^{-\tau_\lambda/\mu_0} + e_{b, \lambda}^{diff}(\mu_0)] \cdot [e^{-\tau_\lambda/\mu} + t_\lambda(-\mu)]} \\
&= q_\lambda(-\mu, \mu_0) \cdot \rho_\lambda(-\mu, \mu_0, \phi - \phi_0) - u_\lambda(-\mu, \mu_0, \phi - \phi_0)
\end{aligned} \tag{48}$$

with

$$q_\lambda(-\mu, \mu_0) = \frac{[1 - A_{best, \lambda}^{hem}(\mu_0) \cdot s_\lambda]}{[\mu_0 e^{-\tau_\lambda/\mu_0} + e_{b, \lambda}^{diff}(\mu_0)] \cdot [e^{-\tau_\lambda/\mu} + t_\lambda(-\mu)]}$$

$$u_\lambda(-\mu, \mu_0, \phi - \phi_0) = q_\lambda(-\mu, \mu_0) \cdot \rho_\lambda^{aim}(-\mu, \mu_0, \phi - \phi_0) \quad (49)$$

Thus, r_λ is composed of two terms, the first one dependent on both the observations (i.e., ρ_λ) and the aerosol modeling (through q_λ) and the second term, u_λ , dependent only on the modeling.

From the theory of propagation of errors (e.g., [4]) applied to Eq. (48), the variance (the square of the uncertainty) of the HDRF for each camera view, $(\Delta r_\lambda)^2$, can be expressed as

$$\begin{aligned} (\Delta r_\lambda)^2(-\mu, \mu_0, \phi - \phi_0) &= q_\lambda^2(-\mu, \mu_0) \cdot \sigma_{\rho_\lambda}^2(-\mu, \mu_0, \phi - \phi_0) \\ &\quad + \rho_\lambda^2(-\mu, \mu_0, \phi - \phi_0) \cdot \sigma_{q_\lambda}^2(-\mu, \mu_0) + \sigma_{u_\lambda}^2(-\mu, \mu_0, \phi - \phi_0) \\ &\quad - 2 \cdot \rho_\lambda(-\mu, \mu_0, \phi - \phi_0) \cdot \sigma_{qu_\lambda}^2(-\mu, \mu_0, \phi - \phi_0) \end{aligned} \quad (50)$$

where $\sigma_{q_\lambda}^2$, $\sigma_{\rho_\lambda}^2$, and $\sigma_{u_\lambda}^2$ are variances of q_λ , ρ_λ , and u_λ , respectively, and $\sigma_{qu_\lambda}^2$ is the covariance of q_λ and u_λ . Since variations in ρ_λ are uncorrelated with variations in q_λ or u_λ , their resulting covariance terms are set to zero. But it is expected that variations in q_λ will be correlated somewhat with variations in u_λ since both parameters are generated from the aerosol modelling, so its covariance term is retained. Estimates of these variances and the covariance can be written as,

$$\begin{aligned} \sigma_{\rho_\lambda}^2(-\mu, \mu_0, \phi - \phi_0) &= \sigma_{abs, \lambda}^2(-\mu, \mu_0, \phi - \phi_0) \\ \sigma_{q_\lambda}^2(-\mu, \mu_0) &= \frac{1}{N_{cand}} \cdot \sum_{m=1}^{N_{cand}} [q(-\mu, \mu_0; \tau_{\lambda, m}) - q_\lambda(-\mu, \mu_0)]^2 \\ \sigma_{u_\lambda}^2(-\mu, \mu_0, \phi - \phi_0) &= \frac{1}{N_{cand}} \cdot \sum_{m=1}^{N_{cand}} [u(-\mu, \mu_0, \phi - \phi_0; \tau_{\lambda, m}) - u_\lambda(-\mu, \mu_0, \phi - \phi_0)]^2 \\ \sigma_{qu_\lambda}^2(-\mu, \mu_0, \phi - \phi_0) &= \\ &\quad \frac{1}{N_{cand}} \cdot \sum_{m=1}^{N_{cand}} [u(-\mu, \mu_0, \phi - \phi_0; \tau_{\lambda, m}) - u_\lambda(-\mu, \mu_0, \phi - \phi_0)] \cdot [q(-\mu, \mu_0; \tau_{\lambda, m}) - q_\lambda(-\mu, \mu_0)] \end{aligned} \quad (51)$$

where q and u are described by the model-dependent forms of Eq. (49), namely,

$$q(-\mu, \mu_0; \tau_{\lambda, m}) = \frac{[1 - A_{best, \lambda}^{hem}(\mu_0) \cdot s(\tau_{\lambda, m})]}{[\mu_0 e^{-\tau_{\lambda, m}/\mu_0} + e_b^{diff}(\mu_0; \tau_{\lambda, m})] \cdot [e^{-\tau_{\lambda, m}/\mu} + t(-\mu; \tau_{\lambda, m})]}$$

$$u(-\mu, \mu_0, \phi - \phi_0; \tau_{\lambda, m}) = q(-\mu, \mu_0; \tau_{\lambda, m}) \cdot \rho^{atm}(-\mu, \mu_0, \phi - \phi_0; \tau_{\lambda, m}) \quad (52)$$

The value of $\sigma_{abs, \lambda}$, the absolute radiometric uncertainty in ρ_{λ} , is obtained by using calibration uncertainty information provided in the MISR Ancillary Radiometric Product (see [M-2]). These data are provided at a standard set of equivalent reflectances (nominally 15 values), for each channel (band and camera combination) of the instrument. Specifically, we make use of:

- (1) ϵ_{abs_sys} , the systematic component of the absolute radiometric uncertainty, expressed in percent, at the tabulated set of equivalent reflectance levels and in the appropriate channel;
- (2) SNR_{am} , the signal-to-noise ratio at the tabulated set of equivalent reflectance levels and in the appropriate channel, for the averaging mode $am = 4 \times 4$.

Now, to calculate $\sigma_{abs, \lambda}$ corresponding to equivalent reflectance ρ_{λ} , we first linearly interpolate the tabulated values of ϵ_{abs_sys} and $SNR_{4 \times 4}$ to this equivalent reflectance. Denoting these interpolated values $\epsilon_{abs_sys}(\rho_{\lambda})$ and $SNR_{4 \times 4}(\rho_{\lambda})$, we then have

$$\sigma_{abs}^2 = \rho_{\lambda}^2 \left\{ \left(\frac{\epsilon_{abs_sys}(\rho_{\lambda})}{100} \right)^2 + \left(\frac{1}{SNR_{4 \times 4}(\rho_{\lambda})} \right)^2 \right\} \quad (52a)$$

The camera-averaged uncertainty of the HDRF, $\overline{\Delta r_{\lambda}}$ is then given by

$$\overline{\Delta r_{\lambda}}(\mu_0, \phi_0) = \sqrt{\frac{1}{N_{cam}} \cdot \sum_i (\Delta r_{\lambda})^2(-\mu_i, \mu_0, \phi_i - \phi_0)} \quad (53)$$

with N_{cam} as the number of available cameras.

The uncertainty in the BHR, ΔA_{λ}^{hem} , is obtained in a similar manner. Starting from Eqs. (11), (13), (14) and (41) and using the normalized form of the radiant exitance and irradiance, we can write

$$\begin{aligned}
A_{\lambda}^{hem}(\mu_0) &= \frac{m_{\lambda}(\mu_0)}{e_{\lambda}(\mu_0)} \\
m_{\lambda}(\mu_0) &= \int_0^1 \int_0^{2\pi} \rho_{\lambda}^{refl}(-\mu, \mu_0, \phi - \phi_0) \mu d\mu d\phi \\
e_{\lambda}(\mu_0) &= \frac{e_b(\mu_0)}{1 - A_{\lambda}^{hem}(\mu_0) \cdot s_{\lambda}} = \frac{\mu_0 e^{-\tau_{\lambda}/\mu_0} + e_{b,\lambda}^{diff}(\mu_0)}{1 - A_{best,\lambda}^{hem}(\mu_0) \cdot s_{\lambda}}
\end{aligned} \tag{54}$$

The expression for m_{λ} can be approximated by

$$\begin{aligned}
m_{\lambda}(\mu_0) &\approx \overline{\rho_{\lambda}^{refl}} \cdot \int_0^1 \int_0^{2\pi} \mu d\mu d\phi \\
&= \pi \cdot \overline{\rho_{\lambda}^{refl}} = \frac{\pi}{N_{cam}} \cdot \sum_i \rho_{\lambda}^{refl}(-\mu_i, \mu_0, \phi_i - \phi_0)
\end{aligned} \tag{55}$$

where $\overline{\rho_{\lambda}^{refl}}$ is the camera-averaged equivalent reflectance at the surface. Using Eq. (37) as an approximate form for ρ_{λ}^{refl} in Eq. (55), we have

$$\begin{aligned}
m_{\lambda}(\mu_0) &\approx \frac{\pi}{N_{cam}} \cdot \sum_i \frac{\rho_{\lambda}(-\mu_i, \mu_0, \phi_i - \phi_0) - \rho_{\lambda}^{atm}(-\mu_i, \mu_0, \phi_i - \phi_0)}{e^{-\tau_{\lambda}/\mu_i} + t_{\lambda}(-\mu_i)} \\
&= \frac{\pi}{N_{cam}} \cdot \sum_i g_{\lambda}(-\mu_i) \cdot \rho_{\lambda}(-\mu_i, \mu_0, \phi_i - \phi_0) - v_{\lambda}(\mu_0, \phi_0)
\end{aligned} \tag{56}$$

with

$$\begin{aligned}
g_{\lambda}(-\mu) &= [e^{-\tau_{\lambda}/\mu} + t_{\lambda}(-\mu)]^{-1} \\
v_{\lambda}(\mu_0, \phi_0) &= \frac{\pi}{N_{cam}} \cdot \sum_i g_{\lambda}(-\mu_i) \cdot \rho_{\lambda}^{atm}(-\mu_i, \mu_0, \phi_i - \phi_0)
\end{aligned} \tag{57}$$

The radiant exitance m_{λ} is now described in terms of the individual camera-dependent TOA equivalent reflectances, ρ_{λ} , and v_{λ} , a term dependent only on the aerosol models. The variance of the BHR then can be expressed as

$$\begin{aligned}
(\Delta A_{\lambda}^{hem})^2(\mu_0) &= \frac{\pi^2}{e_{\lambda}^2(\mu_0) \cdot N_{cam}^2} \cdot \sum_i g_{\lambda}^2(-\mu_i) \cdot \sigma_{\rho_{\lambda}}^2(-\mu_i, \mu_0, \phi_i - \phi_0) \\
&\quad + \frac{1}{e_{\lambda}^2(\mu_0)} \cdot \sigma_{v_{\lambda}}^2(\mu_0, \phi_0) + \left[\frac{A_{best, \lambda}^{hem}(\mu_0)}{e_{\lambda}(\mu_0)} \right]^2 \cdot \sigma_{e_{\lambda}}^2(\mu_0) \\
&\quad + 2 \cdot \frac{A_{best, \lambda}^{hem}(\mu_0)}{e_{\lambda}^2(\mu_0)} \cdot \sigma_{ev_{\lambda}}^2(\mu_0, \phi_0)
\end{aligned} \tag{58}$$

where $\sigma_{\rho_{\lambda}}^2$ are the variances of the ρ_{λ} of the individual cameras, $\sigma_{v_{\lambda}}^2$ and $\sigma_{e_{\lambda}}^2$ are variances of v_{λ} and e_{λ} , respectively, and $\sigma_{ev_{\lambda}}^2$ is the covariance. Estimates of the variances $\sigma_{\rho_{\lambda}}^2$ are given in Eq. (51). Estimates for the remaining variances and the covariance in Eq. (58) are given by

$$\begin{aligned}
\sigma_{v_{\lambda}}^2(\mu_0, \phi_0) &= \frac{1}{N_{cand}} \cdot \sum_{m=1}^{N_{cand}} [v(\mu_0, \phi_0; \tau_{\lambda, m}) - v_{\lambda}(\mu_0, \phi_0)]^2 \\
\sigma_{e_{\lambda}}^2(\mu_0) &= \frac{1}{N_{cand}} \cdot \sum_{m=1}^{N_{cand}} [e(\mu_0; \tau_{\lambda, m}) - e_{\lambda}(\mu_0)]^2 \\
\sigma_{ev_{\lambda}}^2(\mu_0, \phi_0) &= \frac{1}{N_{cand}} \cdot \sum_{m=1}^{N_{cand}} [v(\mu_0, \phi_0; \tau_{\lambda, m}) - v_{\lambda}(\mu_0, \phi_0)] \cdot [e(\mu_0; \tau_{\lambda, m}) - e_{\lambda}(\mu_0)]
\end{aligned} \tag{59}$$

with e and v described by the model-dependent forms of Eqs. (54) and (57), i.e.,

$$\begin{aligned}
e(\mu_0; \tau_{\lambda, m}) &= \frac{\mu_0 e^{-\tau_{\lambda, m}/\mu_0} + e_b^{diff}(\mu_0; \tau_{\lambda, m})}{1 - A_{best, \lambda}^{hem}(\mu_0) \cdot s(\tau_{\lambda, m})} \\
v(\mu_0, \phi_0; \tau_{\lambda, m}) &= \frac{\pi}{N_{cam}} \cdot \sum_i g(-\mu_i; \tau_{\lambda, m}) \cdot \rho^{atm}(-\mu_i, \mu_0, \phi_i - \phi_0; \tau_{\lambda, m}) \\
g(-\mu; \tau_{\lambda, m}) &= [e^{-\tau_{\lambda, m}/\mu} + t(-\mu; \tau_{\lambda, m})]^{-1}
\end{aligned} \tag{60}$$

where m is the model index.

3.3.3.6 Best estimates of the ancillary atmospheric data and their uncertainties

The ancillary atmospheric data consists of the best estimates of the black surface irradiance,

$e_{b,\lambda}$ and the BOA bihemispherical albedo for isotropic incident radiation, s_λ . With these parameters and the best estimate of the BHR, $A_{best,\lambda}^{hem}$, a determination of the ambient surface irradiance and radiance exitance can be made for each subregion using Eqs. (13) and (14). The best estimate of the BOA hemispherical albedo, s_λ , is the model-averaged one given in Eq. (47), and the best estimate of the total irradiance, $e_{b,\lambda}$, can be expressed as

$$e_{b,\lambda}(\mu_0) = \mu_0 e^{-\tau_\lambda/\mu_0} + e_{b,\lambda}^{diff}(\mu_0) \quad (61)$$

where the model-averaged optical depth, τ_λ , and diffuse irradiance, $e_{b,\lambda}^{diff}$, are also given in Eq. (47).

An estimate of the variances (square of the uncertainties) of these parameters follows the form of Eqs. (51) and (59). We have

$$\begin{aligned} (\Delta e_{b,\lambda})^2(\mu_0) &= \frac{1}{N_{cand}} \cdot \sum_{m=1}^{N_{cand}} [e_b(\mu_0; \tau_{\lambda,m}) - e_{b,\lambda}(\mu_0)]^2 \\ (\Delta s_\lambda)^2 &= \frac{1}{N_{cand}} \cdot \sum_{m=1}^{N_{cand}} [s(\tau_{\lambda,m}) - s_\lambda]^2 \end{aligned} \quad (62)$$

with e_b described by the model-dependent form of Eq. (61), namely

$$e_b(\mu_0; \tau_{\lambda,m}) = \mu_0 e^{-\tau_{\lambda,m}/\mu_0} + e_b^{diff}(\mu_0; \tau_{\lambda,m}) \quad (63)$$

3.3.3.7 Archived algorithm output

For those 1.1 km subregions upon which a HDRF/BHR retrieval was performed, the best estimate HDRF, r_{best} , is computed at all available view angles and for all available MISR wavelengths. Its camera-averaged uncertainty, Δr is computed for all available MISR wavelengths. The best estimate BHR, A_{best}^{hem} and its uncertainty, ΔA^{hem} , are computed for all available MISR wavelengths. In the particular case of BHR, the uncertainty measure archived in the data product is relative uncertainty, given by $\Delta A^{hem} / A_{best}^{hem}$. In addition the ancillary atmospheric products, $e_{b,\lambda}$, s_λ and their uncertainties, $\Delta e_{b,\lambda}$ and Δs_λ , respectively, are computed for the 17.6 km region. These parameters are directly archived in the Aerosol/Surface Product. The view directions and the sun direction associated with these parameters are provided in the ellipsoid-referenced coordinate system in the Level 1B2 Georectified Radiance Product, and may also be calculated by the user in the terrain-referenced coordinate system (see §3.3.2).

3.3.4 Retrieve BRF and DHR

3.3.4.1 Physics of the problem

The algorithm for retrieving HDRF's and BHR's from MISR TOA radiances is virtually independent of any particular kind of surface model and is shown to be highly accurate when correct atmospheric information is used (see §3.5). Going a step further, it then is possible to retrieve bidirectional reflectance factors (BRF's) and directional-hemispherical reflectances (DHR's) by fitting the retrieved HDRF's to computed HDRF's, using a parameterized bidirectional reflectance distribution (BRDF) surface model. The BRF is actually a limiting form of the HDRF, defined for the special condition of no atmosphere. The same limiting form also applies to the relationship between the BHR and the DHR. This implies that there is no diffuse radiation incident on the surface and only the direct radiance from the Sun. It is the removal of the effects of the diffuse radiance from the HDRF's which requires the use of a parameterized BRDF surface model in the BRF/DHR algorithm and which ultimately makes the retrieved BRF's and DHR's somewhat model dependent. The BRF/DHR algorithm also determines the BRDF surface model parameters, which allows the model to predict the surface angular reflectance properties fully and thus to extend the geometric range of the BRF's and DHR's (and HDRF's and BHR's) to also include all solar and viewing geometries not covered by the observations. With further research, it may also be possible to obtain a correlation between the model parameters and surface physical parameters (e.g., LAI and leaf orientation parameters) and surface classification types.

A number of BRDF surface models have been proposed in the literature, ranging from those with only 2 - 3 parameters (e.g., [45]) to those with 10 and more parameters (e.g., [1], [38]). Devising new and better BRDF surface models is an ongoing effort by many researchers and there is no consensus at the present time as to an optimum BRDF model for use with multi-angle data. Different researchers may want to use different models, depending on the focus of their investigations. If simple models, containing two or three parameters, are used in the inversion process then the MISR HDRF's associated with individual swaths usually will be a sufficient data set upon which to perform retrievals. However, if the more complicated BRDF surface models are used, containing more than three parameters, then the MISR HDRF's associated with overlapping swaths from multiple orbits and multiple days will be required and possibly the addition of MODIS data with its greater cross-track coverage. For the MISR at-launch standard product, we have opted for the former strategy, and a modified form of the BRDF model of Rahman et al. [37] is used. The BRDF, $f_{x,y}$, is directly proportional to the surface bidirectional reflectance factor, R , according to

$$f_{x,y}(-\mu, \mu_0, \phi - \phi_0) = \frac{1}{\pi} \cdot R_{x,y}(-\mu, \mu_0, \phi - \phi_0) \quad (64)$$

since the BRDF equals $1/\pi$ for a lambertian scattering surface [35]. Aside from the factor of π , the BRF and the BRDF are essentially identical descriptions of the scattering properties of a surface

and the two terms can be used interchangeably. For consistency with usage in the MISR aerosol and surface retrievals, we cast our equations in terms of BRF.

3.3.4.2 Mathematical description of the algorithm

The angular distribution of a parallel beam of radiation, incident on the surface in the direction (μ_0, ϕ_0) can be expressed as

$$L_{x,y}^{inc}(\mu, \mu_0, \phi - \phi_0) = E_0 \cdot \delta(\mu - \mu_0) \cdot \delta(\phi - \phi_0) \quad (65)$$

where δ is the Dirac δ -function. Substituting this expression into Eq. (8), we find

$$\begin{aligned} r_{x,y}(-\mu, \mu_0, \phi - \phi_0) &= \frac{\frac{E_0}{\pi} \int_0^{12\pi} R_{x,y}(-\mu, \mu', \phi - \phi') \delta(\mu' - \mu_0) \delta(\phi' - \phi_0) \mu' d\mu' d\phi'}{\frac{E_0}{\pi} \int_0^{12\pi} \delta(\mu' - \mu_0) \delta(\phi' - \phi_0) \mu' d\mu' d\phi'} \\ &= R_{x,y}(-\mu, \mu_0, \phi - \phi_0) \end{aligned} \quad (66)$$

Thus, for the condition of no atmosphere and the incident solar radiation at the surface is a parallel beam of light, the hemispherical-directional reflectance factor, $r_{x,y}$, is equal to the *bidirectional reflectance factor*, $R_{x,y}$. The *directional-hemispherical reflectance* (DHR), $A_{x,y}^{dir}$, is the hemispherically integrated BRF, defined as in Eq. (13) with $r_{x,y}$ replaced by $R_{x,y}$, i.e.,

$$\begin{aligned} A_{x,y}^{dir}(\mu_0) &= \frac{1}{\pi} \int_0^{12\pi} R_{x,y}(-\mu, \mu_0, \phi - \phi_0) \mu d\mu d\phi \\ &= \frac{M_{x,y}(\mu_0)}{E(\mu_0)} \end{aligned} \quad (67)$$

$M_{x,y}$ is the radiant exitance when the surface is illuminated by a parallel beam of radiation and E is the irradiance of the parallel beam, equal to $\mu_0 E_0$.

The retrieval algorithm starts with the relationship between the HDRF and the BRF, i.e., Eq. (8),

$$r_{x,y}(-\mu, \mu_0, \phi - \phi_0) = \frac{\int_0^1 \int_0^{2\pi} R_{x,y}(-\mu, \mu', \phi - \phi') L_{x,y}^{inc}(\mu', \mu_0, \phi' - \phi_0) \mu' d\mu' d\phi'}{E_{x,y}(\mu_0)} \quad (68)$$

where $r_{x,y}$ has been previously retrieved and the irradiance $E_{x,y}$ is computed using Eq. (14). The incident radiance $L_{x,y}^{inc}$ is approximated by the form,

$$\begin{aligned} L_{x,y}^{inc}(\mu, \mu_0, \phi - \phi_0) &\equiv E_0 e^{-\tau/\mu_0} \cdot \delta(\mu - \mu_0) \cdot \delta(\phi - \phi_0) \\ &+ E_0 \cdot [T_0'(\mu, \mu_0) + T_1'(\mu, \mu_0) \cos(\phi - \phi_0)] \\ &+ \frac{A_{x,y}^{hem}(\mu_0) \cdot s}{\pi} \cdot E_{x,y}(\mu_0) \end{aligned} \quad (69)$$

where the first term on the right-hand-side of Eq. (69) represents the direct radiance, the second term represents approximately the diffuse downwelling radiance in the absence of a surface (i.e., a black surface), and the last term represents approximately the downwelling radiance due to multiple reflections between the atmosphere and the surface. The diffuse downward transmittance T' is described by a two term cosine series in $\phi - \phi_0$, where T_0' and T_1' are determined as in Eqs. (26) and (27) for the upward transmittance. There is a reciprocity relationship between the upward and downward diffuse transmittances, namely,

$$\mu \cdot T(-\mu, -\mu', \phi - \phi') = \mu' \cdot T'(\mu', \mu, \phi' - \phi) \quad (70)$$

which implies,

$$\begin{aligned} \mu \cdot T_0(-\mu, -\mu') &= \mu' \cdot T_0'(\mu', \mu) \\ \mu \cdot T_1(-\mu, -\mu') &= \mu' \cdot T_1'(\mu', \mu) \end{aligned} \quad (71)$$

The relationships expressed in Eq. (71) are important because they require only the T_0 and T_1 functions be stored in the SMART dataset. Substituting Eq. (69) for $L_{x,y}^{inc}$ in Eq. (68) and using the relations described by Eq. (71),

$$\begin{aligned}
r_{x,y}(-\mu, \mu_0, \phi - \phi_0) = & \frac{E_b^{dir}(\mu_0)}{E_{x,y}(\mu_0)} \cdot R_{x,y}(-\mu, \mu_0, \phi - \phi_0) \\
& + \frac{\mu_0 E_0}{E_{x,y}(\mu_0)} \cdot 2\pi \int_0^1 R_{0,x,y}(-\mu, \mu') T_0(-\mu_0, -\mu') d\mu' \\
& + \frac{\mu_0 E_0}{E_{x,y}(\mu_0)} \cdot \pi \cos(\phi - \phi_0) \int_0^1 R_{1,x,y}(-\mu, \mu') T_1(-\mu_0, -\mu') d\mu' \\
& + A_{x,y}^{hem}(\mu_0) \cdot s \cdot 2 \int_0^1 R_{0,x,y}(-\mu, \mu') \mu' d\mu'
\end{aligned} \tag{72}$$

where the direct irradiance E_b^{dir} is given by

$$E_b^{dir}(\mu_0) = \mu_0 E_0 \cdot e^{-\tau/\mu_0} \tag{73}$$

and $R_{x,y}$ within the integrals is expanded in a two term cosine series in $\phi - \phi'$,

$$R_{x,y}(-\mu, \mu', \phi - \phi') = R_{0,x,y}(-\mu, \mu') + R_{1,x,y}(-\mu, \mu') \cdot \cos(\phi - \phi') \tag{74}$$

After some rearranging Eq. (72) is suitable to be used in an iterative scheme to determine $R_{x,y}$. We have,

$$\begin{aligned}
R_{x,y}^{(n+1)}(-\mu, \mu_0, \phi - \phi_0) = & \frac{E_{x,y}(\mu_0)}{E_b^{dir}(\mu_0)} \cdot r_{x,y}(-\mu, \mu_0, \phi - \phi_0) \\
& - \frac{2\pi}{e^{-\tau/\mu_0}} \cdot \int_0^1 R_{0,model}^{(n)}(-\mu, \mu') T_0(-\mu_0, -\mu') d\mu' \\
& - \frac{\pi \cdot \cos(\phi - \phi_0)}{e^{-\tau/\mu_0}} \cdot \int_0^1 R_{1,model}^{(n)}(-\mu, \mu') T_1(-\mu_0, -\mu') d\mu' \\
& - \frac{A_{x,y}^{hem}(\mu_0) \cdot s \cdot E_{x,y}(\mu_0)}{E_b^{dir}(\mu_0)} \cdot 2 \int_0^1 R_{0,model}^{(n)}(-\mu, \mu') \mu' d\mu'
\end{aligned} \tag{75}$$

where $R_{0,x,y}^{(n)}$ and $R_{1,x,y}^{(n)}$ are replaced by $R_{0,model}^{(n)}$ and $R_{1,model}^{(n)}$, respectively, which are produced from a BRF model. This step is necessary because $R_{0,x,y}^{(n)}$ and $R_{1,x,y}^{(n)}$ in the integrals of Eq. (72) are dependent on μ' , the direction of incidence of the radiance at the surface, and this dependence

is displayed in the MISR data only for the single direction, μ_0 , the cosine of the sun angle of the observations. The parameterized BRF model is specified by fitting it to $R_{x,y}^{(n)}$ and determining the best fit parameters. Once the parameters are determined, this procedure then allows $R_{0,model}^{(n)}$ and $R_{1,model}^{(n)}$ to be computed from the expressions

$$R_{0,model}^{(n)}(-\mu, \mu') = \frac{1}{2\pi} \int_0^{2\pi} R_{model}^{(n)}(-\mu, \mu', \phi - \phi') d\phi' \quad (76)$$

and

$$R_{1,model}^{(n)}(-\mu, \mu') \cos(\phi - \phi_0) = \frac{1}{\pi} \int_0^{2\pi} R_{model}^{(n)}(-\mu, \mu', \phi - \phi') \cos(\phi' - \phi_0) d\phi' \quad (77)$$

The BRF model used is that of Rahman et al. [37], modified to allow a nearly linearizable least squares fitting analysis. This modified model has been shown to work sufficiently well for this purpose [16], and is described by

$$R_{model}(-\mu, \mu_0, \phi - \phi_0) = r_0 \cdot \frac{\mu^{k-1} \cdot \mu_0^{k-1}}{(\mu + \mu_0)^{1-k}} \cdot \exp[b \cdot p(\Omega)] \cdot h(-\mu, \mu_0, \phi - \phi_0) \quad (78)$$

with three free parameters (r_0, k, b). The function h is a factor to account for the hot spot,

$$h(-\mu, \mu_0, \phi - \phi_0) = 1 + \frac{1 - r_0}{1 + G(-\mu, \mu_0, \phi - \phi_0)} \quad (79)$$

with

$$G(-\mu, \mu_0, \phi - \phi_0) = \left\{ \left(\frac{1}{\mu^2} - 1 \right) + \left(\frac{1}{\mu_0^2} - 1 \right) + 2 \left[\sqrt{\left(\frac{1}{\mu^2} - 1 \right) \left(\frac{1}{\mu_0^2} - 1 \right)} \right] \cos(\phi - \phi_0) \right\}^{\frac{1}{2}} \quad (80)$$

The function p in Eq. (78) is assumed to depend only on the scattering angle Ω , the angle between the directions of the incident and reflected radiances, and at the present time it is defined to be

$$p(\Omega) = \cos \Omega = -\mu \mu_0 + (1 - \mu^2)^{\frac{1}{2}} \cdot (1 - \mu_0^2)^{\frac{1}{2}} \cdot \cos(\phi - \phi_0) \quad (81)$$

The fitting of R_{model} to $R_{x,y}^{(n)}$ is accomplished by first taking the logarithm of each function, differencing them, and then computing the sum of the squares of the residuals,

$$S = \sum_i [\ln R_{x,y}^{(n)}(-\mu_i, \mu_0, \phi_i - \phi_0) - \ln R_{model}^{(n)}(-\mu_i, \mu_0, \phi_i - \phi_0)]^2 \quad (82)$$

where the summation is over the cameras used and

$$\begin{aligned} \ln R_{model}^{(n)}(-\mu_i, \mu_0, \phi_i - \phi_0) = & \ln r_0^{(n)} + (k^{(n)} - 1) \cdot \ln [\mu_i \mu_0 (\mu_i + \mu_0)] + b^{(n)} \cdot p(\Omega_i) \\ & + \ln h^{(n)}(-\mu_i, \mu_0, \phi_i - \phi_0) \end{aligned} \quad (83)$$

The model is given explicit dependence on the iteration count through the superscript (n) because the parameters are updated every time $R_{x,y}^{(n)}$ is iterated. Aside from the $\ln h^{(n)}$ term in Eq. (83), we note that $\ln R_{model}$ is linear in the three model parameters $\ln r_0$, k , and b . The $\ln h^{(n)}$ term, which contains r_0 , is easily handled by simply using the value of r_0 from the previous iteration. Thus, from Eq. (79),

$$h^{(n)}(-\mu, \mu_0, \phi - \phi_0) = 1 + \frac{1 - r_0^{(n-1)}}{1 + G(-\mu, \mu_0, \phi - \phi_0)} \quad (84)$$

where $r_0^{(-1)}$ is set equal to zero.

The minimization of S in Eq. (82) follows conventional least-squares methodology, in which we establish three equations, $\partial S / \partial \ln r_0^{(n)} = 0$, $\partial S / \partial (\kappa^{(n)} - 1) = 0$, and $\partial S / \partial \beta^{(n)} = 0$ to solve for $r_0^{(n)}$, $\kappa^{(n)}$, and $\beta^{(n)}$. Letting

$$\gamma_i^{(n)} = \ln R_{x,y}^{(n)}(-\mu_i, \mu_0, \phi_i - \phi_0) - \ln h^{(n)}(-\mu_i, \mu_0, \phi_i - \phi_0) \quad (84a)$$

$$m_i = \ln [\mu_i \mu_0 (\mu_i + \mu_0)] \quad (84b)$$

then

$$\begin{bmatrix} \ln r_0^{(n)} \\ \kappa^{(n)} - 1 \\ \beta^{(n)} \end{bmatrix} = \begin{bmatrix} \sum_i 1 & \sum_i m_i & \sum_i p(\Omega_i) \\ \sum_i m_i & \sum_i (m_i)^2 & \sum_i m_i p(\Omega_i) \\ \sum_i p(\Omega_i) & \sum_i m_i p(\Omega_i) & \sum_i p^2(\Omega_i) \end{bmatrix}^{-1} \begin{bmatrix} \sum_i \Upsilon_i^{(n)} \\ \sum_i m_i \Upsilon_i^{(n)} \\ \sum_i p(\Omega_i) \Upsilon_i^{(n)} \end{bmatrix} \quad (84c)$$

from which it is straightforward to obtain $r_0^{(n)}$, $\kappa^{(n)}$, and $\beta^{(n)}$. Once the parameters $r_0^{(n)}$, $k^{(n)}$, and $b^{(n)}$ are found, $R_{0,model}^{(n)}$ and $R_{1,model}^{(n)}$ then can be computed using Eqs. (76) and (77).

As a good initial estimate to start the iteration, we set the BRF equal to the HDRF, i.e.,

$$R_{x,y}^{(0)}(-\mu, \mu_0, \phi - \phi_0) = r_{x,y}(-\mu, \mu_0, \phi - \phi_0) \quad (85)$$

The iteration process expressed by Eq. (75) is then cycled N times, where N is a configurable parameter currently set equal to 1.

Equation deleted (86)

Finally, the DHR is retrieved by using $R_{x,y}^{(N)}$ from the N^{th} iteration in Eq. (67) and assuming the azimuth angle model of Eq. (74). Thus we can write

$$A_{x,y}^{dir}(\mu_0) = 2 \int_0^1 R_{0,x,y}^{(N)}(-\mu, \mu_0) \mu d\mu \quad (87)$$

where

$$R_{0,x,y}^{(N)}(-\mu, \mu_0) = \frac{R_{x,y}^{(N)}(-\mu, \mu_0, \phi_a - \phi_0) \cos(\phi_f - \phi_0) - R_{x,y}^{(N)}(-\mu, \mu_0, \phi_f - \phi_0) \cos(\phi_a - \phi_0)}{\cos(\phi_f - \phi_0) - \cos(\phi_a - \phi_0)} \quad (88)$$

and ϕ_f, ϕ_a are the two azimuth angles for each fore-aft camera pair.

3.3.4.3 Algorithm synopsis and computational specifics

Using the definition of normalized irradiance in Eq. (31) and the irradiance expressions of Eqs. (14) and (41), the basic iteration equation for the algorithm, Eq. (75), can be rewritten as

$$\begin{aligned}
R_{best, x, y}^{(n+1)}(-\mu, \mu_0, \phi - \phi_0) = & \frac{\mu_0 e^{-\tau/\mu_0} + e_b^{diff}(\mu_0)}{[1 - A_{x, y}^{hem}(\mu_0) \cdot s] \cdot \mu_0 e^{-\tau/\mu_0}} \cdot r_{best, x, y}(-\mu, \mu_0, \phi - \phi_0) \\
& - \frac{2\pi}{e^{-\tau/\mu_0}} \cdot \int_0^1 R_{model}^{0(n)}(-\mu, \mu') T_0(-\mu_0, -\mu') d\mu' \\
& - \frac{\pi \cdot \cos(\phi - \phi_0)}{e^{-\tau/\mu_0}} \cdot \int_0^1 R_{model}^{1(n)}(-\mu, \mu') T_1(-\mu_0, -\mu') d\mu' \\
& - \frac{A_{x, y}^{hem}(\mu_0) \cdot s \cdot [\mu_0 e^{-\tau/\mu_0} + e_b^{diff}(\mu_0)]}{[1 - A_{x, y}^{hem}(\mu_0) \cdot s] \cdot \mu_0 e^{-\tau/\mu_0}} \cdot 2 \int_0^1 R_{model}^{0(n)}(-\mu, \mu') \mu' d\mu'
\end{aligned} \tag{89}$$

where the best estimate of the HDRF, $r_{best, x, y}$ is used to obtain the best estimate of BRF, $R_{best, x, y}$. The only unknowns, $R_{0, model}^{(n)}$ and $R_{1, model}^{(n)}$, are computed from Eqs. (76) and (77), using a surface model $R_{model}^{(n)}$ whose parameters are determined by fitting the model to $R_{x, y}^{(n)}$. The initial estimate, $R_{x, y}^{(0)}$, is the hemispherical-directional reflectance factor, $r_{best, x, y}^{dir}$. After the N^{th} and final iteration, the best estimate of directional-hemispherical reflectance, $A_{best, x, y}^{dir}$, is determined from Eq. (87). The integral in Eq. (87) is accomplished by interpolating $R_{0, x, y}^{(N)}$ to the standard Radau point grid, the same as was done with $\rho_{0, x, y}^{refl(n)}$ in Eq. (39). The integrals in Eq. (89) are also evaluated using a Radau quadrature formula, the same way as those integrals in Eq. (32) when computing the surface equivalent reflectance, $\rho_{x, y}^{refl(n)}$.

An estimate is also made of the quality of fit between the retrieved BRF, $R_{x, y}^{(N)}$ and the model BRF, $R_{model}^{(N)}$ after the completion of the last iteration. A measure of the fit residuals can be defined as

$$\Delta = \frac{1}{A_{x, y}^{dir}(\mu_0)} \cdot \frac{\sum_{j=1}^9 v_j \cdot |R_{best, x, y}^{(N)}(-\mu_j, \mu_0, \phi_j - \phi_0) - R_{model}^{(N)}(-\mu_j, \mu_0, \phi_j - \phi_0)|}{\sum_{j=1}^9 v_j} \tag{89a}$$

where $v = 1$ for those camera angles with valid values of the measured equivalent reflectance, and $v = 0$ otherwise.

3.3.4.4 Aerosol mixture requirements of the algorithm

The aerosol optical depth τ_λ , upward diffuse transmittance T_λ , BOA bihemispherical albe-

do s_λ , and the normalized diffuse black surface irradiance $e_{b,\lambda}^{diff}$ for the retrieved aerosol mixtures are described in Eq. (47).

3.3.4.5 Archived algorithm output

For those 1.1 km subregions upon which a BRF/DHR retrieval was performed, the best estimate BRF, R_{best} , is computed at all available view angles and for all available MISR wavelengths. The three BRF model parameters, r_0 , k , and b (obtained from the final iteration), and the measure of the fit residual, Δ , are computed for all available MISR wavelengths. The best estimate DHR, A_{best}^{dir} , is computed for all available MISR wavelengths. All of these parameters are directly archived in the Aerosol/Surface Product. The magnitude of the uncertainties in BRF and DHR are expected to be similar to the uncertainties in HDRF and BHR, and are thus not calculated.

3.3.5 Calculate PAR-integrated BHR and DHR

3.3.5.1 Physics of the problem

For radiation balance and climate studies the shortwave (wavelength-integrated or bolometric) BHR is needed, split into the photosynthetically active radiation (PAR) regime (400 - 700 nm), and the non-PAR regime (>700 nm). Since MISR has only four narrow bands in the shortwave region of the spectrum, additional information concerning the spectral shape of the surface BHR is needed to transform the four MISR spectral BHR's to a full shortwave BHR. This type information can be obtained from MODIS, and we leave the algorithm to retrieve it to the post-launch era. However, since three of the four MISR bands are in the PAR spectral region, we include a PAR-integrated BHR in the at-launch product. A PAR-integrated DHR is also produced since it is a measure of the amount of incident photosynthetically active radiation absorbed by the complete canopy-soil system for a no atmosphere condition and can be compared to FPAR, another MISR surface product parameter, which accounts for the amount of PAR radiation absorbed by the canopy alone.

3.3.5.2 Mathematical description of the algorithm

At wavelength λ , the bihemispherical reflectance, A_λ^{hem} , is the ratio of the radiant exitance M_λ^{hem} to the irradiance E_λ^{hem} at the surface under ambient atmospheric conditions of direct and diffuse illumination. Given A_λ^{hem} from the surface retrieval, we must first obtain M_λ^{hem} and E_λ^{hem} for each 1.1-km subregion. These are calculated according to:

$$E_\lambda^{hem}(\mu_0) = \frac{E_{b,\lambda}(\mu_0)}{1 - A_\lambda^{hem}(\mu_0) \cdot s_\lambda} = \frac{E_{b,\lambda}^{dir}(\mu_0) + E_{b,\lambda}^{diff}(\mu_0)}{1 - A_\lambda^{hem}(\mu_0) \cdot s_\lambda}$$

$$M_\lambda^{hem}(\mu_0) = A_\lambda^{hem}(\mu_0) \cdot E_\lambda^{hem}(\mu_0) \quad (90)$$

where $E_{b,\lambda}$ is the downwelling irradiance for a black surface and s_λ is the BOA bihemispherical albedo for isotropic incident radiation. In contrast with the previous sections, the explicit spatial dependence (the subregion x,y coordinates) has been suppressed in the notation and the spectral dependence (wavelength λ) is now emphasized. To compute the PAR-integrated bihemispherical reflectance, A_{PAR}^{hem} , for a 17.6-km region, we first average the values of M_λ^{hem} and E_λ^{hem} , determined from Eq. (90), over the subregions for which there was a successful surface retrieval in the blue, green, and red bands simultaneously. Calling these spatial averages $\langle M_\lambda^{hem} \rangle$ and $\langle E_\lambda^{hem} \rangle$, the equation for the PAR-integrated BHR, A_{PAR}^{hem} , is

$$A_{PAR}^{hem}(\mu_0) = \frac{\int_{400}^{700} \langle M_\lambda^{hem}(\mu_0) \rangle d\lambda}{\int_{400}^{700} \langle E_\lambda^{hem}(\mu_0) \rangle d\lambda} \quad (91)$$

Recasting Eqs. (90) and (91) in terms of the normalized irradiances and radiant exitances defined by Eq. (31), we have

$$e_\lambda^{hem}(\mu_0) = \frac{\mu_0 e^{-\tau_\lambda/\mu_0} + e_{b,\lambda}^{diff}(\mu_0)}{1 - A_\lambda^{hem}(\mu_0) \cdot s_\lambda}$$

$$m_\lambda^{hem}(\mu_0) = A_\lambda^{hem}(\mu_0) \cdot e_\lambda^{hem}(\mu_0) \quad (92)$$

and

$$A_{PAR}^{hem}(\mu_0) = \frac{\int_{400}^{700} \langle m_\lambda^{hem}(\mu_0) \rangle E_{0,\lambda} d\lambda}{\int_{400}^{700} \langle e_\lambda^{hem}(\mu_0) \rangle E_{0,\lambda} d\lambda} \quad (93)$$

where the solar irradiance spectrum, $E_{0,\lambda}$, is known for all wavelengths. However, Eq. (92) only provides $\langle m_\lambda^{hem} \rangle$ and $\langle e_\lambda^{hem} \rangle$ at the 4 MISR wavelengths, of which only 3 are within the PAR region. Thus, in order to carry out the integrals in Eq. (93) we need to make an assumption about the spectral shape of $\langle m_\lambda^{hem} \rangle$ and $\langle e_\lambda^{hem} \rangle$.

First, make the simplification that $\langle m_\lambda^{hem} \rangle$ and $\langle e_\lambda^{hem} \rangle$ are monochromatic values at the MISR band-center wavelengths. They are actually integrated over the 15 to 30 nm bandwidths of

the filters, but this simplification is probably justifiable, given the other assumptions. Next, assume a piecewise linear variation in $\langle m_\lambda^{hem} \rangle$ and $\langle e_\lambda^{hem} \rangle$ over the 400 - 700 nm region, i.e., letting F_λ represent either $\langle m_\lambda^{hem} \rangle$ or $\langle e_\lambda^{hem} \rangle$:

$$\begin{aligned} F_\lambda &= F_1, & 400 \leq \lambda \leq \lambda_1 \\ F_\lambda &= F_1 + (\lambda - \lambda_1)(F_2 - F_1)/(\lambda_2 - \lambda_1), & \lambda_1 \leq \lambda \leq \lambda_2 \\ F_\lambda &= F_2 + (\lambda - \lambda_2)(F_3 - F_2)/(\lambda_3 - \lambda_2), & \lambda_2 \leq \lambda \leq \lambda_3 \\ F_\lambda &= F_3, & \lambda_3 \leq \lambda \leq 700 \end{aligned}$$

where the subscripts 1, 2, 3 denote the blue, green, and red bands respectively.

Now, let

$$\begin{aligned} S_1 &= \int_{400}^{\lambda_1} E_{0,\lambda} d\lambda & S_2 &= \int_{\lambda_1}^{\lambda_2} E_{0,\lambda} d\lambda & S_3 &= \frac{1}{(\lambda_2 - \lambda_1)} \int_{\lambda_1}^{\lambda_2} (\lambda - \lambda_1) E_{0,\lambda} d\lambda \\ S_4 &= \int_{\lambda_2}^{\lambda_3} E_{0,\lambda} d\lambda & S_5 &= \frac{1}{(\lambda_3 - \lambda_2)} \int_{\lambda_2}^{\lambda_3} (\lambda - \lambda_2) E_{0,\lambda} d\lambda & S_6 &= \int_{\lambda_3}^{700} E_{0,\lambda} d\lambda \end{aligned} \quad (94)$$

Since these constants only depend on the MISR band center wavelengths and the solar irradiance spectrum, they can be calculated pre-flight. Then

$$\int_{400}^{700} F_\lambda E_{0,\lambda} d\lambda = (S_1 + S_2 - S_3)F_1 + (S_3 + S_4 - S_5)F_2 + (S_5 + S_6)F_3 \quad (95)$$

and if we define

$$w_1 = S_1 + S_2 - S_3 \quad w_2 = S_3 + S_4 - S_5 \quad w_3 = S_5 + S_6 \quad (96)$$

and then normalize these such that

$$\hat{w}_1 = \frac{w_1}{w_1 + w_2 + w_3} \quad \hat{w}_2 = \frac{w_2}{w_1 + w_2 + w_3} \quad \hat{w}_3 = \frac{w_3}{w_1 + w_2 + w_3} \quad (97)$$

then

$$A_{PAR}^{hem}(\mu_0) = \frac{\hat{w}_1 \langle m_1^{hem}(\mu_0) \rangle + \hat{w}_2 \langle m_2^{hem}(\mu_0) \rangle + \hat{w}_3 \langle m_3^{hem}(\mu_0) \rangle}{\hat{w}_1 \langle e_1^{hem}(\mu_0) \rangle + \hat{w}_2 \langle e_2^{hem}(\mu_0) \rangle + \hat{w}_3 \langle e_3^{hem}(\mu_0) \rangle} \quad (98)$$

with m^{hem} and e^{hem} defined by Eq. (92).

An identical calculation is done to obtain the PAR-integrated DHR, provided Eq. (92) is modified as follows to represent the “no atmosphere” situation:

$$\begin{aligned} e_{\lambda}^{dir}(\mu_0) &= \mu_0 \\ m_{\lambda}^{dir}(\mu_0) &= A_{\lambda}^{dir}(\mu_0) \cdot e_{\lambda}^{dir}(\mu_0) \end{aligned} \quad (99)$$

Using Eq. (99), the PAR-integrated DHR is then

$$A_{PAR}^{dir}(\mu_0) = \frac{\hat{w}_1 \langle m_1^{dir}(\mu_0) \rangle + \hat{w}_2 \langle m_2^{dir}(\mu_0) \rangle + \hat{w}_3 \langle m_3^{dir}(\mu_0) \rangle}{\hat{w}_1 \langle e_1^{dir}(\mu_0) \rangle + \hat{w}_2 \langle e_2^{dir}(\mu_0) \rangle + \hat{w}_3 \langle e_3^{dir}(\mu_0) \rangle} \quad (100)$$

with the same weights as defined in Eq. (97). These weights are precalculated and obtained from the ARP.

3.3.5.3 Aerosol mixture requirements of the algorithm

The optical depth τ_{λ} , the BOA bihemispherical albedo, s_{λ} , and the normalized diffuse black surface irradiance, $e_{b,\lambda}^{diff}$ for the retrieved aerosol mixtures are described in Eq. (47).

3.3.5.4 Archived algorithm output

For those 1.1 km subregions upon which a BRF/DHR retrieval was performed, the PAR-integrated BHR, A_{PAR}^{hem} , and the PAR-integrated DHR, A_{PAR}^{dir} , are computed and directly archived in the Aerosol/Surface Product.

3.3.6 Determine subregion LAI and associated uncertainty

3.3.6.1 Physics of the problem

A fundamental structural variable of plant canopies is the green leaf-area index (LAI), defined as the amount of one-side green leaf area per unit ground area, integrated from the top of the canopy to the ground. Besides being an indicator of green phytomass, it can be used in the estimation of other canopy properties, such as FPAR. We plan to determine LAI at 1.1 km (subregion)

spatial resolution by means of sophisticated 3-dimensional modeling of various types of vegetative canopies from which the necessary radiative transfer parameters needed in the LAI retrieval are precomputed and stored in the Canopy Architecture Radiative Transfer (CART) file, part of the Ancillary Land Biome (ALB) Dataset. Depending on biome type, the model input parameters to the radiative transfer calculations include fractional ground cover, understory LAI, leaf normal orientation, woody material fraction, leaf and crown sizes, leaf chlorophyll content, soil reflectance and solar zenith angle. For further information on the generation of the CART file and the ALB Dataset, see [M-6].

The LAI retrieval algorithm first determines if the subregion has a meaningful amount of vegetation by calculating the normalized difference vegetation index (NDVI) using the previously retrieved DHR's in the red and NIR bands. If the NDVI is \leq a threshold value $NDVI_{\text{thresh}}$, the subregion is classified as barren and no additional processing is performed for the LAI (in this event LAI is considered to be 0.0). For an $NDVI > NDVI_{\text{thresh}}$, a determination is made of which biome types within the subregion, out of a population of six major biome types -- grasses and cereal crops, shrublands, broadleaf crops, savanna, broadleaf forests, and needle forests -- are consistent with the MISR observations. To minimize the possibility of multiple biome types and/or canopy structures as acceptable solutions, the algorithm is designed to utilize all the available information from the observations by means of a two step process. The first step involves a comparison of the retrieved spectral hemispherically integrated reflectances (DHR's and BHR's) with those determined for the various candidate biome/canopy types and which also depend on LAI and soil reflectance. Only those candidate biome/canopy/soil models which pass this comparison test can then proceed to the second step which is a comparison of their directional reflectances at the MISR angles to the retrieved spectral directional reflectances (i.e., the BRF's). From the remaining set, a "best" value of LAI is chosen, using the results from the biome which has the least spread in its LAI values as a function of soil type.

3.3.6.2 Mathematical description of the algorithm

For each 1.1 km subregion, the Normalized Difference Vegetation Index (NDVI) can be written as

$$NDVI(\mu_0) = \frac{A_4^{dir}(\mu_0) - A_3^{dir}(\mu_0)}{A_4^{dir}(\mu_0) + A_3^{dir}(\mu_0)} \quad (101)$$

where A_4^{dir} and A_3^{dir} are the DHR's in the MISR near-IR and red bands (bands 4 and 3), respectively, for a solar zenith angle whose cosine is μ_0 .

We first compare the NDVI to the threshold value, $NDVI_{\text{thresh}}$. If the $NDVI \leq NDVI_{\text{thresh}}$, the subregion is considered to be non-vegetated (barren) and the remaining steps in the LAI algo-

rithm are skipped. If the inputs required to calculated NDVI are unavailable, the subregion is considered to be of unknown type, and the remaining steps in the LAI algorithm are skipped. Otherwise, we proceed on to the first comparison test.

The first comparison test implemented by the algorithm is based on hemispherically integrated reflectances at the four MISR wavelengths and as such, a merit function Δ_1 is defined as

$$\begin{aligned} \Delta_1(bio, lai, soil, \mu_0) = & \\ & \frac{\gamma}{N_{dir}} \sum_{l=1}^4 v_{dir}(l) \cdot \left[\frac{A^{dir}(\lambda_l, \mu_0) - A_{model}^{dir}(\lambda_l, bio, lai, soil, \mu_0)}{\Delta A^{hem}(\lambda_l, \mu_0)} \right]^2 + \\ & + \frac{(1-\gamma)}{N_{hem}} \sum_{l=1}^4 v_{hem}(l) \cdot \left[\frac{A^{hem}(\lambda_l, \mu_0) - A_{model}^{hem}(\lambda_l, bio, lai, soil, \mu_0)}{\Delta A^{hem}(\lambda_l, \mu_0)} \right]^2 \end{aligned} \quad (102)$$

where

A^{dir} and A^{hem} are the retrieved hemispherical-directional reflectance (DHR) and bi-hemispherical reflectance (BHR), respectively, at the MISR wavelengths;

ΔA^{hem} is the retrieved uncertainty in A^{hem} from Eq. (58) (note that we use this same quantity as an estimate of the uncertainty in A^{dir} as well);

A_{model}^{dir} and A_{model}^{hem} are the DHR and BHR of the candidate canopy/soil model, specified by biome type, effective canopy LAI (a combination of canopy LAI and ground cover fraction), and soil model via the three parameters, *bio*, *lai*, and *soil*, respectively, in the CART file;

$v_{dir}(l) = 1$ if retrieved values of A^{dir} and ΔA^{hem} exist at wavelength λ_l , otherwise $v_{dir}(l) = 0$;

N_{dir} is the number of wavelengths for which $v_{dir} = 1$, i.e.,

$$N_{dir} = \sum_{l=1}^4 v_{dir}(l) \quad (103)$$

$v_{hem}(l) = 1$ if retrieved values of A^{hem} and ΔA^{hem} exist at wavelength λ_l , otherwise $v_{hem}(l) = 0$;

N_{hem} is the number of wavelengths for which $v_{hem} = 1$, i.e.,

$$N_{hem} = \sum_{l=1}^4 v_{hem}(l) \quad (104)$$

γ is a configurable parameter used to “tune” the merit function to relative proportions of DHR and BHR. For example, if $\gamma = 0$, the merit function depends entirely on BHR’s. The inclusion of both DHR and BHR is employed to take advantage of the potentially different sensitivities these parameters have to canopy structure. At present, we set $\gamma = 0$.

The merit function is defined and normalized such that a model which differs from the retrieved DHR and BHR values by an amount equivalent or less than the retrieval uncertainty will result in a value of Δ_1 on the order of unity. We establish a configurable threshold value $\Delta_{1,thresh}$, and consider a model to pass this test if

$$\Delta_1(bio, lai, soil, \mu_0) \leq \Delta_{1,thresh} \quad (105)$$

where $\Delta_{1,thresh}$ is currently set to 1.

The predetermined values of the effective LAI for the various canopy/soil models are found in the CART file. Now, for each biome type and LAI value, let N_1 be the count of how many times this LAI value passed the Δ_1 merit function test (considering all of the various soil types associated with this biome). If LAI is a particular LAI value and the total number of LAI values is N_{LAI} , then, the total number of valid solutions after completion of the Δ_1 merit function test, $N_{sol,1}$, is given by

$$N_{sol,1}(bio) = \sum_{lai=1}^{N_{LAI}} N_1(bio, lai) \quad (106)$$

and, for those biomes in which $N_{sol,1} > 0$, the mean LAI is given by

$$\overline{LAI}_1(bio) = \frac{\sum_{lai=1}^{N_{LAI}} N_1(bio, lai) \cdot LAI(bio, lai)}{N_{sol,1}(bio)} \quad (107)$$

and a measure of the spread in LAI values for each biome from

$$\Delta LAI_1(bio) = \sqrt{\frac{\sum_{lai=1}^{N_{LAI}} N_1(bio, lai) \cdot [LAI(bio, lai) - \overline{LAI}_1(bio)]^2}{N_{sol,1}(bio)}} \quad (108)$$

The parameters $N_{sol,1}$, \overline{LAI}_1 , and ΔLAI_1 are archived for each biome type. Equations (106) - (108) provide a useful conceptual framework for understanding the meaning of these parameters. However, in practice, these parameters are more easily calculated using running sums as described in §3.3.6.3, Eqs. (118) - (120). If $N_{sol,1} = 0$ for a given biome, fill values are used for \overline{LAI}_1 and ΔLAI_1 . A test is also performed to check whether \overline{LAI}_1 is the average LAI in the saturation domain, defined as all $N_{sol,1}$ solutions having essentially equal probability of occurrence. If

$$\min_{1 \leq k \leq N_{sat}} ([L_k^* - \overline{LAI}_1(bio)]^2 + [d_k^* - \Delta LAI_1(bio)]^2) \leq \delta \quad (109)$$

is satisfied for a prescribed accuracy δ , where δ is a configurable parameter, then \overline{LAI}_1 is considered to be a solution under a condition of saturation and is noted by archiving the LAI spread as $-\Delta LAI_1$. The saturation curve, (L_k^*, d_k^*) , $k = 1, 2, \dots, N_{sat}$, is stored in the CART file [M-6].

If the merit function Δ_1 for a particular canopy/soil model satisfies the relation in Eq. (105), then that model proceeds on to the second comparison test in the algorithm. In this test directional reflectances are now used to discriminate between competing candidate models. A second merit function Δ_2 is defined as

$$\begin{aligned} \Delta_2(bio, lai, \mu_0) = & \\ = & \frac{\sum_{l=1}^4 \sum_{j=1}^9 v'(l, j) \cdot \left[\frac{R(\lambda_l, -\mu_j, \mu_0, \Delta\phi_j) - R_{model}(\lambda_l, bio, lai, -\mu_j, \mu_0, \Delta\phi_j)}{\Delta r(\lambda_l, \mu_0)} \right]^2}{\sum_{l=1}^4 \sum_{j=1}^9 v'(l, j)} \end{aligned} \quad (110)$$

where

R is the retrieved bidirectional reflectance factor (BRF) at the MISR view angles and wavelengths;

R_{model} is the BRF for the candidate canopy model for the same viewing geometry and wavelengths,

Δr is the retrieved HDRF camera-averaged uncertainty (assumed to be equivalent to the BRF uncertainty);

$v'(l, j) = 1$ if a retrieved value of R exists at wavelength l and camera j ; otherwise $v'(l, j) = 0$.

A model passes this second test if

$$\Delta_2(bio, lai, soil, \mu_0) \leq \Delta_{2, \text{thresh}} \quad (111)$$

where $\Delta_{2, \text{thresh}}$ is a configurable threshold parameter currently set to 1.

For each biome type, we then determine the total number of valid solutions after completion of the second merit function test, $N_{sol,2}$, and for those biomes in which $N_{sol,2} > 0$ we also compute the parameters \overline{LAI}_2 and ΔLAI_2 in an analogous manner as was done for the first merit test. These are archived for each biome type. Again, a saturation test is performed on \overline{LAI}_2 in the same way as described previously for \overline{LAI}_1 . If saturation is evident, then the spread is archived as $-\Delta LAI_2$. If $N_{sol,2} = 0$ for a given biome, fill values are used for \overline{LAI}_2 and ΔLAI_2 .

3.3.6.3 Algorithm synopsis and computational specifics

The speed of execution of the LAI algorithm is enhanced considerably through the use of a look-up table approach which allows the necessary parameters, which describe the radiative transfer of atmospheric radiation within complex canopies, to be evaluated in a simple manner. This tabular information is contained in the Canopy Architecture Radiative Transfer (CART) file of the ALB Dataset. The particular four CART file parameters needed in the LAI algorithm are A_{model}^{dir} , A_{model}^{diff} , W_1 , and W_2 . When computing Δ_1 in Eq. (102), A_{model}^{dir} is read directly from the CART and A_{model}^{hem} is given by

$$A_{model}^{hem}(\lambda, bio, lai, soil, \mu_0) = f^{dir}(\lambda, \mu_0) \cdot A_{model}^{dir}(\lambda, bio, lai, soil, \mu_0) + [1 - f^{dir}(\lambda, \mu_0)] \cdot A_{model}^{diff}(\lambda, bio, lai, soil, \mu_0) \quad (112)$$

where f^{dir} is the ratio of direct to total (direct + diffuse) irradiance on top of the canopy. An expression for f^{dir} can be written as, using Eq. (92),

$$f^{dir}(\lambda, \mu_0) = \frac{e^{dir}(\lambda, \mu_0)}{e^{hem}(\lambda, \mu_0)} = \frac{\mu_0 e^{-\tau(\lambda)/\mu_0} \cdot [1 - A^{hem}(\lambda, \mu_0) \cdot s(\lambda)]}{\mu_0 e^{-\tau(\lambda)/\mu_0} + e_b^{diff}(\lambda, \mu_0)} \quad (113)$$

where the spectrally-dependent quantities e_b^{diff} (the black surface diffuse irradiance), τ (the

atmospheric optical depth), and s (the BOA bihemispherical albedo), have been previously determined in earlier steps of the aerosol and surface retrieval process [see Eq. (47)].

Likewise, when computing Δ_2 in Eq. (110), R_{model} is given by

$$R_{model}(\lambda, bio, lai, -\mu, \mu_0, \Delta\phi) = W_1(\lambda, bio, lai, -\mu, \mu_0, \Delta\phi) + W_2(\lambda, bio, lai, -\mu, \mu_0, \Delta\phi) \cdot A^{dir}(\lambda, \mu_0) \quad (114)$$

where A^{dir} is the retrieved DHR. The formulation of A_{model}^{hem} and R_{model} expressed by Eqs. (112) and (114), respectively, minimizes the computation time needed to perform the two merit tests which define the essence of the LAI algorithm. In addition, the use of bins to partition the angular variables $-\mu$, μ_0 , and $\Delta\phi$ in the CART file requires only that the correct bin holding each of these angular variables be identified to determine the values of the required four parameters, thus bypassing any need for angular interpolation.

As mentioned previously, the parameters N_{soil} , \overline{LAI} , and ΔLAI for the two merit tests, described by Eqs. (106) - (108) respectively, can be efficiently computed using running sums. For a particular biome type, described by the CART file parameter bio , the first merit test is performed for all soil models and effective canopy LAI models, described by the CART file parameters $soil$ and lai , respectively. Thus,

$$S_{11}^{LAI}(bio) = \sum_{soil=1}^{N_{soil}} \sum_{lai=1}^{N_{LAI}} \Gamma_1(bio, soil, lai) \quad (115)$$

$$S_{21}^{LAI}(bio) = \sum_{lai=1}^{N_{LAI}} LAI(bio, lai) \sum_{soil=1}^{N_{soil}} \Gamma_1(bio, soil, lai) \quad (116)$$

$$S_{31}^{LAI}(bio) = \sum_{lai=1}^{N_{LAI}} LAI^2(bio, lai) \sum_{soil=1}^{N_{soil}} \Gamma_1(bio, soil, lai) \quad (117)$$

so that

$$N_{sol,1}(bio) = S_{11}^{LAI}(bio) \quad (118)$$

$$\overline{LAI}_1(bio) = \frac{S_{21}^{LAI}(bio)}{S_{11}^{LAI}(bio)} \quad (119)$$

$$\Delta LAI_1(bio) = \sqrt{\frac{S_{31}^{LAI}(bio)}{S_{11}^{LAI}(bio)} - [\overline{LAI}_1(bio)]^2} \quad (120)$$

Here, $\Gamma_1(bio, soil, lai) = 1$ if the model defined by *bio*, *soil* and *lai* passed the Δ_1 merit function test, and $\Gamma_1(bio, soil, lai) = 0$ otherwise. For the second merit test we have

$$S_{12}^{LAI}(bio) = \sum_{lai} \Gamma_2(bio, lai) \quad (121)$$

$$S_{22}^{LAI}(bio) = \sum_{lai} \Gamma_2(bio, lai) \cdot LAI(bio, lai) \quad (122)$$

$$S_{32}^{LAI}(bio) = \sum_{lai} \Gamma_2(bio, lai) \cdot LAI^2(bio, lai) \quad (123)$$

so that

$$N_{sol,2}(bio) = S_{12}^{LAI}(bio) \quad (124)$$

$$\overline{LAI}_2(bio) = \frac{S_{22}^{LAI}(bio)}{S_{12}^{LAI}(bio)} \quad (125)$$

$$\Delta LAI_2(bio) = \sqrt{\frac{S_{32}^{LAI}(bio)}{S_{12}^{LAI}(bio)} - [\overline{LAI}_2(bio)]^2} \quad (126)$$

In this case $\Gamma_2(bio, lai) = 1$ if the model defined by *bio* and *lai* passed both the Δ_1 and Δ_2 merit function tests, and $\Gamma_2(bio, lai) = 0$ otherwise. The summations in Eqs. (121) - (123) are only over those values of *lai* for the models which passed the first merit test.

3.3.6.4 Archived algorithm output

For each 1.1-km subregion within which a BRF/DHR retrieval was performed, the LAI algorithm results are archived in the Aerosol/Surface Product. For each biome type, we archive $N_{sol,1}$, \overline{LAI}_1 , ΔLAI_1 , and $N_{sol,2}$, \overline{LAI}_2 , ΔLAI_2 . Because the value of NDVI establishes whether it is necessary to calculate a value of LAI (LAI is defined to be 0.0 for $NDVI \leq NDVI_{thresh}$), we also archive NDVI in the product.

3.3.7 Determine subregion FPAR and its uncertainty

3.3.7.1 Physics of the problem

A measure of photosynthetic capacity is FPAR which is the fraction of incident photosynthetically active radiation that is absorbed by photosynthesizing tissue in a plant canopy. Theoretical canopy radiative transfer models for the six biome types are used to relate the estimate of LAI determined above to the subregion FPAR.

When all candidate canopy/soil models are unsuccessful in passing the two comparison tests, no biome identification and canopy LAI results are obtained, and the algorithm defaults to an NDVI-FPAR regression analysis to obtain only an estimate of FPAR. Theoretical and empirical evidence support a relationship between FPAR and NDVI, dependent on biome type and solar zenith angle [33], [34]. As such, we plan to use the surface NDVI, derived from the retrieved directional-hemispherical reflectances (DHR's) in the MISR red and near-IR bands, to estimate FPAR at the 1.1 km spatial resolution in this default mode. Since the NDVI-FPAR relationship depends on biome type, the default algorithm requires the use of the Biome Classification Map which contains the biome type at 1.1 km resolution. The NDVI-FPAR relationship is found to be linear in most cases, with the exception of those canopies with bright backgrounds. These relationships are similar to those reported in the literature based on field data and model results (e.g., [2], [36]), and are obtained prior to launch by making repeated runs of the radiative transfer canopy model for various scenarios of input parameters for each biome type. The same models used to generate the LAI-FPAR relationships used in the primary algorithm are also regressed to produce NDVI-FPAR relationships which depend only on biome type and solar zenith angle.

Subregion (1.1-km) FPAR and the associated uncertainty are established as intermediate parameters only, and are not archived. The archived parameters are provided for 17.6-km regions (see §3.3.8).

3.3.7.2 Mathematical description of the algorithm

FPAR is defined as the fraction of photosynthetically active radiation absorbed by green elements of the vegetation canopy. Therefore,

$$FPAR(bio, lai, \mu_0) = \frac{\int_{400}^{700} a^{hem}(\lambda, \mu_0) e_{\lambda}^{hem}(\mu_0) E_{0, \lambda} d\lambda}{\int_{400}^{700} e_{\lambda}^{hem}(\mu_0) E_{0, \lambda} d\lambda} \quad (127)$$

Here, a^{hem} describes both the absorption within the canopy for the case of black ground and the additional absorption within the canopy due to the interaction between the ground (soil and/or understory) and the canopy, $E_{0,\lambda}$ is the TOA solar irradiance spectrum, and e_{λ}^{hem} is the normalized incident irradiance [see Eq. (92)].

The canopy absorption a^{hem} is determined directly, using parameters taken from the CART file and the retrieved BHR, A^{hem} . However care must be taken to ensure that the contribution of the ground to the canopy absorptance does not exceed the uncertainty in A^{hem} . This is done by performing the test (see section 6.5.3.8 in [M-6]),

$$0 < A^{hem}(\lambda, \mu_0) - r_{bs}^{hem}(\lambda, bio, lai, \mu_0) < T^{hem}(\lambda, bio, lai, \mu_0), \quad (128)$$

where r_{bs}^{hem} is the BHR for the canopy with a black ground and T^{hem} is a parameter dependent on the canopy transmission and absorption properties. If this test is not satisfied, then a^{hem} becomes independent of the canopy model and is computed as

$$a^{hem}(\lambda, \mu_0) = 1 - A^{hem}(\lambda, \mu_0). \quad (129)$$

When A^{hem} is not available for any reason at a given wavelength, then A_{model}^{hem} is substituted. In this case the test described by (128) is automatically satisfied and need not be performed.

The integrals in Eq. (127) are computed in an identical fashion to those describing A_{PAR}^{hem} and A_{PAR}^{dir} . Thus,

$$FPAR(bio, lai, \mu_0) = \frac{\hat{w}_1 a_1^{hem}(\mu_0) + \hat{w}_2 a_2^{hem}(\mu_0) + \hat{w}_3 a_3^{hem}(\mu_0)}{\hat{w}_1 e_1^{hem}(\mu_0) + \hat{w}_2 e_2^{hem}(\mu_0) + \hat{w}_3 e_3^{hem}(\mu_0)} \quad (130)$$

where the weights \hat{w}_i are given by Eq. (97) and e_i^{hem} by Eq. (92). Again, if A^{hem} is not available at a given wavelength, then A_{model}^{hem} is used in Eq. (92).

Now, if there is at least one solution biome/canopy model for a given subregion, then to calculate the best estimate of the subregion FPAR, we consider the set of \overline{LAI}_2 and ΔLAI_2 values for all biomes with $N_{sol,2} > 0$. Among this set we find the biome with the minimum value of ΔLAI_2 . If the same minimum value is found for more than one biome, we choose the biome from this set that has the smallest value of \overline{LAI}_2 . If this process establishes a unique biome type, we denote this biome as bio' , and we let the associated estimates of LAI and LAI spread be written as \overline{LAI}_2' and $\Delta LAI_2'$. If this process fails to identify a unique biome type, the subregion is considered to have an ambiguous biome type, and is not included in the regional FPAR calculation nor processed further.

If there are no solution biome/canopy models for a given subregion, then the algorithm enters the default mode in which the Biome Classification Map in the Ancillary Land Biome Dataset is accessed to find the biome type assigned to that particular subregion and the appropriate NDVI-FPAR relationship is used, dependent on pre-established biome type bio'' and μ_0 to obtain a value for the subregion FPAR. The relationship is linear, i.e.,

$$FPAR_{subregion} = F_0(bio'', \mu_0) + F_1(bio'', \mu_0) \cdot NDVI(\mu_0) \quad (131)$$

where F_0 and F_1 are regression coefficients. For geographic locations which the Ancillary Land Biome Dataset does not classify as one of the six biome types (e.g., classified as barren), we set $FPAR_{subregion} = 0$. The regression coefficients F_0 and F_1 are provided for three ranges of solar zenith angle, and are contained within the NDVI-FPAR Regression file of the ALB Dataset.

For the default FPAR algorithm, the associated uncertainty is considered to arise from two sources. The first is the experimental error in the determination of NDVI. The second is the variability in the FPAR-NDVI relationship resulting from uncertainties in the parameters underlying the biome models.

Based on the results presented in §3.5.2, a natural variability in NDVI of ~ 0.1 is not unreasonable for a given biome type. Let δ_{NDVI}^{nat} represent this uncertainty in NDVI. From Eq. (101), we derive that the instrument uncertainty in NDVI, assuming that the uncertainty in DHR is equal to the uncertainty in BHR and that the uncertainties in bands 3 and 4 are uncorrelated, is given by:

$$\delta_{NDVI}^{instr} = \frac{2}{(A_4^{dir} + A_3^{dir})^2} \cdot \sqrt{(A_4^{dir} \Delta A_3^{hem})^2 + (A_3^{dir} \Delta A_4^{hem})^2} \quad (132)$$

We then specify the overall uncertainty in NDVI to be

$$\delta_{NDVI} = \sqrt{(\delta_{NDVI}^{nat})^2 + (\delta_{NDVI}^{instr})^2} \quad (133)$$

and from Eq. (131) we obtain that

$$\delta FPAR_{subregion} = F_1(bio'', \mu_0) \cdot \delta_{NDVI} \quad (134)$$

Finally, we note that if $NDVI \leq NDVI_{thresh}$, neither the primary or default algorithms are used. Rather, we set

$$FPAR_{subregion} = 0.0$$

$$\delta FPAR_{subregion} = 0.0 \quad (135)$$

3.3.7.3 Algorithm synopsis and computational specifics

The expression for FPAR in Eq. (130) is described solely in terms of retrieved parameters (f^{dir} , e^{hem} , and A^{hem}) and seven parameters stored in the CART file. These seven parameters, defined to minimize the computation time for a^{hem} , are r_{bs}^{dir} , r_{bs}^{diff} , T^{dir} , T^{diff} , F_1^{dir} , F_1^{diff} , and F_2 . Then the algorithm to compute a^{hem} can be expressed as

$$\begin{aligned} a^{hem}(\lambda, \mu_0) &= f^{dir}(\lambda, \mu_0) \cdot F_1^{dir}(\lambda, bio, lai, \mu_0) \\ &\quad + [1 - f^{dir}(\lambda, \mu_0)] \cdot F_1^{diff}(\lambda, bio, lai, \mu_0) \\ &\quad + F_2(\lambda, bio, lai) \cdot A^{hem}(\lambda, \mu_0) \\ &\quad \text{if } 0 < A^{hem}(\lambda, \mu_0) - r_{bs}^{hem}(\lambda, bio, lai, \mu_0) < T^{hem}(\lambda, bio, lai, \mu_0) \\ a^{hem}(\lambda, \mu_0) &= 1 - A^{hem}(\lambda, \mu_0) \quad \text{otherwise.} \end{aligned} \quad (136)$$

Here,

$$\begin{aligned} r_{bs}^{hem}(\lambda, bio, lai, \mu_0) &= f^{dir}(\lambda, \mu_0) \cdot r_{bs}^{dir}(\lambda, bio, lai, \mu_0) \\ &\quad + [1 - f^{dir}(\lambda, \mu_0)] \cdot r_{bs}^{diff}(\lambda, bio, lai, \mu_0) \end{aligned} \quad (137)$$

$$\begin{aligned} T^{hem}(\lambda, bio, lai, \mu_0) &= f^{dir}(\lambda, \mu_0) \cdot T^{dir}(\lambda, bio, lai, \mu_0) \\ &\quad + [1 - f^{dir}(\lambda, \mu_0)] \cdot T^{diff}(\lambda, bio, lai, \mu_0) \end{aligned} \quad (138)$$

and f^{dir} is given by Eq. (113). Those six CART file parameters, dependent on the angular variable μ_0 , are gridded such that a closest angle determination is sufficiently accurate and, thus, no angular interpolation is required.

In addition to the CART canopy model parameters the computation of a^{hem} also depends on the retrieved parameters A^{hem} and f^{dir} . If the BRF A^{hem} is not available at a particular wavelength, then A_{model}^{hem} , as defined in Eq. (112), is used instead. However, A_{model}^{hem} in this expression also depends on f^{dir} and f^{dir} in turn depends on A^{hem} (or A_{model}^{hem} in this case) via Eq. (113). So, an alternative form for computing f^{dir} is necessary, found by substituting Eq. (112) into Eq. (113) and solving for f^{dir} . We find that

$$f^{dir}(\lambda, \mu_0) = \frac{G_1(\lambda, \mu_0) - A_{model}^{diff}(\lambda, bio, lai, soil, \mu_0) \cdot G_2(\lambda, \mu_0)}{1 + [A_{model}^{dir}(\lambda, bio, lai, soil, \mu_0) - A_{model}^{diff}(\lambda, bio, lai, soil, \mu_0)] \cdot G_2(\lambda, \mu_0)} \quad (139)$$

where

$$G_1(\lambda, \mu_0) = \frac{\mu_0 e^{-\tau(\lambda)/\mu_0}}{\mu_0 e^{-\tau(\lambda)/\mu_0} + e_b^{diff}(\lambda, \mu_0)} \quad (140)$$

$$G_2(\lambda, \mu_0) = s(\lambda) \cdot G_1(\lambda, \mu_0) \quad (141)$$

Eq. (139) is used to compute f^{dir} instead of Eq. (113) when A^{hem} is not available at a given wavelength.

Note that the parameters \hat{w}_i are stored in both the ARP and the CART file. This is a result of the algorithm development history, in which these parameters were required for generation of the PAR-integrated BHR and DHR, and at the time those algorithms were developed the LAI/FPAR algorithm and the CART file had not yet been established.

To compute the estimate of FPAR and its uncertainty for the subregion we proceed as follows. During the application of the second merit function test for determining LAI, we also compute the additional running sums,

$$S_{22}^{FPAR}(bio, \mu_0) = \sum_{lai} \Gamma_2(bio, lai) \cdot FPAR(bio, lai, \mu_0) \quad (142)$$

$$S_{32}^{FPAR}(bio, \mu_0) = \sum_{lai} \Gamma_2(bio, lai) \cdot [FPAR(bio, lai, \mu_0)]^2 \quad (143)$$

where the summations are only over those values of lai for the models of biome type bio which passed the first merit test. The parameter Γ_2 is the same as that used in Eqs. (121)-(123). Following the determination of the appropriate biome type, bio' , we then obtain the estimate of FPAR from:

$$FPAR_{subregion} = \frac{S_{22}^{FPAR}(bio', \mu_0)}{S_{12}^{LAI}(bio')} \quad (144)$$

and an associated uncertainty of

$$\delta FPAR_{subregion} = \sqrt{\frac{S_{32}^{FPAR}(bio', \mu_0)}{S_{12}^{LAI}(bio')} - [FPAR_{subregion}]^2} \quad (145)$$

where S_{12}^{LAI} is given by Eq. (121).

3.3.8 Determine regional FPAR

3.3.8.1 Physics of the problem

The FPAR for the 17.6 km region is the ratio of the absorbed PAR for the region (APAR) to the incident PAR for the region (IPAR). We assume that the subregion IPAR, $IPAR_{subregion}$, is uniform over a region such that FPAR for the region is just the averaged subregion FPAR.

3.3.8.2 Mathematical description of the algorithm

The regional FPAR can be expressed as

$$\begin{aligned} FPAR_{region} &= \frac{APAR}{IPAR} = \frac{\sum_{sub} FPAR_{subregion} \cdot IPAR_{subregion}}{\sum_{sub} IPAR_{subregion}} \\ &= \frac{1}{N_{sub}} \cdot \sum_{sub} FPAR_{subregion} \end{aligned} \quad (146)$$

where $FPAR_{subregion}$ is a retrieved FPAR for a subregion [either from Eq. (144), (131), or (135)] within the region and N_{sub} is the number of available subregions (that is, the number containing retrieved FPAR's) within the region. Note that at present, the default FPAR's [i.e., those for which the primary algorithm failed and regression using Eq. (131) was performed] are established only for solar zenith angles θ_0 up to 60° . For regions with $\theta_0 > 60^\circ$ (i.e., $\mu_0 < 0.5$), FPAR's that could not be determined by any of the above methods are set to a fill value indicating that no calculation was performed. The summation in Eq. (146) does not include these subregions.

For each regional FPAR an associated FPAR variability is also determined. This is defined as

$$\Delta FPAR_{region} = \left[\frac{1}{N_{sub}} \cdot \sum_{sub} [FPAR_{subregion}(\mu_0) - FPAR_{region}(\mu_0)]^2 \right]^{\frac{1}{2}} \quad (147)$$

and gives a measure of the range of variability of the FPAR's within the region.

Also computed is the mode value of the FPAR uncertainty for the individual 1.1 km subregions,

$$\delta FPAR_{region} = Mode\{\delta FPAR_{subregion}\} \quad (148)$$

where the individual $\delta FPAR_{subregion}$'s are determined either from Eq. (145), (134), or (135).

3.3.8.3 Archived algorithm output

For each 17.6 km region within which some successful subregional BRF/DHR retrievals were performed, a regional FPAR, $FPAR_{region}$, and its variability, $\Delta FPAR_{region}$, are directly archived in the Aerosol/Surface Product along with the modal value of subregion FPAR uncertainty, $\delta FPAR_{region}$. A maximum of 256 1.1-km subregions contribute to the 17.6-km regional FPAR. As part of the quality assessment of the regional FPAR, we archive the number of subregional FPAR's calculated using the LAI/FPAR retrieval algorithm and the number of subregional FPAR's calculated using the default NDVI-FPAR algorithm. Finally, we also archive the frequency of occurrence of each biome/surface type within the region from among the 10 possibilities: one of the six vegetated biomes, barren, unknown, ambiguous, and not_land.

3.4 THEORETICAL DESCRIPTION OF OCEAN SURFACE RETRIEVALS

Several processes which occur during the ocean surface retrievals are indicated in §3.1 (in particular Figure 3). In the following sections, the physical basis of these processes and a mathematical description of the algorithm which is used to implement each process is presented. Each of the following processes is performed only on those subregions which have been deemed acceptable for surface retrieval (see §3.2.1.4 and §3.2.1.5) and which fall within the tropical ocean, defined to be a 600-km wide band centered on the equator (i.e., within latitudes $\pm 2.695^\circ$).

3.4.1 Determine TOA equivalent reflectance due to sun glitter and whitecaps

3.4.1.1 Physics of the problem

The reflectance of the ocean surface is considered to arise from the contribution of three terms: (1) diffusely reflecting suspended material, (2) sun glitter, and (3) whitecaps. The first term is negligible at 672 nm and 866 nm; however, it forms the basis of ocean color algorithms at shorter wavelengths (446 nm and 558 nm for MISR). Thus, we want to retrieve the equivalent reflectance associated with this term for MISR bands 1 and 2. The second and third terms are approximately wavelength independent. The wind roughens the ocean surface, which can then be modeled as an array of facets with a distribution of slopes. A basic theory was worked out by Cox and Munk [9]. As wind speed increases, the wave slopes increase and the glitter pattern increases in angular width. The Cox-Munk model will be used to establish the magnitude of the second term for the

radiative transfer calculations. Direct observations by any camera of the glitter pattern are not used in the aerosol retrievals and are removed from the surface retrievals as well, by eliminating views within 30° of the specular reflection direction. Sun glitter therefore affects the observed radiances used in surface retrievals only as a result of scattering. Finally, the whitecap model adopted for MISR uses only wind speed as an input parameter, and is based on Monahan and O’Muircheartaigh [32] and Koepke [28].

3.4.1.2 Mathematical description of the algorithm

The bidirectional reflectance factor (BRF) of the ocean surface, R_{λ}^{ocean} at wavelength λ is the sum of three terms:

$$\begin{aligned} R_{\lambda}^{ocean}(-\mu, \mu_0, \phi - \phi_0) &= \\ &= R_{\lambda}^{water}(-\mu, \mu_0, \phi - \phi_0) + R_{\lambda}^{glitter}(-\mu, \mu_0, \phi - \phi_0) + R_{\lambda}^{whitecap}(-\mu, \mu_0, \phi - \phi_0) \end{aligned} \quad (149)$$

where R_{λ}^{water} is the BRF of the water due to diffuse scattering by suspended material and the remaining terms are due to glitter and whitecaps, respectively. In addition to depending on the view and illumination geometry, the BRF’s for glitter and whitecaps are also a function of the surface wind speed but do not depend on λ . Expressions for $R_{\lambda}^{glitter}$ and $R_{\lambda}^{whitecap}$ can be found in [M-6]. Therefore, the equivalent reflectance at the top of the atmosphere, ρ_{λ} , may be written as the sum of four terms,

$$\begin{aligned} \rho_{\lambda}(-\mu, \mu_0, \phi - \phi_0) &= \rho_{\lambda}^{atm}(-\mu, \mu_0, \phi - \phi_0) + \rho_{\lambda}^{water}(-\mu, \mu_0, \phi - \phi_0) \\ &+ \rho_{\lambda}^{glitter}(-\mu, \mu_0, \phi - \phi_0) + \rho_{\lambda}^{whitecap}(-\mu, \mu_0, \phi - \phi_0) \end{aligned} \quad (150)$$

where ρ_{λ}^{atm} is the equivalent reflectance describing the atmospheric path radiance, and the other three terms are equivalent reflectances describing the water leaving radiance, glitter radiance and whitecap radiance of the ocean surface at the top of the atmosphere. Note the dependence of $\rho_{\lambda}^{glitter}$ and $\rho_{\lambda}^{whitecap}$ on λ due to the atmospheric transmittance.

Once an aerosol retrieval has been performed, then ρ_{λ}^{atm} and the combination of $\rho_{\lambda}^{glitter} + \rho_{\lambda}^{whitecap}$ can be determined. Subtracting $\rho_{\lambda}^{glitter} + \rho_{\lambda}^{whitecap}$ from ρ_{λ} results in $\rho_{\lambda}^{atm} + \rho_{\lambda}^{water}$ which is the TOA equivalent reflectance component used as input to the conventional ocean surface retrieval algorithm. By also subtracting ρ_{λ}^{atm} from ρ_{λ} results in ρ_{λ}^{water} alone, the TOA equivalent reflectance component used as input to the experimental ocean surface retrieval algorithm. To perform these subtraction procedures, both ρ_{λ}^{atm} and $\rho_{\lambda}^{glitter} + \rho_{\lambda}^{whitecap}$ must be interpolated to the MISR view angle and solar geometries since each term is stored in the SMART Dataset on a standard Radau point grid. A three point quadratic scheme is used in the interpolation procedure.

3.4.1.3 Aerosol mixture requirements of the algorithm

The SMART Dataset contains ρ_{λ}^{atm} and a combined $\rho_{\lambda}^{glitter} + \rho_{\lambda}^{whitecap}$ for each of the pure particles composing the aerosol mixtures used during aerosol retrievals. The combined glitter and whitecap equivalent reflectance for a successful aerosol mixture candidate, using the standard linear mixing theory, can be expressed as

$$\begin{aligned} & \rho_{\lambda}^{glitter}(-\mu, \mu_0, \phi - \phi_0; \tau_{\lambda}) + \rho_{\lambda}^{whitecap}(-\mu, \mu_0, \phi - \phi_0; \tau_{\lambda}) \\ &= \sum_n f_{n\lambda} \cdot [\rho_n^{glitter}(-\mu, \mu_0, \phi - \phi_0; \tau_{\lambda}) + \rho_n^{whitecap}(-\mu, \mu_0, \phi - \phi_0; \tau_{\lambda})] \end{aligned} \quad (151)$$

where $f_{n\lambda}$ is the fractional amount of pure particle component n at wavelength λ and τ_{λ} is the mixture optical depth. If there are N_{cand} aerosol mixture candidates, then $\rho_{\lambda}^{glitter} + \rho_{\lambda}^{whitecap}$ in Eq. (151) is computed for each candidate and the results are averaged. Thus,

$$\begin{aligned} & \rho_{\lambda}^{glitter}(-\mu, \mu_0, \phi - \phi_0) + \rho_{\lambda}^{whitecap}(-\mu, \mu_0, \phi - \phi_0) \\ &= \frac{1}{N_{cand}} \cdot \sum_{m=1}^{N_{cand}} [\rho^{glitter}(-\mu, \mu_0, \phi - \phi_0; \tau_{\lambda, m}) + \rho^{whitecap}(-\mu, \mu_0, \phi - \phi_0; \tau_{\lambda, m})] \end{aligned} \quad (152)$$

where m is the candidate index.

3.4.2 Retrieve B-camera water-leaving equivalent reflectance (conventional approach)

3.4.2.1 Physics of the problem

In the conventional approach the retrieval of the water-leaving reflectances is effected by an algorithm similar to that reported by Gordon and Wang [20] for SeaWiFS. This algorithm is a prototype for MODIS, and has been described in full detail by Gordon [19].

Prior to applying the conventional ocean retrieval algorithm, the sum of the glitter and whitecap contributions to the TOA radiance field are determined, using the aerosol models obtained from the MISR aerosol retrievals and the SMART Dataset. These contributions are subtracted from the MISR B-camera observations in bands 3 and 4 (red and near-IR), to obtain an estimate of the path radiance. The particular B-camera chosen is the one which is contaminated least by glitter and whitecaps. At these wavelengths, the water-leaving reflectance is assumed to be zero, a valid assumption except in waters with high chlorophyll concentrations, e.g., $> 0.7 - 1.0 \text{ mg m}^{-3}$, or possibly intense open-ocean coccolithophore blooms [3]. Following this glitter and whitecap correction, the contribution to the path radiance due to molecular (Rayleigh) scattering by the atmosphere,

which depends only on wavelength and atmospheric pressure, is then subtracted. The remainder is used to choose two aerosol models from a set of candidate models contained in the Tropical Ocean Aerosol Climatology (TOAC) Dataset. Note that this part of the algorithm may choose different aerosol models than obtained in the MISR aerosol retrieval; however, the MISR-retrieved aerosol is only used for the glitter and whitecap correction, which involves small terms. The candidate models in the TOAC Dataset are based upon those proposed by Shettle and Fenn [41]. The models chosen in this manner are then used to predict the aerosol contribution to the radiance in MISR bands 1 and 2 (blue and green) which, when combined with the molecular scattering component, yields the desired TOA water-leaving equivalent reflectance. This is then corrected for the effects of the atmospheric transmittance to obtain the atmospherically corrected water-leaving equivalent reflectance.

The algorithm as applied to MODIS and SeaWiFS utilizes 765 nm and 865 nm in the same manner that 672 and 866 nm (bands 3 and 4) are used with MISR. The advantage that the other instruments have over MISR for ocean retrievals is that water-leaving radiance at 765 nm can be taken to be zero at much higher chlorophyll concentrations than at 672 nm. With the exception of the method used to correct for glitter and whitecaps, the MISR algorithm is identical to the MODIS/SeaWiFS algorithm.

3.4.2.2 Mathematical description of the algorithm

As described in detail in [19], the algorithm utilizes a set of precomputed look-up tables which provide the aerosol contribution to the atmospheric path radiance, including the effects of multiple scattering. Specifically the tables provide the aerosol contribution as a function of the aerosol optical thickness, the viewing zenith and azimuth angles and the solar zenith and azimuth angles for each candidate aerosol model. In the MISR implementation, these look-up tables are incorporated in the TOAC Dataset and are used to determine the atmospherically corrected B-camera water-leaving equivalent reflectance, $\rho_{surf, \lambda}^{water}$.

The methodology to choose which B camera is most glitter-free is as follows. Define a local right-handed Cartesian coordinate system in which the +z-axis is co-aligned with the normal to the Earth's ellipsoid and points toward the center of the Earth, the x-axis is aligned with a great circle and points toward the geographic north pole, and the y-axis is orthogonal to both of these (i.e., points East). Let \hat{s} be the unit vector pointing in the direction of the Sun's rays, in which θ_0 is the solar zenith angle (relative to the z-axis) and ϕ_0 is the solar azimuth angle (relative to the x-axis). Then, the vector which describes the specular reflection direction, \hat{r} , has polar angles $180^\circ - \theta_0$ and ϕ_0 . Let the view vector \hat{v} point in the direction of photon travel, with an elevation angle θ relative to the z-axis and azimuth angle ϕ . Let $\mu_0 = \cos\theta_0$ and $\mu = \cos(180^\circ - \theta) = -\cos\theta$. The cone angle between the specular direction and the view direction, ξ , is given by:

$$\cos \xi = \hat{r} \cdot \hat{v} = \mu \mu_0 + (1 - \mu^2)^{\frac{1}{2}} (1 - \mu_0^2)^{\frac{1}{2}} \cos(\phi - \phi_0) \quad (153)$$

The most glitter-free B camera is the one with the larger value of ξ .

3.4.2.3 Aerosol mixture requirements of the algorithm

The equivalent reflectance of the glitter and whitecap radiance components for the retrieved aerosol mixtures, $\rho_{\lambda}^{glitter} + \rho_{\lambda}^{whitecap}$, is described by Eq. (152).

3.4.2.4 Archived algorithm output

For those 1.1 km subregions where an ocean surface retrieval is performed, TOAC aerosol model parameters are determined and an atmospherically corrected water-leaving equivalent reflectance, $\rho_{surf, \lambda}^{water}$, for the B-camera view contaminated least by glitter and whitecaps is determined for MISR bands 1 and 2 (blue and green wavelengths). There are two required model identifiers. Additionally, the aerosol optical depth at 866 nm gives a measure of the confidence in the atmospheric correction. These parameters are directly archived in the Aerosol/Surface Product.

3.4.3 Retrieve B-camera water-leaving equivalent reflectance (experimental approach)

3.4.3.1 Physics of the problem

The experimental approach algorithm differs from the conventional approach algorithm in that the aerosol models, retrieved using all available MISR views, are used to provide not only the glitter and whitecap terms, but an estimate of the atmospheric path radiance as well. Therefore, these TOA radiance components can be subtracted from the observed radiance, resulting in the term describing the TOA water-leaving radiance. Converting this to a radiance at the ocean surface requires a correction for the upward atmospheric transmittance, a simple procedure when the approximation of a lambertian ocean reflectance for diffuse transmittance is invoked. Since the water-leaving radiance is assumed to be zero in MISR bands 3 and 4 (red and near-IR), it is computed only in MISR bands 1 and 2 (blue and green) and only for the B-camera view least contaminated by glitter and whitecaps.

3.4.3.2 Mathematical description of the algorithm

The aerosol retrieval provides a determination of the equivalent reflectances for the atmospheric path radiance, ρ_{λ}^{atm} , and the radiance contributions due to glitter and whitecaps, $\rho_{\lambda}^{glitter} + \rho_{\lambda}^{whitecap}$. Using Eq. (150), the equivalent reflectance of the TOA water-leaving radiance, ρ_{λ}^{water} , can be easily obtained from the observed (corrected for ozone absorption) equivalent reflectance ρ_{λ} . We have

$$\begin{aligned} \rho_{\lambda}^{water}(-\mu, \mu_0, \phi - \phi_0) = & \rho_{\lambda}(-\mu, \mu_0, \phi - \phi_0) - \rho_{\lambda}^{atm}(-\mu, \mu_0, \phi - \phi_0) \\ & - \rho_{\lambda}^{glitter}(-\mu, \mu_0, \phi - \phi_0) - \rho_{\lambda}^{whitecap}(-\mu, \mu_0, \phi - \phi_0) \end{aligned} \quad (154)$$

Now, ρ_{λ}^{water} , can be expressed in terms of the equivalent reflectance of the water-leaving radiance at the ocean surface, $\rho_{surf, \lambda}^{water}$, as

$$\begin{aligned} \rho_{\lambda}^{water}(-\mu, \mu_0, \phi - \phi_0) = & e^{-\tau_{\lambda}/\mu} \cdot \rho_{surf, \lambda}^{water}(-\mu, \mu_0, \phi - \phi_0) \\ & + \int_0^1 \int_0^{2\pi} T_{\lambda}(-\mu, -\mu', \phi - \phi') \rho_{surf, \lambda}^{water}(-\mu', \mu_0, \phi' - \phi_0) d\mu' d\phi' \end{aligned} \quad (155)$$

a modified form of Eq. (17). Approximating $\rho_{surf, \lambda}^{water}$ in the integral as a lambertian reflectance and therefore removing it from the integral,

$$\rho_{\lambda}^{water}(-\mu, \mu_0, \phi - \phi_0) \approx [e^{-\tau_{\lambda}/\mu} + t_{\lambda}(-\mu)] \cdot \rho_{surf, \lambda}^{water}(-\mu, \mu_0, \phi - \phi_0) \quad (156)$$

where t_{λ} is described by Eq. (19). The equivalent reflectance for water-leaving radiance, $\rho_{surf, \lambda}^{water}$, can then be written as

$$\rho_{surf, \lambda}^{water}(-\mu, \mu_0, \phi - \phi_0) = \frac{\rho_{\lambda}^{water}(-\mu, \mu_0, \phi - \phi_0)}{[e^{-\tau_{\lambda}/\mu} + t_{\lambda}(-\mu)]} \quad (157)$$

where t must be interpolated to the B camera specific value of μ since this atmospheric parameter is stored in the SMART Dataset at view angle cosines, defined on the standard Radau point grid. This is accomplished using a three point quadratic interpolation scheme.

3.4.3.3 Aerosol mixture requirements of the algorithm

There are four atmospheric parameters used in the algorithm that depend on the retrieved aerosol mixture models. These are the equivalent reflectance of the atmospheric path radiance, ρ_{λ}^{atm} , the combined glitter and whitecap equivalent reflectance, $\rho_{\lambda}^{glitter} + \rho_{\lambda}^{whitecap}$, the atmospheric optical depth, τ_{λ} , and the angle-integrated upward diffuse transmittance, t_{λ} . The parameters τ_{λ} , and ρ_{λ}^{atm} are described by Eq. (47) and $\rho_{\lambda}^{glitter} + \rho_{\lambda}^{whitecap}$ is described by Eq. (152). The SMART Dataset contains t_{λ} for each of the pure particles composing the aerosol mixtures. The angle-integrated upward diffuse transmittance for each successful aerosol mixture candidate, using the modified linear mixing theory, is expressed as

$$\begin{aligned}
t(-\mu; \tau_\lambda) = & t_{R,ms}(-\mu; \tau_{R,\lambda}) + \sum_n f_n \cdot t_{n,ss}(-\mu; \tau_\lambda) \\
& + \sum_n f_n \cdot \frac{\bar{\omega}_{mix,\lambda}}{\bar{\omega}_{n\lambda}} \cdot e^{-\tau_\lambda |\bar{\omega}_{mix,\lambda} - \bar{\omega}_{n\lambda}|} \cdot [t_{n,ms}(-\mu; \tau_\lambda) - t_{R,ms}(-\mu; \tau_{R,\lambda})]
\end{aligned} \tag{158}$$

where $f_{n\lambda}$ is the fractional amount of pure particle component n at wavelength λ and τ_λ is the mixture optical depth. If there are N_{cand} successful aerosol mixture candidates, then t in Eq. (158) is computed for each candidate and the results are averaged. Thus,

$$t_\lambda(-\mu) = \frac{1}{N_{cand}} \cdot \sum_{m=1}^{N_{cand}} t(-\mu; \tau_{\lambda,m}) \tag{159}$$

where m is the candidate index.

3.4.3.4 Best estimate of water-leaving equivalent reflectance and its uncertainty

If there are N_{cand} acceptable aerosol mixture candidate models as determined from the aerosol retrieval, the best estimate of the water-leaving equivalent reflectance, $\rho_{surf,\lambda}^{water}$, is defined by Eq. (157), where all atmosphere-dependent parameters are assumed to be averages of the N_{cand} individual candidate models. Thus, $\rho_\lambda^{glitter} + \rho_\lambda^{whitecap}$ in Eq. (154) is given by Eq. (152) and the other averaged parameters in Eqs. (154) and (157), ρ_λ^{atm} , τ_λ , and t_λ , are described in Eq. (47). Now, using Eqs. (154) and (157), $\rho_{surf,\lambda}^{water}$ can be expressed in terms of the measured equivalent reflectances, ρ_λ , as

$$\rho_{surf,\lambda}^{water}(-\mu, \mu_0, \phi - \phi_0) = g_\lambda(-\mu) \cdot \rho_\lambda(-\mu, \mu_0, \phi - \phi_0) - w_\lambda(-\mu, \mu_0, \phi - \phi_0) \tag{160}$$

where g_λ is given by Eq. (57) and w_λ is defined as

$$\begin{aligned}
w_\lambda(-\mu, \mu_0, \phi - \phi_0) = & g_\lambda(-\mu) \cdot [\rho_\lambda^{atm}(-\mu, \mu_0, \phi - \phi_0) \\
& + \rho_\lambda^{glitter}(-\mu, \mu_0, \phi - \phi_0) + \rho_\lambda^{whitecap}(-\mu, \mu_0, \phi - \phi_0)]
\end{aligned} \tag{161}$$

Thus, the variance of $\rho_{surf,\lambda}^{water}$ can be written as

$$\begin{aligned}
(\Delta \rho_{surf, \lambda}^{water})^2(-\mu, \mu_0, \phi - \phi_0) &= g_{\lambda}^2(-\mu) \cdot \sigma_{\rho_{\lambda}}^2(-\mu, \mu_0, \phi - \phi_0) \\
&\quad + \rho_{\lambda}^2(-\mu, \mu_0, \phi - \phi_0) \cdot \sigma_{g_{\lambda}}^2(-\mu) + \sigma_{w_{\lambda}}^2(-\mu, \mu_0, \phi - \phi_0) \\
&\quad - 2 \cdot \rho_{\lambda}(-\mu, \mu_0, \phi - \phi_0) \cdot \sigma_{g_{\lambda} w_{\lambda}}^2(-\mu, \mu_0, \phi - \phi_0)
\end{aligned} \tag{162}$$

where $\sigma_{\rho_{\lambda}}^2$, $\sigma_{g_{\lambda}}^2$, and $\sigma_{w_{\lambda}}^2$ are variances of ρ_{λ} , g_{λ} , and w_{λ} , respectively, and $\sigma_{g_{\lambda} w_{\lambda}}^2$ is the covariance of g_{λ} and w_{λ} . An estimate of $\sigma_{\rho_{\lambda}}^2$ is given in Eq. (51) and estimates of the other variances and the covariance can be written as

$$\begin{aligned}
\sigma_{g_{\lambda}}^2(-\mu) &= \frac{1}{N_{cand}} \cdot \sum_{m=1}^{N_{cand}} [g(-\mu; \tau_{\lambda, m}) - g_{\lambda}(-\mu)]^2 \\
\sigma_{w_{\lambda}}^2(-\mu, \mu_0, \phi - \phi_0) &= \frac{1}{N_{cand}} \cdot \sum_{m=1}^{N_{cand}} [w(-\mu, \mu_0, \phi - \phi_0; \tau_{\lambda, m}) - w_{\lambda}(-\mu, \mu_0, \phi - \phi_0)]^2 \\
\sigma_{g_{\lambda} w_{\lambda}}^2(-\mu, \mu_0, \phi - \phi_0) &= \\
&\quad \frac{1}{N_{cand}} \cdot \sum_{m=1}^{N_{cand}} [w(-\mu, \mu_0, \phi - \phi_0; \tau_{\lambda, m}) - w_{\lambda}(-\mu, \mu_0, \phi - \phi_0)] \cdot [g(-\mu; \tau_{\lambda, m}) - g_{\lambda}(-\mu)]
\end{aligned} \tag{163}$$

where the model-dependent g is given by Eq. (60) and the model-dependent w is expressed as

$$\begin{aligned}
w(-\mu, \mu_0, \phi - \phi_0; \tau_{\lambda, m}) &= g(-\mu; \tau_{\lambda, m}) \cdot [\rho^{atm}(-\mu, \mu_0, \phi - \phi_0; \tau_{\lambda, m}) \\
&\quad + \rho^{glitter}(-\mu, \mu_0, \phi - \phi_0; \tau_{\lambda, m}) + \rho^{whitecap}(-\mu, \mu_0, \phi - \phi_0; \tau_{\lambda, m})]
\end{aligned} \tag{164}$$

3.4.3.5 Archived algorithm output

Like the conventional algorithm, the use of the experimental algorithm for the B-camera equivalent reflectance is restricted to the tropical ocean. For those 1.1 km subregions where an ocean surface retrieval is performed, the equivalent reflectance of the water-leaving radiance, $\rho_{surf, \lambda}^{water}$, and its uncertainty, $\Delta \rho_{surf, \lambda}^{water}$, are determined for MISR bands 1 and 2 (blue and green wavelengths) and for the B-camera view contaminated least by glitter and whitecaps, and are directly archived in the Aerosol/Surface Product.

3.4.4 Retrieve phytoplankton pigment concentration

3.4.4.1 Physics of the problem

The phytoplankton pigment concentration C of water is the sum of the concentrations of chlorophyll a and phaeophytin a . Gordon et al. [17] have shown that for the pigment range $0 \leq C \leq 1 \text{ mg/m}^3$, i.e., waters for which the optical properties are dominated by phytoplankton and their immediate detrital material, the ratio of the atmospherically corrected water-leaving radiances in bands 1 and 3 (443 and 550 nm) of the Coastal Zone Color Scanner (CZCS) can be used to estimate C . These CZCS bands are almost identical, both center wavelength and width, to the MISR bands 1 and 2 (blue and green) and thus the CZCS algorithm can also be used to estimate C from the MISR-determined, atmospherically corrected water-leaving equivalent reflectances in these bands. For pigment concentrations greater than 1 mg m^{-3} , which occur near the coast and at times during blooms in the open ocean, the water-leaving radiance in the blue band becomes vanishingly small, and the algorithm may not be valid. As a minimum check, we require that the atmospherically corrected water-leaving radiances in bands 1 and 2 are both positive before calculating C .

3.4.4.2 Mathematical description of the algorithm

The phytoplankton pigment concentration, C , is estimated from the empirical expression,

$$C = \alpha \left[\frac{L_{surf,2}^{water}(-\mu, \mu_0, \phi - \phi_0)}{L_{surf,1}^{water}(-\mu, \mu_0, \phi - \phi_0)} \right]^\beta \quad (165)$$

where $L_{surf,1}^{water}$ and $L_{surf,2}^{water}$ are the atmospherically corrected water-leaving radiances in bands 1 and 2, respectively, and where α and β take on values of 1.12 and 1.7, respectively. Converting radiance to equivalent reflectance via Eq. (30) and denoting the selected camera geometry by a subscript B,

$$C = \alpha \left[\frac{\mathcal{E}_{0,2}^{std, in-band} \cdot \rho_{surf,2}^{water}(-\mu_B, \mu_0, \phi_B - \phi_0)}{\mathcal{E}_{0,1}^{std, in-band} \cdot \rho_{surf,1}^{water}(-\mu_B, \mu_0, \phi_B - \phi_0)} \right]^\beta \quad (166)$$

where $\rho_{surf,1}^{water}$ and $\rho_{surf,2}^{water}$ are the corresponding equivalent reflectances for the selected B camera; $\mathcal{E}_{0,1}^{std, in-band}$ and $\mathcal{E}_{0,2}^{std, in-band}$ are the standardized, in-band weighted solar irradiances in bands 1 and 2, obtained from the ARP. The reason that in-band values are used is that a correction for out-of-band response is planned prior to aerosol and surface retrievals (see [M-5]). However, we note that initial versions of the data processing software will not include this correction. In this case, $\mathcal{E}_{0,1}^{std}$ and $\mathcal{E}_{0,2}^{std}$, solar irradiances weighted by the total band response, are used in Eq. (166). C is expressed in units of mg m^{-3} .

3.4.5 Estimated uncertainty of C

Using the expression for C in Eq. (166), we can write the variance of C as

$$\begin{aligned}
 (\Delta C)^2 = & \left[\frac{\beta C}{\rho_{surf,2}^{water}(-\mu_B, \mu_0, \phi_B - \phi_0)} \right]^2 \cdot (\Delta \rho_{surf,1}^{water})^2(-\mu_B, \mu_0, \phi_B - \phi_0) \\
 & + \left[\frac{\beta C}{\rho_{surf,1}^{water}(-\mu_B, \mu_0, \phi_B - \phi_0)} \right]^2 \cdot (\Delta \rho_{surf,2}^{water})^2(-\mu_B, \mu_0, \phi_B - \phi_0) \\
 & - 2 \left[\frac{\beta^2 C^2}{\rho_{surf,1}^{water}(-\mu_B, \mu_0, \phi_B - \phi_0) \cdot \rho_{surf,2}^{water}(-\mu_B, \mu_0, \phi_B - \phi_0)} \right] \cdot \sigma_{\rho_1 \rho_2}^2(-\mu_B, \mu_0, \phi_B - \phi_0)
 \end{aligned} \tag{167}$$

where $(\Delta \rho_{surf,1}^{water})^2$ and $(\Delta \rho_{surf,2}^{water})^2$ are uncertainties in $\rho_{surf,1}^{water}$ and $\rho_{surf,2}^{water}$, respectively and $\sigma_{\rho_1 \rho_2}^2$ is their covariance. Estimates of these variances for the equivalent reflectances using the experimental algorithm are given by Eq. (162) and the covariance is expressed as

$$\begin{aligned}
 \sigma_{\rho_1 \rho_2}^2 = & \frac{1}{N_{cand}} \cdot \sum_{m=1}^{N_{cand}} [\rho_{surf}^{water}(-\mu_B, \mu_0, \phi_B - \phi_0; \tau_{1,m}) - \rho_{surf,1}^{water}(-\mu_B, \mu_0, \phi_B - \phi_0)] \\
 & \cdot [\rho_{surf}^{water}(-\mu_B, \mu_0, \phi_B - \phi_0; \tau_{2,m}) - \rho_{surf,2}^{water}(-\mu_B, \mu_0, \phi_B - \phi_0)]
 \end{aligned} \tag{168}$$

where ρ_{surf}^{water} is the model-dependent form of Eq. (157), i.e.,

$$\begin{aligned}
 \rho_{surf}^{water}(-\mu_B, \mu_0, \phi_B - \phi_0; \tau_{\lambda,m}) &= \frac{\rho^{water}(-\mu, \mu_0, \phi - \phi_0; \tau_{\lambda,m})}{[e^{-\tau_{\lambda,m}/\mu} + t(-\mu; \tau_{\lambda,m})]} \\
 \rho^{water}(-\mu, \mu_0, \phi - \phi_0; \tau_{\lambda,m}) &= \rho_{\lambda}(-\mu, \mu_0, \phi - \phi_0) - \rho^{atm}(-\mu, \mu_0, \phi - \phi_0; \tau_{\lambda,m}) \\
 &\quad - \rho^{glitter}(-\mu, \mu_0, \phi - \phi_0; \tau_{\lambda,m}) - \rho^{whitecap}(-\mu, \mu_0, \phi - \phi_0; \tau_{\lambda,m})
 \end{aligned} \tag{169}$$

There is a natural variability δC in the relationship described by Eq. (165) of $\approx 0.38C$ [18]. Therefore, the total variance of C , $(\Delta C)_{tot}^2$, can be expressed as,

$$(\Delta C)_{tot}^2 = (\Delta C)^2 + 0.14C^2 \tag{170}$$

3.4.5.1 Archived algorithm output

Since this algorithm requires the B-camera equivalent reflectances $\rho_{surf,1}^{water}$ and $\rho_{surf,2}^{water}$ as input, its use is restricted to the tropical ocean. For those 1.1 km subregions where $\rho_{surf,1}^{water}$ and $\rho_{surf,2}^{water}$ are available, the phytoplankton pigment concentration, C , is computed using the equivalent reflectances from both the conventional and experimental algorithms, and the uncertainty, $(\Delta C)_{tot}$, using the experimental algorithm, are directly archived in the Aerosol/Surface Product.

3.5 ALGORITHM SENSITIVITY STUDIES

3.5.1 HDRF and BHR land retrievals

Uncertainty estimates for the retrieved land surface HDRF's and BHR's were ascertained by performing retrieval studies on simulated MISR datasets, constructed using realistic surface BRDFs and atmospheric aerosol models. The surface BRDFs were derived from field measurements ([24], [25], [26]) for various surface types ranging from bare soil (strong backward scattering) to forest canopies (moderate backward and forward scattering). The 11 types used in the retrieval uncertainty study are listed in Table 5.

Table 5: Surface type characteristics

Case	Surface Type	BHR (670 nm)
1	Soil	0.186
2	Grassland	0.318
3	Steppe grass	0.211
4	Hard wheat	0.228
5	Irrigated wheat	0.0633
6	Hardwood forest	0.0350
7	Pine forest	0.0376
8	Lawn grass	0.0578
9	Corn	0.0817
10	Soybeans	0.0344
11	Orchard grass	0.0774

The simulated MISR datasets consist of computed TOA radiances at a wavelength of 670 nm and the nine MISR view angles for each of the 11 different surface types, assuming a sulfate aerosol (accumulation mode) in the troposphere with an optical depth of 0.4 and a Rayleigh (molecular) scattering optical depth of 0.043. The solar zenith angle was taken to be 46° and the azimuth angle

defining the MISR observation plane assumed three different values, 30°, 60° and 90° as measured from the principal plane. The multiple scattering radiative transfer computations for this coupled atmosphere-surface problem were accomplished using a matrix operator technique [21] in which all orders of interaction between the surface and the atmosphere were taken into account.

The surface algorithm, as described in §3.3.3, was used on the simulated MISR datasets to retrieve both the HDRF at the nine MISR view angles and the associated BHR for each of the 11 surface types. It is expected that the accuracy of the surface algorithm would depend on how well the atmospheric properties were known, so three retrieval scenarios were studied in which the aerosol properties were varied. The first scenario assumed the same atmospheric properties as those used in generating the simulated MISR datasets (i.e., the correct aerosol model and optical depth was used in the surface algorithm). With no uncertainty in the atmospheric properties any errors in the surface retrieval products come only from the mechanics of performing the actual retrieval. The other two retrieval scenarios varied the properties of the aerosol, one assuming that the correct aerosol model is used but with a modified optical depth of 0.35 instead of 0.4 and the other assuming the correct optical depth of 0.4 but using a highly hydrated form (99% relative humidity) of the correct aerosol model.

The error in the retrieval of the HDRF is described by a parameter δ called the deviation, defined by

$$\delta = \frac{1}{9} \cdot \sum_{ij} |r(\mu_i, \mu_0, \phi_j - \phi_0) - r_0(\mu_i, \mu_0, \phi_j - \phi_0)| \quad (171)$$

where r and r_0 are the retrieved and true HDRF's, respectively. Figure 5 shows the HDRF deviations for the 11 surface types and the three azimuth view angle geometries for the scenario of a correct atmospheric model. Note that for all cases the deviation is under 0.005. The largest deviations occurred for those surface types with the highest BHR values (cases 1 through 4; see Table 4), and are substantially smaller for the other types (less than 0.0025). In Figure 6, where the aerosol optical depth is reduced by 0.05 from the correct value, the deviations are typically between 0.010 and 0.015 for the surface cases with low BHR values (cases 5 through 11) and slightly smaller deviations for the surface cases with higher BHR values. The same case-dependent trend is seen in Figure 7 where the hydrated aerosol model is used but the deviations for all cases are now somewhat larger. The corresponding BHR errors, defined as the true BHR minus the retrieved BHR, are shown in Figures 8, 9, and 10. In Figure 8, in which the correct atmospheric model was used, those surface types with the largest BHR values also show the largest errors (about -0.009) occurring for the view geometry azimuth angle of 90°, i.e., observations perpendicular to the principal plane. The results of the aerosol model with the reduced optical depth, displayed in Figure 9, show a general positive bias error of about 0.007 with errors generally smaller for those surface cases with the highest BHR values. The same trend is seen in Figure 10 for the hydrated aerosol

model but with a larger positive bias error of about 0.012.

This preliminary study indicates that the largest source of error in the surface retrieval is due mainly to the uncertainties associated with the atmospheric properties (i.e., aerosol type and optical depth). The nominal aerosol optical depth of 0.4 used in this study is generally larger than the typical optical depths found globally. For smaller optical depths the errors in retrieved HDRF's and BHR's, as displayed in Figures 5 - 10, will diminish accordingly. Users with the most stringent accuracy requirements are advised to limit the data to situations with low aerosol optical depth.

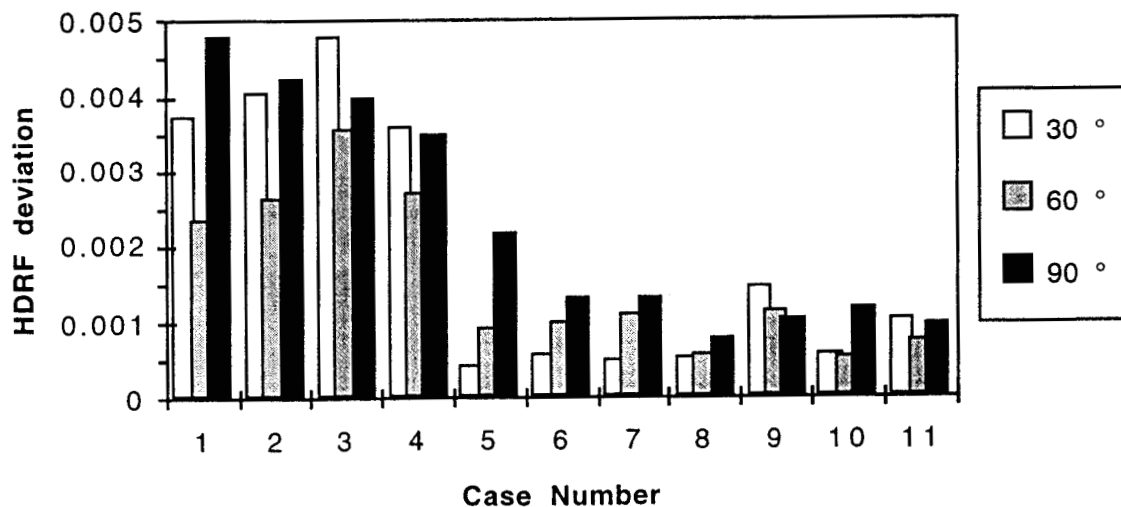


Figure 5. HDRF retrieval errors with correct atmospheric model

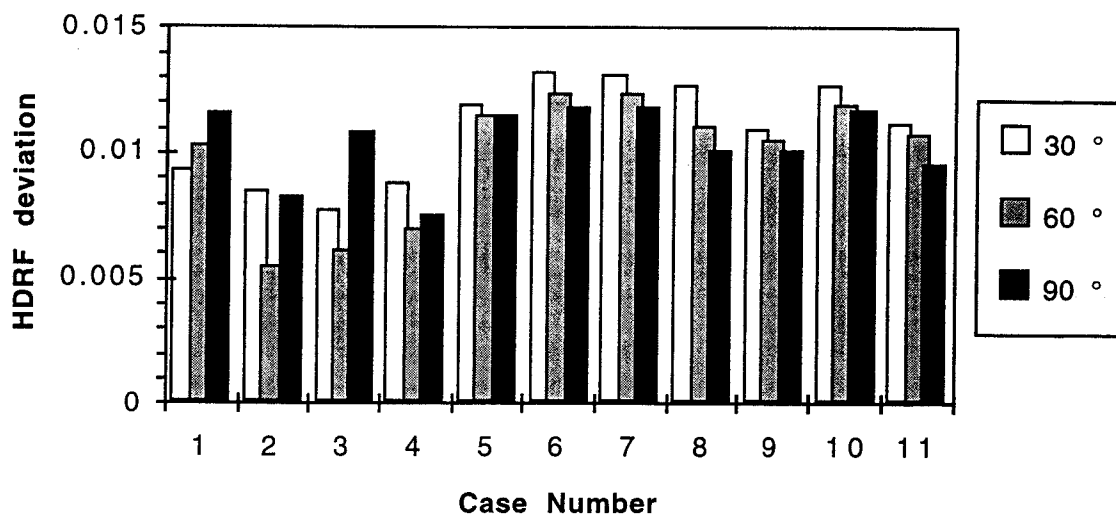


Figure 6. HDRF retrieval errors with atmospheric optical depth reduced by 0.05

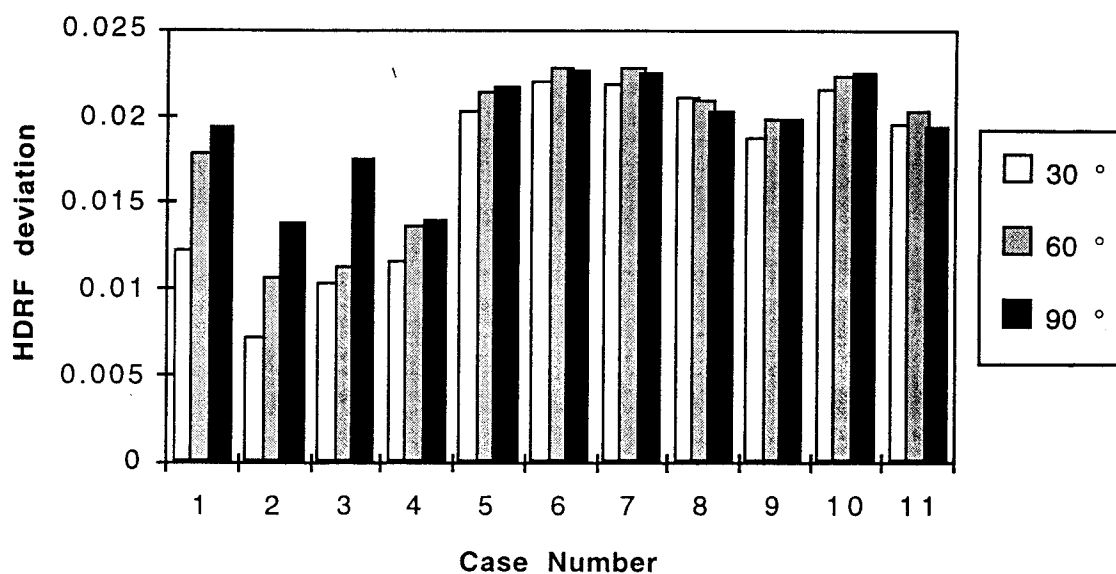


Figure 7. HDRF retrieval errors with hydrated aerosol model

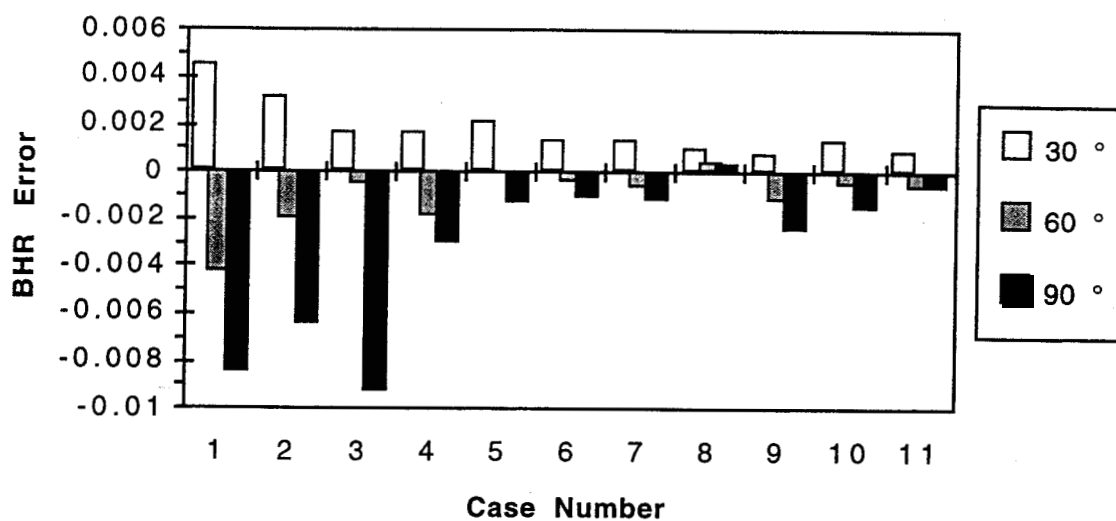


Figure 8. BHR retrieval errors with correct atmospheric model

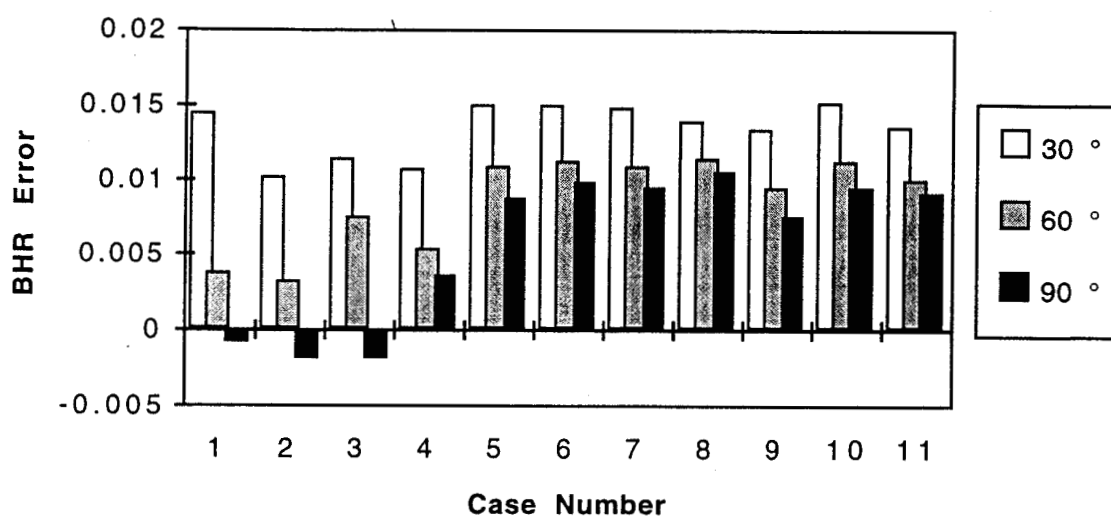


Figure 9. BHR retrieval errors with atmospheric optical depth reduced by 0.05

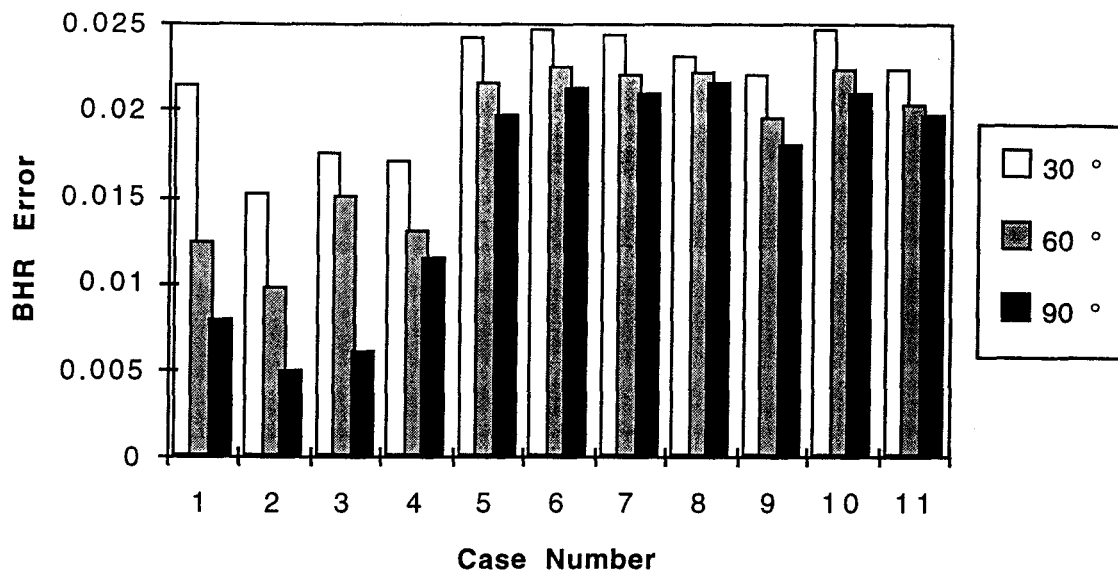


Figure 10. BHR retrieval errors with hydrated aerosol model

3.5.2 NDVI-FPAR relationship

Standard canopies (the base cases) of the six biome classes described in §3.3.6 can be defined in terms of canopy model parameter values considered typical from a remote sensing point of view. Table 6 lists the parameter types and associated values for each biome class. Leaf water content in all cases was 0.025 m and leaf optical properties were simulated with the PROSPECT model [23]. For savanna, leaf forests, and needle forests fractional ground cover refers to the overstory, a range of LAI (0 - 3) was also considered for their understory, and the two leaf normal orientations in these biomes refer to over-and understory. The trunk, stem and branch fractions are fraction of the canopy LAI and their optical properties are averages of those reported for boreal canopies.

Table 6: Biome Model Parameters

Parameter	Grasses/ Cereal Crops	Shrublands	Broadleaf Crops	Savanna	Leaf Forests	Needle Forests
Plant LAI	0 - 7	0 - 7	0 - 7	0 - 7	0 - 7	0 - 7
Fractional Ground Cover	1.0	0.2 - 0.6	0.1 - 1.0	0.2 - 0.4	> 0.8	> 0.7
Understory LAI	n/a	n/a	n/a	0 - 5	0 - 2	0 - 2

Table 6: Biome Model Parameters

Parameter	Grasses/ Cereal Crops	Shrublands	Broadleaf Crops	Savanna	Leaf Forests	Needle Forests
Leaf Normal Orientation	erectophile	uniform	uniform	uniform/ erectophile	uniform/ planophile	uniform/ planophile
Stems, Trunks & Branches	n/a	5%	10%	10%	15 - 20%	15 - 20%
Leaf Size (m)	0.05	0.05	0.10	n/a	n/a	n/a
Crown Size (m)	n/a	n/a	n/a	4x2 8x4	6x4 12x8	4x2 8x4
Leaf Chlorophyll ($\mu\text{g}/\text{m}^2$)	20 - 40	20 - 40	20 - 40	20 - 40	20 - 40	20 - 40
Soil Properties c = clay, s = sand	60c+40s medium	80s+20c bright	80c+20s dark	60c+40s medium	60c+40s medium	60c+40s medium
Solar Zenith Angle (deg)	10 - 60	10 - 60	10 - 60	10 - 60	10 - 60	10 - 60

Based on this modeling, spectral reflectances in the red and near IR and PAR absorptance were computed using the canopy radiative transfer model to simulate NDVI-FPAR relationships. These are shown in Figure 11. In this figure, the notation “Bn” refers to Biome n, where n = 1 (cereal crops or grasses), n = 2 (shrublands), n = 3 (broadleaf crops), n = 4 (savannas), n = 5 (broadleaf forests), and n = 6 (coniferous forests). The abbreviation “ulai” refers to understory leaf area index.

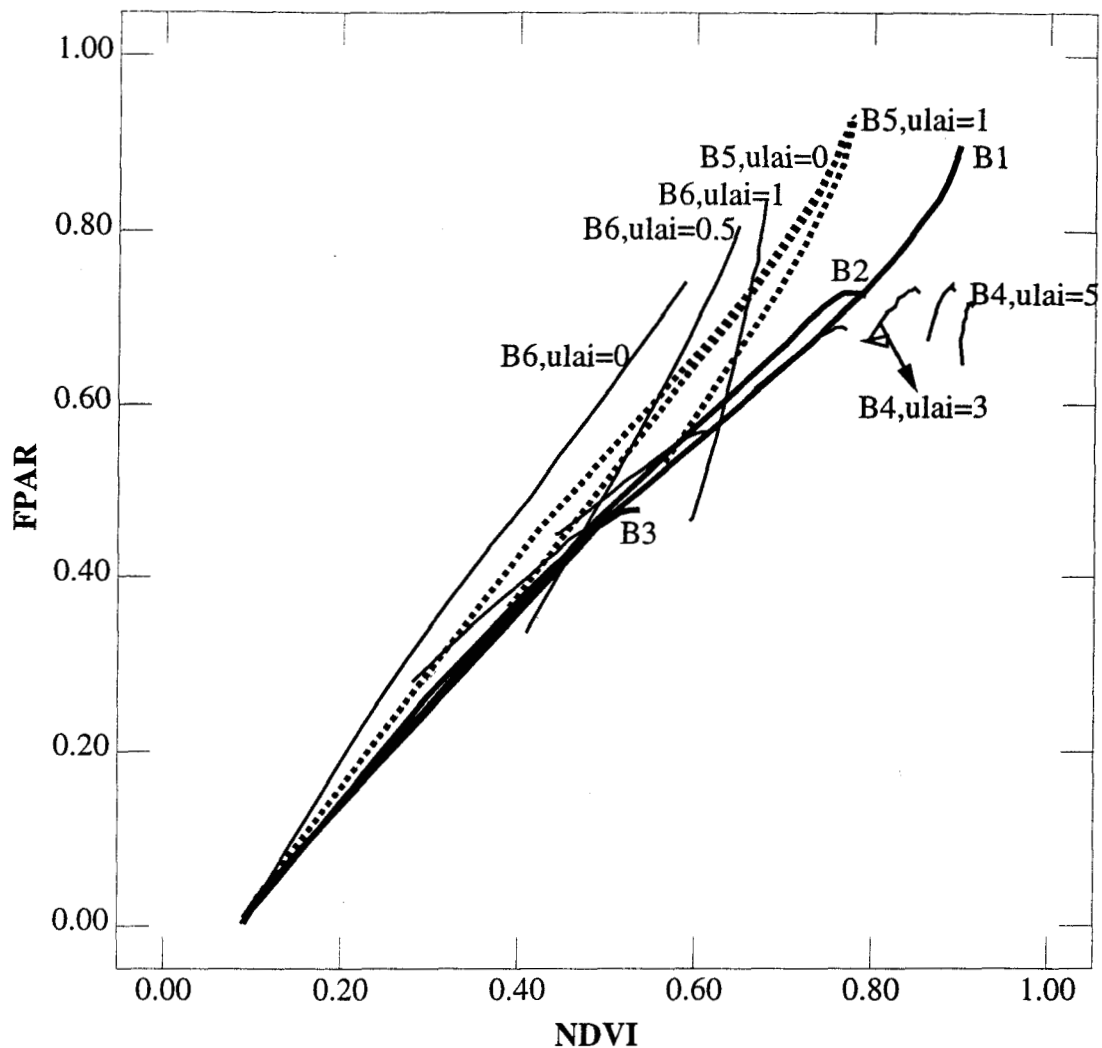


Figure 11. Relationships between FPAR and at-surface NDVI in the base case simulation

A sensitivity analysis was performed by changing the base case parameter values of each biome type, one at a time, to the end points of the parameter ranges typically found in practice. For example, the leaf normal orientation of leaf forests in the base case simulation was uniform. The sensitivity to leaf orientation for this biome type was investigated by changing the leaf normal orientation to planophile (mostly horizontal leaves) and repeating all the calculations that were performed in the base case simulation. Another set of calculations was then performed with erectophile leaf normal orientation (leaves mostly vertical). In this fashion the NDVI-FPAR relationships are repeatedly simulated for various scenarios to investigate the sensitivity to ground cover, understory LAI, leaf normal orientation, woody material fraction, leaf and crown sizes, leaf chlorophyll content, soil reflectance and solar zenith angle. Table 7 depicts the variations in nadir NDVI for typical changes in the canopy radiative transfer model parameters and solar zenith angle. Since

NDVI-FPAR relationships are nearly linear, the error in the estimation of FPAR because of uncertainty in the canopy parameters is of the same order of magnitude as for NDVI. We see that large variations in NDVI (and FPAR) can occur (~ 0.1) if the ground cover is not precisely known. Similar errors occur in the shrublands biome if the soil reflectance is incorrectly specified. These variation estimates are valid for canopies at seasonal maximum greenness.

Table 7: NDVI Sensitivity to Biome Parameters

Parameter	Grasses/ Cereal Crops	Shrublands	Broadleaf Crops	Savanna	Leaf Forests	Needle Forests
Base Case NDVI	0.81	0.42	0.72	0.58	0.77	0.74
Fractional Ground Cover	n/a	-0.07@0.4 0.07@0.6	-0.17@0.6 0.13@1.0	-0.07@0.1 0.12@0.4	-0.01@0.6 n/a	-0.03@0.6 0.03@1.0
Planophile	0.04	0.06	0.04	0.03	0.03	0.03
Uniform	0.01	n/a	n/a	n/a	n/a	n/a
Erectophile	n/a	-0.02	-0.02	-0.01	-0.01	-0.01
Gap Radius (10% change)	-0.01	-0.01	-0.01	-0.04	-0.07	-0.08
Woody Material Fraction (10 - 40%)	n/a	0.01 - 0.03	n/a	0.01 - 0.04	0.02 - 0.06	0.04 - 0.06
Leaf Chlorophyll (40 $\mu\text{g}/\text{m}^2$)	0.04	0.02	0.04	0.03	0.04	0.04
Bright Soil	-0.01	n/a	-0.04	-0.03	-0.01	-0.02
Medium Soil	n/a	0.04	n/a	n/a	n/a	n/a
Dark Soil	0.02	0.13	0.05	0.06	0.01	0.03
Solar Zenith Angle (15 - 60 deg)	-0.01	-0.04	-0.07	-0.06	-0.01	-0.03

The fact that terrain varies in elevation has direct consequences for the accuracy of the FPAR algorithm in that atmospheric functions such as path radiance, diffuse transmittance, etc. are dependent on the terrain height. In particular, terrain height effects may produce a possible deterioration of surface classification accuracy because NDVI become more sensitive to terrain height with increasing turbidity [44]. For MISR the average elevation of each 1.1 km area will be known to < 100 m and the elevation-dependent atmospheric effects taken into account when retrieving DHR. Thus, the uncertainty in NDVI due to elevation uncertainty should be less than $\pm 1.5\%$ [44].

3.5.3 Determination of equivalent reflectance of water-leaving radiance

So far, an error analysis has been performed only for the conventional retrieval discussed in

§3.4.2. To assess the efficacy of the algorithm, simulations of the total equivalent reflectance at the spacecraft using aerosol models which were similar, but not identical, to the candidate aerosols models, were carried out. The simulated reflectance was then used as pseudo-data for insertion into the correction algorithm. The error in the retrieval of the top-of-atmosphere water leaving radiance at 446 nm was nearly always found to be in the range 0.001 - 0.002. This error meets the SeaWiFS goal of retrieving this quantity to within 5% in waters with low phytoplankton pigment concentrations, e.g., the Sargasso Sea in summer.

3.6 PRACTICAL CONSIDERATIONS

3.6.1 Numerical computation considerations

Requirements on processing speed and data storage are described in [M-10].

3.6.2 Programming and procedural considerations

Guidelines to be followed during algorithm development are described in [M-7].

3.6.3 Configuration of retrievals

A Surface Retrieval Configuration File is used to establish the numerical values of adjustable parameters used within the retrievals, e.g., thresholds establishing whether an iteration may be terminated. This avoids “hard-wiring” specific values into the software. The Aerosol/Surface Product will contain information indicating what version of the configuration file was used. The contents of the Surface Retrieval Configuration File are shown in Table 8. The values shown correspond to the at-launch settings. The column entitled “Section” indicates where in this ATB a description of the specific configuration parameter is found.

Table 8: Contents of the Surface Retrieval Configuration File

Parameter	Value	Section
Maximum acceptable RDQI for performing a surface retrieval, $RDQI_1$	0	3.2.1.3
Number of iterations of Eq. (25)	2	3.3.3.2
Number of iterations of Eq. (75)	1	3.3.4.2
NDVI value for discriminating vegetated and non-vegetated land $NDVI_{thresh}$	0.2	3.3.6.2
DHR/BHR “tuning” parameter γ	0.0	3.3.6.2
First comparison test acceptability parameter $\Delta_{1,thresh}$	1	3.3.6.2
Second comparison test acceptability parameter $\Delta_{2,thresh}$	1	3.3.6.2
Saturation test threshold, δ	0.01	3.3.6.2
Natural uncertainty in NDVI associated with a particular biome	0.1	3.3.6.2

Table 8: Contents of the Surface Retrieval Configuration File (continued)

Parameter	Value	Section
Latitude limits on tropical ocean retrievals	$\pm 2.695^\circ$	3.4
Coefficient α in Eq. (165)	1.12	3.4.4.2
Coefficient β in Eq. (165)	1.7	3.4.4.2

3.6.4 Quality assessment and diagnostics

A number of parameters and indicators will be reported in the Aerosol/Surface Product as retrieval diagnostics. Maps or other summaries of these parameters will be reviewed by the MISR team for quality assessment. Included among these are retrieval residuals, sources of ancillary and external data, statistical information regarding the processing, etc. A tabulation of these indicators is provided in [M-9], cross-referenced, where applicable, to the pertinent section of this ATB document.

3.6.5 Exception handling

A surface retrieval is performed only if a valid aerosol retrieval exists for the region being processed (i.e., the region passed cloud screen, topographic complexity, and other tests), if the average slope of the surface element (over land) is less than 20° , and if the residuals in the aerosol model fits are below an acceptable threshold. Over oceans sun glint in the B-cameras may also limit the number of surface retrievals.

In addition to the above, it is possible that data in one or more of the 36 instrument channels could be missing. This situation could arise either due to failure of an instrument channel in flight, or as a result of obscuration of a particular camera's view of a surface region by cloud or terrain. These cases will be handled as follows:

- (1) Surface retrievals will be done using all available channels. Any missing channels will be handled through appropriate interpolation procedures in the algorithm. It is expected that accuracy degradation of the surface parameters will occur commensurate with the number of missing channels.

3.7 ALGORITHM VALIDATION

Validation of the surface retrieval algorithms will rely on several sources of data including aircraft observations, together with field observations of downwelling diffuse sky spectral radiance and irradiance, the direct solar irradiance component, and the surface spectral bidirectional reflectance distribution function (BRDF).

Details on planned field campaigns, experimental methodologies, and instrument calibration

and data reduction procedures are documented in [M-8]. For this information, the reader is referred to this source.

3.8 ALGORITHM DEVELOPMENT SCHEDULE

A strategy for time-phased development of the algorithms for the product described in this document, and a listing of key development milestones, are provided in [M-7].

4. ASSUMPTIONS AND LIMITATIONS

4.1 ASSUMPTIONS

The following assumptions are made with respect to the surface retrievals described in this document:

- (1) The description of multiple reflections between the atmosphere and surface is approximated by representing the surface as a lambertian reflector.
- (2) Surface slope effects are ignored in the calculation of the interaction between the surface and downwelling diffuse radiation.
- (3) The EOS Project will insure that assimilated meteorological fields from the EOS Data Assimilation Project are available to the MISR data processing system at the DAAC in a timely fashion.
- (4) The plane-parallel approximation for radiative transfer is assumed to be valid.
- (5) Adjacency effects are ignored at the scales at which the surface parameters are reported.
- (6) Radiances upon which surface retrievals are performed have been normalized to an Earth-Sun distance of 1 AU and corrected for the effects of ozone, as described in [M-5].
- (7) View-dependent footprint size differences and image misregistration do not significantly degrade the surface retrieval process.

4.2 LIMITATIONS

The following limitations apply to the at-launch surface retrievals described in this document:

- (1) Retrievals will not be performed over topographically complex terrain.
- (2) Retrievals will not be performed over any scene for which there is not a valid aerosol retrieval.

5. REFERENCES

- [1] Ahmad, S.P. and D.W. Deering (1992). A simple analytical function for bidirectional reflectance. *J. Geophys. Res.* **97**, 18,867-18,886.
- [2] Asrar, G., M. Fuchs, E.T. Kanemasu, and J.L. Hatfield (1984). Estimating absorbed photosynthetic radiation and leaf area index from spectral reflectance in wheat. *Agron. J.* **76**, 300-306.
- [3] Balch, W.M., P.M. Holligan, S.G. Ackleson and K.J. Voss (1991). Biological and optical properties of mesoscale coccolithophore blooms in the Gulf of Maine. *Limnol. and Oceanogr.* **34**, 629-643.
- [4] Bevington, P.R. (1969). *Data Reduction and Error Analysis for the Physical Sciences*. McGraw-Hill, Inc., 336 pp.
- [5] Borel, C. (1994). MISR Science Team Meeting, Pasadena, CA.
- [6] Cavayas, F. (1987). Modelling and correction of topographic effect using multi-temporal satellite images, *Canadian J. Remote Sensing* **13**, 49.
- [7] Chandrasekhar, S. (1960). *Radiative Transfer*. Dover Publications, Inc., New York, pp. 393.
- [8] Charney, J., W.J. Quirk, S. Chow, and J. Kornfield (1977). A comparative study of the effects of albedo change on droughts in semi-arid regions, *J. Atmos. Sci.* **34**, 1366.
- [9] Cox, C. and W. Munk (1954). Measurements of the roughness of the sea surface from photographs of the Sun's glitter. *Jour. Opt. Soc. of Am.* **44**, 838.
- [10] Dickinson, R.E. (1981). Land surface processes and climate-surface albedos and energy balance. *Adv. Geophys.* **25**, 305.
- [11] Dickinson, R. E., B. Pinty, and M. M. Verstraete (1990). Relating surface albedos in GCM to remotely sensed data. *Agricultural and Forest Meteorology* **52**, 109.
- [12] Diner, D.J. and J.V. Martonchik (1984a). Atmospheric transfer of radiation above an inhomogeneous non-lambertian reflective ground. I. Theory. *J. Quant. Spectrosc. Radiat. Trans.* **31**, 97-125.
- [13] Diner, D.J. and J.V. Martonchik (1984b). Atmospheric transfer of radiation above an inhomogeneous non-lambertian reflective ground. II. Computational considerations and results. *J.*

Quant. Spectrosc. Radiat. Trans. **32**, 279-304.

[14] Diner, D.J. and J. V. Martonchik (1985). Influence of aerosol scattering on atmospheric blurring of surface features. *IEEE Trans. Geosci. and Rem. Sens.* **GE-23**, 618.

[15] Diner, D.J., J.V. Martonchik, C.J. Bruegge, J.E. Conel, E.D. Danielson (1989). Progress report to the NASA Remote Sensing Science Program.

[16] Engelsen, O., B. D. Pinty, and M. M. Verstraete (1996). Parametric Bidirectional Reflectance Factor (BRF) models: I. Evaluation. Internal report, Institute for Remote Sensing Applications, Joint Research Centre, Ispra, Italy.

[17] Gordon, H.R., D.K. Clark, J.W. Brown, O.B. Brown, R.H. Evans, and W.W. Broenkow (1983). Phytoplankton pigment concentrations in the Middle Atlantic Bight: comparison between ship determinations and Coastal Zone Color Scanner estimates. *Appl. Opt.* **22**, 20-36.

[18] Gordon, H.R. (1987). Calibration requirements and methodology for remote sensors viewing the ocean in the visible. *Remote Sens. Environ.* **22**, 103-126.

[19] Gordon, H. (1994). MODIS Normalized Water-leaving Radiance Algorithm Theoretical Basis Document, Version 2, Submitted Nov. 1, 1994 under NASA/GSFC Contract NAS5-31363.

[20] Gordon, H.R. and M. Wang (1994). Retrieval of water-leaving radiance and aerosol optical thickness over the oceans with SeaWiFS: A preliminary algorithm. *Appl. Opt.* **33**, 443-452.

[21] Grant, I.P. and G.E. Hunt (1968). Solution of radiative transfer problems using the invariant S_n method. *Mon. Not. Roy. Astron. Soc.* **141**, 27-41.

[22] Gray, M.H. (1986). Radiometric correction of satellite imagery for topographic and atmospheric effects. M. Sc. Thesis, Faculty of Forestry, University of British Columbia, Vancouver, BC.

[23] Jacquemoud, S. and F. Baret (1990). PROSPECT: A model of leaf optical properties spectra. *Remote Sens. Environ.* **34**, 75-91.

[24] Kimes, D.S. (1983). Dynamics of directional reflectance factor distributions for vegetation canopies. *Appl. Opt.* **22**, 1364-1372.

[25] Kimes, D.S., W.W. Newcomb, R.F. Nelson, and J.B. Schutt (1985a). Directional reflectance distributions of a hardwood and pine forest canopy. *IEEE Trans. Geosci. Remote Sens.*

GE-24, 281-293.

[26] Kimes, D.S., W.W. Newcomb, C.J. Tucker, et al. (1985b). Directional reflectance factor distributions for cover types of Northern Africa in NOAA 7/8 AVHRR Bands 1 and 2. *Remote Sens. Environ.* **18**, 1-19.

[27] Kimes, D. S., P. J. Sellers and D. J. Diner (1987). Extraction of spectral hemispherical reflectance (albedo) of surfaces from nadir and directional reflectance data. *Int. J. Rem. Sens.* **8**, 1727.

[28] Koepke, P. (1984). Effective reflectance of oceanic whitecaps. *Appl. Opt.* **23**, 1816.

[29] Loveland, T.R., J.W. Merchant, D.O. Ohlen, and J.F. Brown (1991). Development of a land cover characteristic data base for the conterminous U.S.. *Photogram. Eng. and Remote Sens.* **57**, 1453-1463.

[30] Martonchik, J. V., E. D. Danielson, D. J. Diner, and C. J. Bruegge (1993). Retrieval of surface directional reflectance and hemispherical albedo using multi-angle measurements. *Proceedings of the IGARSS'93 Symposium*, Tokyo, Japan, pp. 1103-1106.

[31] Mintz, Y. (1984), *The Global Climate* (J.T. Houghton, ed.), Cambridge University Press, Cambridge, London, New York, 79-105.

[32] Monahan, E. C. and I. G. O'Muircheartaigh (1980). Optimal power-law description of oceanic whitecap coverage dependence on wind speed. *J. Phys. Oceanogr.* **10**, 2094.

[33] Myneni, R.B. and D.L. Williams (1994). On the relationship between FAPAR and ND-VI. *Remote Sens. Environ.* **49**, 200-211.

[34] Myneni, R.B., F.G. Hall, P.J. Sellers, and A.L. Marshak (1995). The interpretation of spectral vegetation indices. *IEEE Trans. Geosci. Remote Sens.* **33**, 481-486.

[35] Nicodemus, F. E., J. C. Richmond, J. J. Hsia, I. W. Ginsberg, and T. Limperis (1977). *Geometrical Considerations and Nomenclature for Reflectance*, NBS Monograph **160**, National Bureau of Standards, U.S. Department of Commerce, Washington, D.C.

[36] Peterson, D.L., M.A. Spanner, S.W. Running, and L. Band (1987). Relationship of Thematic Mapper Simulator data to leaf area index. *Remote Sens. Environ.* **22**, 323-341.

[37] Rahman, H., B. Pinty, and M.M. Verstraete (1993). Coupled surface-atmosphere reflectance (CSAR) model 2. Semiempirical surface model usable with NOAA Advanced Very High

Resolution Radiometer data. *J. Geophys. Res.* **98**, 20,791-20,801.

[38] Schluessel, G., R.E. Dickinson, J.L. Privette, W.J. Emery, and R. Kokaly (1994). Modeling the bidirectional reflectance distribution function of mixed finite plant canopies and soil. *J. Geophys. Res.* **99**, 10,577-10,600.

[39] Sellers, P. J. (1985). Canopy reflectance, photosynthesis and transpiration. *Int. J. Rem. Sens.* **8**, 1335.

[40] Sellers, P. J. (1987). Canopy reflectance, photosynthesis and transpiration II: The role of biophysics in the linearity of their interdependence. *Remote Sens. Env.* **21**, 143.

[41] Shettle, E.P. and R.W. Fenn (1979). Models for the aerosols of the lower atmosphere and the effects of humidity variations on their optical properties. Air Force Geophysics Laboratory, Hanscomb AFB, MA 01731, AFGL-TR-79-0214.

[42] Starks, P.J., J.M. Norman, B.L. Blad, E.A. Walter-shea, and C.L. Walthall (1991). Estimation of shortwave hemispherical reflectance (albedo) from bidirectionally reflected radiance data. *Remote Sens. Env.* **38**, 123-134.

[43] Teillet, P.M., B. Guindon, and D.G. Goodenough (1982). On the slope-aspect correction of multispectral scanner data, *Canadian J. Remote Sensing* **8**, 84.

[44] Teillet, P.M. and K. Staenz (1992). Atmospheric effects due to topography on MODIS vegetation index data simulated from AVIRIS imagery over mountainous terrain. *Canadian J. Remote Sensing* **18**, 283.

[45] Verstraete, M.M, B. Pinty, and R.E. Dickinson (1990). A physical model of the bidirectional reflectance of vegetation canopies 1. Theory. *J. Geophys. Res.* **95**, 11755.

[46] Wang, M. and H.R. Gordon (1994). Radiance reflected from the ocean-atmosphere system: synthesis from individual components of the aerosol size distribution, *Appl. Opt.* **33**, 7088-7095.

[47] Woodham, R.J. and T.K. Lee (1985). Photometric method for radiometric correction of multispectral scanner data, *Canadian J. Remote Sensing* **11**, 132.